

Measurement of the Cross Section for the Quasi-elastic Photoproduction of $\psi(2S)$ at HERA

Victoria Louise Hudgson

*Thesis submitted for the degree of
Doctor of Philosophy*

April 1997

School of Physics and Space Research
Faculty of Science
The University of Birmingham

Abstract

The H1 detector first started taking data at the ep collider, HERA, in 1992. Penetrating muons at small angles to the proton beam are identified and measured using the Forward Muon Detector (FMD) at H1. The methods used to calibrate the detector are presented, and the results of monitoring the calibration constants over 1994 and 1995 are shown. The alignment of the FMD is discussed, and the effects of misalignment on the momentum resolution of the detector is shown.

A measurement is presented of the cross section for the quasi-elastic photoproduction of $\psi(2S)$ mesons at H1. The $\psi(2S)$ meson was identified from the decay $\psi(2S) \rightarrow J/\psi \pi^+ \pi^-$, and the measurement was made from data taken over 1994 and 1995. For values of the elasticity variable, $z > 0.95$, the cross section was measured to be $18 \pm 3(stat) \pm 3(syst)$ nb, at a centre-of-mass energy of $W_{\gamma p} = 80$ GeV. When compared to the equivalent cross section for J/ψ production, this gave a ratio of the cross sections for $\psi(2S)$ and J/ψ of $0.15 \pm 0.03(stat) \pm 0.02(syst)$. The cross section was also measured where the $\psi(2S)$ was identified by the decay channel $\psi(2S) \rightarrow l^+ l^-$. Using this sample, the cross section, in the same kinematic region and at the same energy, was found to be $22 \pm 4(stat) \pm 6(stat)$ nb.

Between October 1993 and September 1996, this work was supported financially by the UK Particle Physics and Astronomy Research Council (P.P.A.R.C), formerly a part of the Science and Engineering Research Council (S.E.R.C).

A note on Units

In this work, a system of natural units will be used, whereby $\hbar = c = 1$

Contents

1	The H1 Detector	3
1.1	The HERA Accelerator	3
1.2	General Overview of H1	4
1.3	Tracking	7
1.3.1	The Central Tracking Detector	8
1.3.2	The Forward Tracking Detector	9
1.3.3	Backward Chambers	9
1.4	Calorimetry	10
1.4.1	Liquid Argon Calorimeter	10
1.4.2	BEMC	12
1.4.3	SPACAL	12
1.4.4	Instrumented Iron	13
1.4.5	Plug Calorimeter	14
1.5	The Forward Muon Detector	14
1.6	The Luminosity System	17
1.7	Timing Devices	19
1.8	Triggering and Data Acquisition	19

2	Calibration and Alignment of the Forward Muon Detector	22
2.1	Introduction	22
2.2	Reconstruction in the FMD	22
2.2.1	Qt Analysis	22
2.2.2	Space-point reconstruction	23
2.2.3	Track reconstruction	24
2.3	Determination of the calibration constants	24
2.3.1	The Drift Velocity	25
2.3.2	Determination of the T_0	26
2.4	Variation of Drift Velocity with Voltage	27
2.5	Monitoring of 1994 and 1995 Data	32
2.6	Alignment of the FMD	36
2.6.1	Physical Surveys	37
2.6.2	Checksum Method	37
2.6.3	Results	39
2.6.4	Checks on the alignment procedure	39
2.6.5	The effect of misalignment on momentum resolution	42
2.7	Summary	44
3	HERA Physics	48
3.1	Introduction	48
3.2	Deep Inelastic Scattering	48
3.2.1	Kinematics	49
3.2.2	The Proton Structure Function	50

3.3	Photoproduction	53
3.3.1	Elastic scattering and Regge Models	53
3.3.2	The Vector Dominance Model	55
3.3.3	Hard Scattering in Photoproduction	56
3.4	Heavy Flavour Production	57
3.4.1	Open Charm	58
3.4.2	Charmonium	59
3.4.3	Inelastic charmonium production	62
3.4.4	Diffractive ψ production	65
3.4.5	Ratio of ψ' to J/ψ	68
4	Event Selection	71
4.1	Introduction	71
4.2	Event kinematics	72
4.3	Monte Carlo Simulation	74
4.3.1	The DIFFVM event generator	74
4.3.2	Simulation	75
4.4	Triggering	76
4.4.1	L1 subtriggers	76
4.4.2	The Liquid Argon bigray trigger element (<i>LAr_BR</i>)	76
4.4.3	The topological trigger element (<i>Topo_BR</i>)	77
4.4.4	Muon trigger elements	77
4.4.5	The Z-Vertex trigger elements	80
4.4.6	Track trigger elements	83

4.4.7	Veto elements	83
4.5	Lepton identification	85
4.5.1	Identification in the Liquid Argon Calorimeter	85
4.5.2	Identification in the Instrumented Iron	86
4.5.3	Efficiency of lepton identification	86
4.6	Track selection	87
4.7	Selection of ψ' Candidates	91
4.7.1	Four track sample	91
4.7.2	Two track sample	92
4.8	Kinematic Acceptance	92
5	Measurement of Cross-Sections	98
5.1	Signals	98
5.2	Acceptance determination	102
5.3	Systematic Errors	103
5.4	Cross section measurements	107
5.4.1	Results from the four track sample	108
5.4.2	Photon Flux	109
5.4.3	Combined Cross section Result	111
5.4.4	Results from the two track sample	111
5.5	Comparison with other experiments	112
5.6	Summary	114

List of Figures

1.1	Layout of the HERA accelerator and the pre-accelerators	3
1.2	The H1 Detector	6
1.3	The H1 tracking system	7
1.4	Radial view of the H1 central tracking detector	8
1.5	The Calorimetry system of the H1 Detector	11
1.6	A cross section view of the FMD	15
1.7	Theta Octant of the FMD	16
1.8	Phi Octant of the FMD	16
1.9	A drift cell in the FMD	17
1.10	The layout of the luminosity system	18
2.1	Time distribution, and middle range of time distribution	26
2.2	Possible stagger permutations of the drift cells	28
2.3	T_{mid} before and after the toroid	29
2.4	Checksum used to determine the resolution of the drift coordinate.	30
2.5	Variation of drift velocity with E/p	31
2.6	Hit map of the FMD	32
2.7	Variation of drift velocity with voltage	33

2.8	Drift velocity per quadrant at constant voltage	33
2.9	Variation of drift velocity, T_{mid} and T_0 (1994 data)	34
2.10	Variation of drift velocity, T_{mid} and T_0 (1995 data)	35
2.11	Schematic diagram of the FMD to show the checksum method of aligning the chambers.	38
2.12	Examples of the checksums used in the alignment procedure	41
2.13	Checksums obtained after alignment procedure	42
2.14	Checks on the alignment procedure using simulated data	43
2.15	Examples of momentum resolution plots for a misaligned, aligned and per- fectly aligned system	45
2.16	Inverse momentum resolution vs. momentum for a misaligned, aligned and perfectly aligned system	45
2.17	Signal for elastic J/ψ production in the forward direction, momentum mea- sured in the FMD.	47
2.18	Signal for elastic J/ψ production in the forward direction, momentum mea- sured in the Forward Tracker.	47
3.1	Kinematics of electron - proton scattering	49
3.2	Measurement of the structure function $F_2(x, Q^2)$ as a function of Q^2	52
3.3	Measurement of the structure function $F_2(x, Q^2)$ as a function of x	52
3.4	Total photoproduction cross section as a function of the γp centre of mass energy	55
3.5	Examples of hard photoproduction processes at HERA	57
3.6	The charm contribution, $F_2^{c\bar{c}}$ to the proton structure function	59
3.7	Total charm photoproduction cross section as a function of $W_{\gamma p}$	60
3.8	Energy levels for the charmonium system	61

3.9	Strong decays of charmonium states above and below the $D\bar{D}$ threshold . . .	62
3.10	Inelastic J/ψ production via photon gluon fusion	63
3.11	Resolved photon contribution to inelastic J/ψ	64
3.12	Diffraction production of ψ' via pomeron exchange	65
3.13	Total cross section for the elastic photoproduction of J/ψ	67
3.14	$d\sigma/dp_T^2$ for both elastic production of J/ψ and production with proton dissociation	67
3.15	Diffraction production of ψ in the Ryskin model	68
3.16	J/ψ decay to electron pair via an intermediate photon	69
4.1	Reconstructed kinematic variables $W_{\gamma p}$ and y_{JB}	73
4.2	Generated and reconstructed values for the elasticity variable z	74
4.3	Efficiency of the topological and LAr bigray trigger elements (1994)	78
4.4	Efficiency of the topological and LAr bigray trigger elements (1995)	79
4.5	Efficiency of the iron endcap and central barrel trigger elements (1994)	81
4.6	Efficiency of the iron endcap and central barrel trigger elements (1995)	82
4.7	Efficiency of the $DCRPh$ trigger elements	84
4.8	Efficiency of the $DCRPh$ trigger elements	85
4.9	Data samples chosen for lepton identification efficiency studies	87
4.10	Lepton identification efficiencies in the 1994 data	88
4.11	Lepton identification efficiencies in the 1995 data	89
4.12	ψ' candidate event	93
4.13	Kinematic region of acceptance (electron channel)	95
4.14	Kinematic region of acceptance (muon channel)	96

4.15	Acceptance in Q^2 in the 1995 data	97
5.1	ψ' signal in 1994 data	99
5.2	J/ψ and ψ' invariant mass distributions in the 1994 data	99
5.3	ψ' signal in 1995 data	100
5.4	J/ψ and ψ' invariant mass distributions in the 1995 data	100
5.5	Signal for ψ' from the two track sample (1994)	101
5.6	Signal for ψ' from the two track sample (1995)	101
5.7	Comparison between data and MC of various distributions of the ψ' and the decay particles in the event. The distributions are shown from data taken in 1994	104
5.8	Comparison between data and MC of various distributions of the ψ' and the decay particles in the event, where the data is taken from 1995.	105
5.9	Fit to the two track data sample around the ψ' mass.	112
5.10	Ratio of the cross sections for the photoproduction of J/ψ and ψ' mesons .	113

List of Tables

2.1	Voltage set ups for drift velocity scan	30
2.2	Checksums used to determine misalignment values	39
2.3	Results from translational alignment using cosmic muon data	40
4.1	Decay channels and branching ratios	72
4.2	L1 subtriggers used in the analysis	76
4.3	Trigger element efficiencies	86
4.4	Lepton identification efficiencies in 1994 and 1995	87
5.1	Number of events observed in the channels $\psi' \rightarrow J/\psi(\rightarrow l^+l^-)\pi^+\pi^-$	98
5.2	Acceptances for triggering and reconstructing ψ' events in 1994 and 1995 data	103
5.3	Contributions to systematic error from individual trigger elements	106
5.4	Systematic errors for the four data samples from the 1994 and 1995 data, together with the errors for the combined result.	108
5.5	Systematic errors for the two track data sample (94/95)	109
5.6	Summary of ep and photoproduction cross sections for the four data samples.	110

Synopsis

HERA is the world's first electron proton collider, and as such, continues a long history of scattering experiments in particle physics. The point like nature of the electron makes it an ideal particle to probe the composite structure of the proton, first revealed by early fixed target ep scattering experiments at SLAC [1]. These large momentum transfer, inelastic ep scattering interactions are known as *deep inelastic scattering* (DIS), and are interpreted as the electron being scattered elastically by a point like particle inside the proton. The study of these interactions provides information about the structure of the proton and the nature of the strong force. The scale at which the target proton may be probed is a function of the four momentum transfer squared, Q^2 . At HERA, electron and proton beams are collided at very high energies (27.5 GeV and 820 GeV respectively) so that values of Q^2 may be achieved which are orders of magnitude larger than those from previous fixed target experiments, and the proton may be probed at distances down to approximately 10^{-18} m. Another important area of physics which may be studied at HERA is *photoproduction*, where the electron emits a quasi-real photon ($Q^2 \sim 0$), and γp collisions may be used to study the nature of the photon. The study of charm and charmonium has been an active area of interest since the discovery of the J/ψ meson in 1974. At HERA, $c\bar{c}$ pairs are produced predominantly in inelastic collisions, via photon gluon fusion, but may also be produced elastically, via the exchange of a pomeron. Production of charm in this way provides information on the hadronic behaviour of the photon, and on the nature of the pomeron.

An overview of the HERA accelerator and the H1 detector is given in the first chapter. At HERA, the fast bunch crossing rate (every 96 ns) means that H1 must deal with very high rates, and thus requires a sophisticated trigger system, a relatively novel feature of which is the pipelining of the event information. This is also discussed in chapter 1. Another difference between HERA and other high energy colliders is the asymmetry in the energies of the colliding beams. Due to this asymmetry, H1 has enhanced instrumentation in the forward (proton) direction. Detection of forward going muons is important in the study of heavy flavour physics, as muons may be produced in the decay of charm

quarks ($c \rightarrow \mu\nu_\mu s$) or from the decay of J/ψ ($J/\psi \rightarrow \mu^+\mu^-$). In order to improve muon identification and measurement in the forward direction, a forward muon detector (FMD) is incorporated at H1. This detector is discussed in some detail in chapter 1, whilst chapter 2 examines the method of reconstructing tracks through the detector, and the calibration necessary to achieve this. Monitoring of the calibration constants over 1994 and 1995 is discussed. In order to achieve the best momentum resolution possible with the FMD, accurate knowledge of the alignment of the system is necessary. The FMD is aligned by using measurements from physical surveys, and by using the straight tracks from cosmic muons which pass through the detector. Chapter 2 concludes with a study of the effect of misalignment on the momentum resolution. The alignment and calibration work covered in this chapter is the author's own, although the methods on which it is based were developed by Andrew Mehta and Paul Sutton. The work also relied on the forward muon reconstruction code, written by Lee West. An overview of some of the main physics topics studied at HERA is given in chapter 3, focusing in particular on the production of charm. Bound states of charm and anti-charm quarks are known as charmonium, and the various production mechanisms for charmonium states at H1 are discussed in chapter 3. The remainder of the thesis focuses on the quasi-elastic production at HERA of the 2S charmonium state, ψ' . The criteria by which candidate events are selected is discussed in chapter 4. This chapter includes a description of the triggers used to obtain the events, and a study of the efficiency of these triggers. As the particle is identified by its decay to leptons (either directly or via the decay of a J/ψ), the methods of lepton identification are discussed, and a study of the identification efficiency of muons and electrons in H1 is included. The overall acceptance for triggering on, identifying and reconstructing a ψ' meson is measured using the DIFFVM MC. It is important, therefore, that the MC simulation closely models the real data in terms of the reconstruction and identification efficiencies *etc.* Comparisons between data and MC are therefore shown for all the efficiency studies included in chapter 4, and these are used to estimate the systematic uncertainty on the acceptance. The signals observed for ψ' mesons in different decay channels are shown in chapter 5, and the cross section measurements are presented. The ratio of the cross sections for the production of the 2S charmonium state, ψ' , to the 1S state, J/ψ , is presented, and this result is compared with the same ratio obtained from lower energy fixed target experiments. The analysis presented in these final two chapters is the author's own work.

Chapter 1

The H1 Detector

1.1 The HERA Accelerator

The HERA (**H**adron **E**lektron **R**ing **A**nlage) collider at DESY is the first electron (positron)¹ - proton collider to be built. It consists of two independent storage rings housed in a tunnel of 6.4 km circumference, between 15 and 20 m underground. The counter rotating beams are collided at zero crossing angle at two interaction points in the North and South Halls of the accelerator, where the H1 and ZEUS detectors are positioned. The experiment HERMES is positioned in the East hall, using only the electron beam, and in the West using only the proton beam is HERA-B. The layout of the HERA accelerator is shown in figure 1.1.

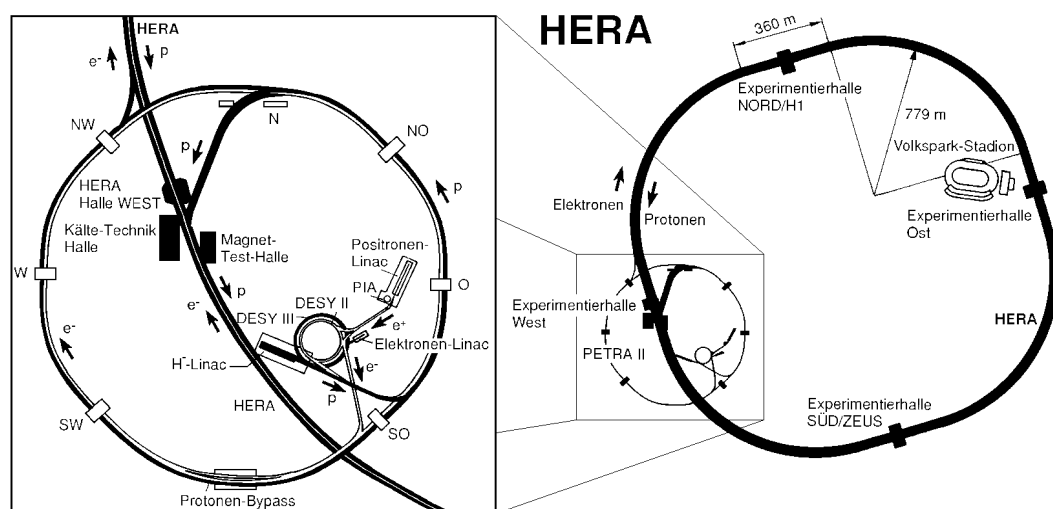


Figure 1.1: *Layout of the HERA accelerator and the pre-accelerators.*

¹From mid-1994 HERA has been operating with a positron beam. Henceforth, the beam lepton will be referred to as *electron* regardless of its charge.

The proton and electron beams are accelerated using both superconducting and warm RF cavities to energies of 820 GeV and 27.5 GeV respectively. This gives a centre of mass energy of approximately 300 GeV, an improvement by an order of magnitude on previous fixed target experiments, giving HERA enormous physics potential. The electron beam energy is limited by synchrotron radiation, but this effect is negligible for the proton beam. Whilst conventional steering magnets are used for the electron beam, stronger fields are required in order to constrain the protons, hence superconducting coils are used. At design luminosity, there would be 210 electron and proton bunches colliding, but in 1994 HERA was operating with 153 colliding bunches of each type, and in 1995 this increased to 174. In both years a small number of non-colliding electron and proton bunches were included; these are referred to as *pilot bunches*, and are used to estimate beam induced background arising from interactions of the beam with the residual gas in the beam pipe, or with the beam wall. Bunch crossings occur every 96 ns. Luminosity was first achieved at HERA in 1992, by 1994 the average luminosity was $1.4 \times 10^{30} \text{ cm}^{-2}\text{s}^{-1}$, and in 1995 it was $2.13 \times 10^{30} \text{ cm}^{-2}\text{s}^{-1}$.

The HERMES experiment uses the electron beam on a polarised target to investigate the spin structure function of the proton and neutron. HERA-B uses a fixed wire target in the proton beam, with the aim of studying *b*-quarks, produced via gluon-gluon fusion. The rest of this chapter will concentrate on the H1 detector.

1.2 General Overview of H1

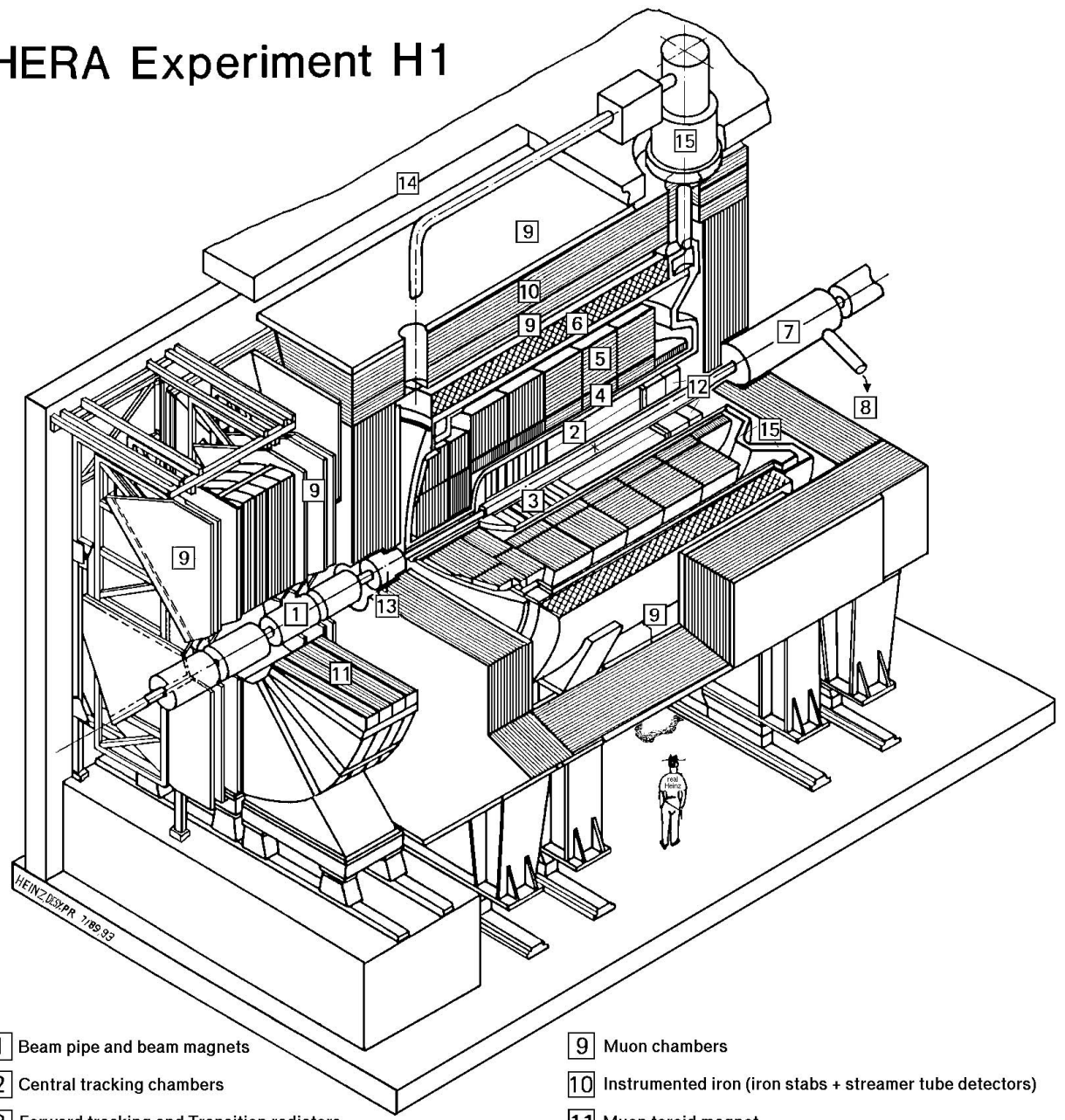
H1, shown in figure 1.2, is one of the two general purpose detectors presently operating at HERA. It is built on the same principles as most modern collider experiments, differing in the enhanced instrumentation in the proton direction due to the asymmetric proton and electron beam energies. The coordinate system in H1 is such that the *z*-axis runs along the beam pipe, with the origin at the interaction point inside H1 (the nominal vertex), and the forward direction is defined as that of the proton beam. The *y* axis is vertical and the *x* axis points towards the centre of the accelerator ring. To maximise the full physics potential of HERA, the H1 detector has to satisfy certain basic requirements. Excellent electron identification and measurement is required in order to study the deep inelastic scattering process. Adequate segmentation of the calorimeter in depth, and in θ and ϕ is therefore crucial. A high degree of hermiticity is important in order to identify missing transverse momentum and investigate phenomena involving energetic neutrinos. Good electromagnetic and hadronic energy resolution is essential for making inclusive energy flow measurements for both neutral and charged current interactions. In order to study

heavy flavour physics and to allow a search for new particles, good muon identification is also very important. Finally, to make efficient use of all these facilities, and overcome the high background conditions which result from the fast bunch cross rates, a sophisticated trigger system is needed. The main components of the H1 detector are as follows²:-

- A tracking system, divided into central and forward tracking detectors, consists of several layers of drift chambers interspersed with multiwire proportional chambers for triggering. In addition there are backward chambers: the backward proportional chambers (BPC) were in place until 1994, and replaced in 1995 with backward drift chambers (BDC).
- The calorimeter system includes a liquid argon calorimeter surrounding the tracker segmented into an electromagnetic part and a hadronic part. A plug calorimeter detects hadronic energy at very small angles in the forward direction. In the shutdown of 1994/1995, the BEMC (backward electromagnetic calorimeter) was replaced by SPACAL (spaghetti calorimeter) providing calorimetry for the backward region. It is here that the final state scattered electron is detected, for DIS events of low to moderate Q^2 .
- A superconducting coil outside the hadronic calorimeter provides a uniform magnetic field of 1.6 Tesla, enabling measurement of the momentum of charged particles from the curvature of their path in the field.
- The iron return yoke of the magnet surrounds all the major components of H1, and is instrumented to allow measurement of hadronic energy not contained by the LAr calorimeter, and muon identification.
- The forward muon detector consists of layers of drift chambers either side of a toroidal magnet, providing identification and measurement of muons in the forward region.
- Electron and photon taggers are placed well downstream in the electron direction and are used to measure luminosity. The electron tagger is also important for the detection and measurement of photoproduction events.
- Time of flight devices are used to suppress the high background rates experienced at H1, by rejecting events when activity arrives out of time with the bunch crossings.

²Many backward components of the detector were replaced and upgraded in the 1994/1995 shutdown [4]. This chapter will discuss subdetectors used in both 1994 and 1995, as the work in this thesis relates to data taken over both years.

HERA Experiment H1



- | | | |
|---|----------------|---|
| <ul style="list-style-type: none"> 1 Beam pipe and beam magnets 2 Central tracking chambers 3 Forward tracking and Transition radiators 4 Electromagnetic calorimeter (lead) 5 Hadronic calorimeter (stainless steel) 6 Superconducting coil (1.2T) 7 Compensating magnet 8 Helium cryogenics | } Liquid Argon | <ul style="list-style-type: none"> 9 Muon chambers 10 Instrumented iron (iron stabs + streamer tube detectors) 11 Muon toroid magnet 12 Warm electromagnetic calorimeter 13 Plug calorimeter (Cu, Si) 14 Concrete shielding 15 Liquid Argon cryostat |
|---|----------------|---|

Figure 1.2: The H1 Detector.

The rest of this chapter contains a brief overview of each of the main features above. A more detailed discussion may be found in [2][3].

1.3 Tracking

The tracking system at H1 has been designed to provide precise measurements of the momentum and angle of isolated charged particles, and to reconstruct jets with high track densities. Many charged particles are produced at small angles in the forward direction due to the asymmetry in the energies of the electron and proton beams, so in order to facilitate good triggering and reconstruction over the whole solid angle, the tracking system is divided into two mechanically distinct tracking detectors: the central (CTD) and forward (FTD) trackers. Both detectors consist of drift chambers and multiwire proportional chambers. The drift chambers give accurate information on the trajectories of charged particles travelling through the magnetic field, thus allowing a momentum measurement, and triggering information is provided by the proportional chambers. Particle identification is achieved by measuring the specific energy loss dE/dx , with a typical energy resolution of about 10%. The tracking system is shown in figure 1.3.

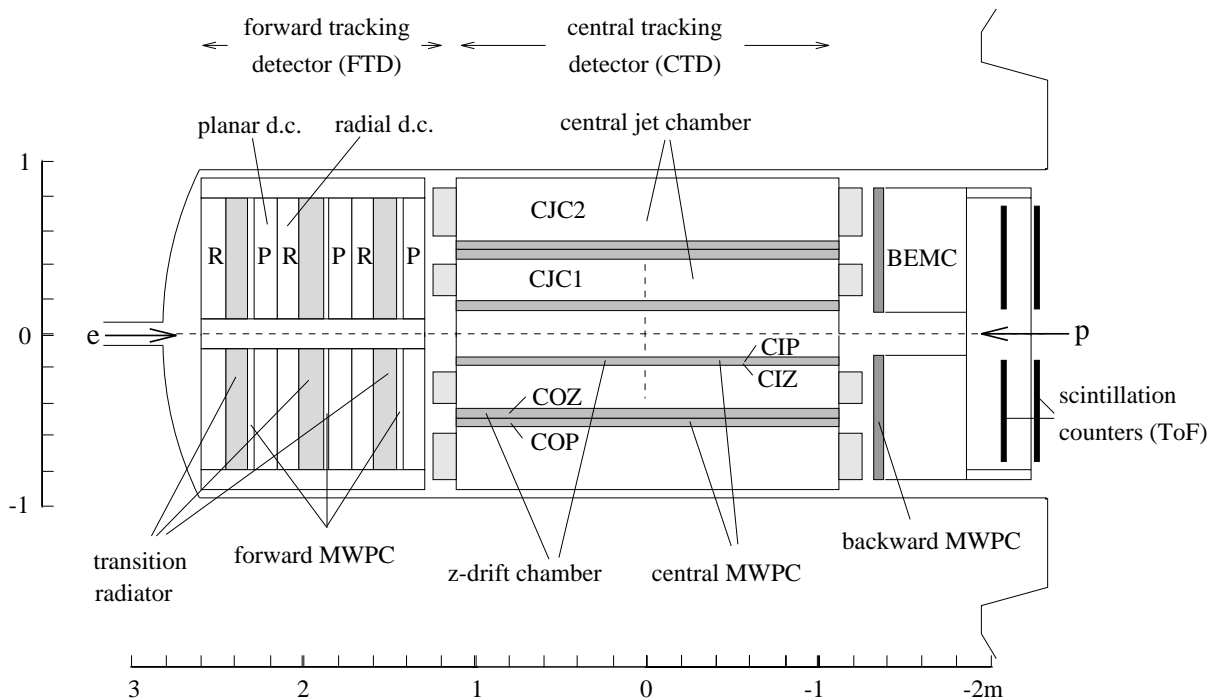


Figure 1.3: The H1 tracking system ($r - z$ view).

1.3.1 The Central Tracking Detector

The central tracking detector (CTD) consists of two concentric drift chambers, CJC1 and CJC2, interleaved with two thin drift chambers, CIZ and COZ, and two multiwire proportional chambers (MWPC's), CIP and COP, as shown in figure 1.4.

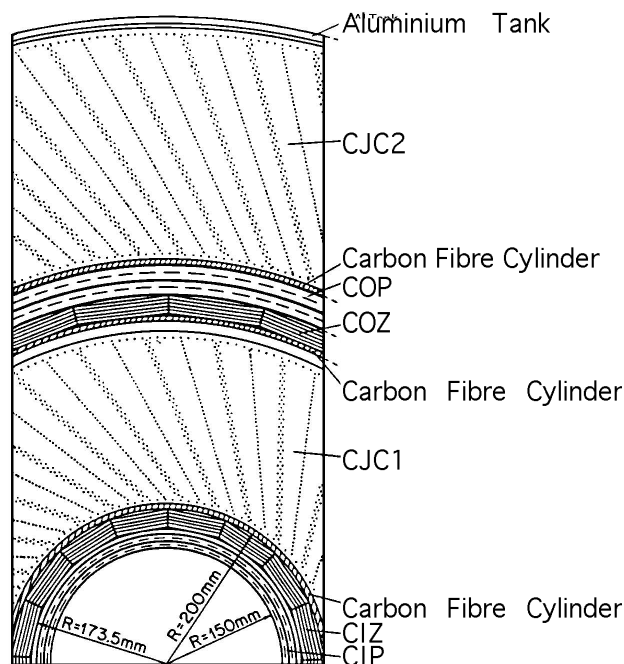


Figure 1.4: Radial view of the H1 central tracking detector.

The sense wires of the central jet chambers (CJC1 and CJC2) are strung parallel to the beam axis and are sampled from both ends to give accurate reconstruction in the $r\phi$ plane. CJC1 consists of 30 drift cells, each containing 24 sense wires, whilst CJC2 consists of 60 cells, each with 34 sense wires. The drift cells are tilted at 30° to the radial direction. The purpose of this is to allow the ionization electrons from a high momentum track ($p_T > 100$ MeV) to drift in the magnetic field in a direction which is approximately perpendicular to the track, thus optimising the track resolution. Drift ambiguities are solved by connecting together track segments from different cells³, and a measurement of the z coordinate is made from charge division. The CJC has a resolution of approximately $170 \mu\text{m}$ in the $r\phi$ plane and $2.2(3.3)$ cm in z for protons(pions). It covers the polar angular range $15^\circ < \theta < 165^\circ$.

³Drift ambiguities arise due to uncertainty in which side of the wire the particle passed. This is discussed further in section 1.5.

Two thin ‘ z -chambers’ (CIZ and COZ) sandwich the inner jet chamber and complement the measurement of charged track momenta made in the CJC. These chambers have sense wires perpendicular to the beam axis, and provide a z -measurement with a resolution of typically $300\mu\text{m}$. The polar angular range covered by the inner and outer z -chambers is $16^\circ < \theta < 169^\circ$ and $25^\circ < \theta < 156^\circ$ respectively.

The inner and outer MWPC’s, CIP and COP, provide fast space-point information for the level one (L1) trigger. The CIP is the innermost component of the central trackers and the COP lies immediately outside CJC2. They consist of concentric double layers of chambers which are read out from cathode pads. The wires are strung parallel to the beam axis, with 480 wires in each layer.

1.3.2 The Forward Tracking Detector

The Forward Tracking Detector (FTD) is designed to provide accurate detection and measurement of charged particles in the forward direction. It consists of three *supermodules*. Each supermodule consists of three layers of planar drift chambers, followed by multiwire proportional chambers, a transition radiator and finally a radial drift chamber. It has an angular coverage of $5^\circ < \theta < 30^\circ$. Each of the three layers of planar drift chambers in each supermodule consists of 32 cells with four sense wires strung in parallel, and uniformly separated in z . The wires are staggered alternately $300\mu\text{m}$ either side of the meridian plane of the cell, and are rotated by 60° in azimuth with respect to the previous layer. This facilitates accurate determination of the $r\phi$ coordinates, with a spatial resolution of approximately $150\mu\text{m} - 170\mu\text{m}$. The forward proportional chambers consist of two planes of wires interleaved with cathode pads. They provide fast track information for triggering in conjunction with the central proportional chambers. The transition radiators are designed to give discrimination between electrons and pions. The radial chambers are segmented in ϕ into 48 sections of 7.5° . Each segment consists of a plane of 12 sense wires strung radially and separated by 1 cm along the beam direction. The wires are staggered by $288\mu\text{m}$ either side of the plane to allow determination of drift ambiguities.

1.3.3 Backward Chambers

The purpose of tracking detectors in the backward region is to provide accurate determination of the scattering angle the electron. From 1992 to 1994, the backward multiwire proportional chamber (BPC) was used, which consisted of five cathode planes and four anode wire planes, where the planes were oriented at 45° to one another, with a sepa-

ration of 2.5 mm between the wires in a plane. In the shutdown of 1994/1995 this was replaced by the backward drift chambers (BDC) [4], which consists of four double layers, with wires strung radially. The four layers are rotated in ϕ by 11.5° with respect to one another.

1.4 Calorimetry

In order to measure accurately both the hadronic final state and the position and energy of the DIS scattered electrons at high Q^2 , H1 requires a calorimeter capable of identification and precision measurement of electrons, muons and neutral particles, as well as measurement of jets with high particle densities. If the coil which provides the magnetic field for the tracking detectors were placed inside the calorimeter, the energy measurement of the electromagnetic showers would be degraded, thus a calorimeter positioned inside the coil both minimises the amount of dead material in front of the calorimeter and the overall size.

Calorimeters consist of layers of passive absorption material interleaved with layers of instrumented active regions. As a particle passes through the absorption material it produces a shower of particles which then deposit charge in the active material by ionization. Measurement of the total integrated ionisation gives a measurement of the energy of the incident particle. Electromagnetic showers occur via brehmstrahlung and pair production, and are characterised by the radiation length, X_0 , the mean length over which the energy of an electron is reduced by a factor $(1/e)$. Strongly interacting particles passing through the absorption material lose energy via inelastic nuclear collisions producing a shower of lower energy hadrons. The development of such showers takes longer than electromagnetic showers, and they are characterised by the absorption length, λ .

The calorimeter system at H1 consists of the main Liquid Argon Calorimeter (LAC), the Backward Electromagnetic Calorimeter (BEMC) (1994 and previous years) or SPACAL (from 1995 onwards) covering the backward direction, the Plug Calorimeter in the very forward direction, and finally the Tail Catcher (TC), which uses the instrumented iron. The whole calorimeter system at H1 is shown in figure 1.5.

1.4.1 Liquid Argon Calorimeter

The LAC [5] consists of layers of stainless steel and lead as the passive absorption materials, and liquid argon as the active material. Liquid argon is chosen because of its

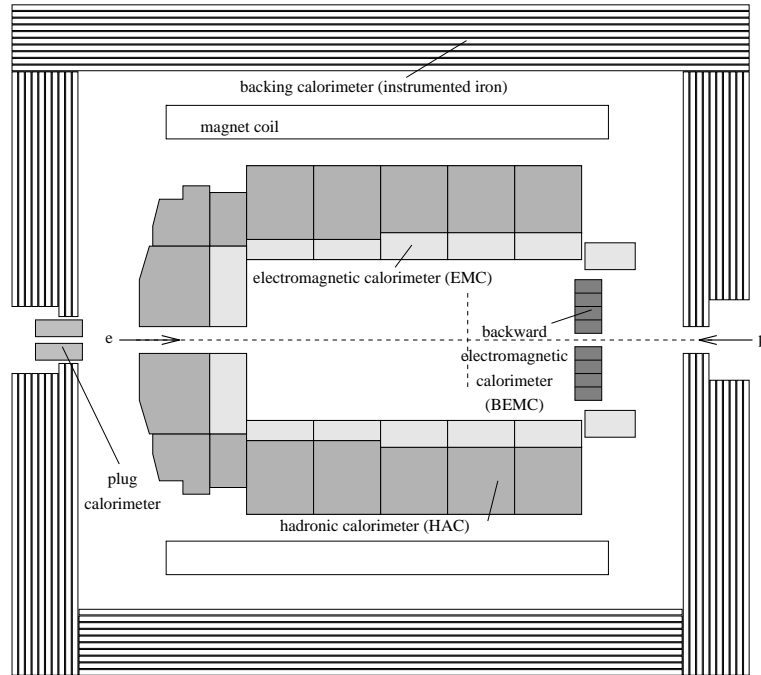


Figure 1.5: The Calorimetry system of the H1 Detector.

stability, ease of calibration and homogeneity of response. The LAC covers the angular range of approximately $4^\circ < \theta < 153^\circ$ and is segmented along the beam axis into eight self supporting ‘wheels’. Each of these wheels is in turn segmented in ϕ into eight identical stacks. The electromagnetic part of each stack consists of 2.4 mm plates of lead as the absorbing material with gaps of 2.35 mm filled with liquid argon as the active material. The hadronic calorimeter (HAC) almost completely surrounds the electromagnetic calorimeter (EMC), except for the very backward part, so that the angular coverage of the EMC is slightly larger than that of the HAC. The hadronic cells consist of 19 mm stainless steel absorber plates, with double gaps of 2.4 mm of liquid argon.

The difference in size of the EMC and HAC reflects the volume of material required to fully contain electromagnetic and hadronic showers. The total depth of the LAC is between 5 and 8 nuclear interaction lengths, whilst the EMC is between 20 and 30 radiation lengths. The energy resolution of the LAC, $\sigma(E)/E$, has been determined as approximately $10\%/\sqrt{E}$ with a constant term below 1% for electrons, and for pions $50\%/\sqrt{E}$ with an energy independent term of 3%. The energy response of hadrons is typically 30% less than that for electrons, and the calorimeter is therefore calibrated at two different energy scales. The uncertainty in these is 3% and 6% for the electromagnetic and hadronic scales respectively.

1.4.2 BEMC

The principal task of a calorimeter in the backward region is to measure the energies and positions of scattered electrons from DIS. It also should contribute to the measurement of hadronic energy emerging from low x DIS events and photoproduction processes. It has to operate in a high rate environment from the illumination on the rear side of the detector due to secondary hadrons originating from beam induced processes.

The BEMC [6] covers the kinematic region $4 < Q^2 < 100 \text{ GeV}^2$. It consists of 88 stacks mounted into an aluminium barrel of diameter 162 cm and covers a range of scattering angles of $151^\circ < \theta < 176^\circ$, with full azimuthal acceptance. The stacks are aligned parallel to the beam line, and consist of multilayer lead scintillator sandwich structures with 50 active sampling layers of plastic scintillator 4 mm thick. Of the 88 stacks, 56 are square in cross section, and the remainder are trapezoidal or triangular in shape in order to fill the circular barrel. The depth of the BEMC in z corresponds to 21.7 radiation lengths. The global energy scale for DIS electrons is adjusted using the kinematic peak⁴ in DIS events to a precision of 1%. The energy resolution of the BEMC is approximately $10\%/\sqrt{E}$ for electrons and $80\%/\sqrt{E}$ for hadrons, with a spatial resolution of 7 mm in the direction transverse to the beam.

1.4.3 SPACAL

In 1995 the BEMC was replaced by SPACAL (Spaghetti Calorimeter) [7] with the aim of increasing the kinematic acceptance to Q^2 values of less than 1 GeV^2 , giving an improved hadronic energy measurement and better e/π separation. SPACAL also replaces the time of flight hodoscope, ToF (section 1.7), in providing crucial timing information necessary in the discrimination of ep collisions from the high rate of proton beam induced background events. SPACAL is divided into an electromagnetic and a hadronic section, and consists of scintillating fibres embedded in a lead matrix.

The electromagnetic section uses fibres of diameter 0.5 mm and a lead-to-fibre ratio of 2.3:1. The hadronic SPACAL has a total active depth equivalent to 28 radiation lengths. Sets of 16 cells, each with a cross section of $40.5 \times 40.5 \text{ mm}$, are combined to form the modules which make up the electromagnetic section. The scintillation light from the fibres is read out by photomultiplier tubes, achieving a time resolution of 1 ns. The response of the calorimeter has been found to be linear between 10 and 60 GeV, with an energy

⁴The kinematic peak is a peak in the scattered electron energy spectrum at the energy of the electron beam.

resolution of approximately $7\%/\sqrt{E}$ with a constant term of $\sim 1\%$ [8].

The overall size of the hadronic section is constrained by existing mechanical structures in the backward region of H1, particularly by the return yoke of the magnet. It has the dual purpose of measuring the electromagnetic energy leakage from the electromagnetic section of the calorimeter and determination of the hadronic energy flow in the backward region. A total of 128 cells with a cross section of 119.3×119.0 mm make up the hadronic section, and these are packed parallel to the beam line. The total depth of the calorimeter, including both hadronic and electromagnetic sections, is 2.02 interaction lengths. The combined response of both the electromagnetic and hadronic sections of SPACAL provides an energy resolution for hadrons of approximately 29% [9]. The ability of the SPACAL to reconstruct and measure the energy of hadronic clusters is a significant improvement over the BEMC.

1.4.4 Instrumented Iron

The iron return yoke of the magnet that surrounds all the major detector components of H1 is instrumented with layers of limited streamer tubes (LST), which are placed in gaps between alternate layers of iron. These serve a dual purpose as a tail catcher (TC) calorimeter to detect and measure hadronic energy leaking from the LAr calorimeter and the BEMC (SPACAL), and measurement of the tracks from penetrating muons. The LST's are oriented along the beam axis in the barrel region, and vertically in the forward and backward regions. The instrumented iron covers the polar angular region $5^\circ < \theta < 175^\circ$.

The tail catcher uses the iron as the passive absorption material, and measures the resulting ionisation using the LST's. There are a total of 16 layers of LST's, 11 of which are equipped with pads. The energy measurement of the tail catcher is based on the analogue readout of the pad layers. It has a depth of approximately 4.5 interaction lengths, and an energy resolution of approximately $100\%/\sqrt{E}$.

The remaining five layers are equipped with strips which lie perpendicular to the wire direction, thus allowing reconstruction of 3-dimensional space points in these layers. The signals from both the wires and the strips are read out digitally, and the hit information is combined to reconstruct a track in the iron. Pad information is used to resolve track ambiguities. Wire signals from five of the layers are used to trigger on muons passing through the iron.

1.4.5 Plug Calorimeter

The plug calorimeter closes the gap in the acceptance for energy flow in the forward direction at small angles, between the beam pipe ($\theta \simeq 0.6^\circ$) and the forward part of the LAC ($\theta \simeq 3^\circ$). It consists of layers of copper absorber plates interleaved with layers of silicon detectors, and has a resolution of approximately $150\%/\sqrt{E}$.

1.5 The Forward Muon Detector

The Forward Muon Detector (FMD) [11] provides an independent means of both identifying and measuring the momentum of muons in the forward direction. The detector is situated between 6.4 and 9.4 m forward of the nominal H1 vertex, outside the iron return yoke. It consists of six layers of drift chambers, three either side of a toroidal magnet. The magnet bends the tracks of the particles in the polar angle, θ , thus allowing a momentum measurement to be made. It consists of eight solid iron modules built into two mobile half toroids to allow for access. Twelve rectangular coils around the toroid, each with fifteen turns of water cooled copper carrying a current of 150 A, provide a field inside the toroid of 1.75 T at its inside radius (65 cm) and 1.5 T at its outside radius (290 cm). The angular acceptance of the FMD is $3^\circ < \theta < 17^\circ$. In order to make a measurement of the momentum of a muon track, it must be detected both before and after the toroid, and must therefore have a momentum large enough for it to pass through the calorimeters, the iron return yoke around H1 and the solid iron toroid of the FMD. This results in a minimum momentum acceptance of the FMD of $p \sim 5$ GeV.

The spatial arrangement of the FMD is shown in figure 1.6. The six layers, two ϕ layers and four θ layers, each consist of eight octants which are fixed alternately on either side of an aluminium ‘door frame’. An octant from a θ layer and one from a ϕ layer are shown in figures 1.7 and 1.8 respectively. The octants are comprised of two planes of drift cells, with each plane displaced from the other by the width of half a cell, as shown in figure 1.9. Ambiguities arising from uncertainty in which side of the wire the muon passed may be solved by pairing hits in cells in two planes arranged in this manner. The θ layers have drift cells with wires strung around the beam pipe, parallel to the x -axis in the local coordinate system of the FMD, giving an accurate measurement of the polar angle, θ . The ϕ layers have wires strung parallel, where the central wire of each octant is radial.

There are a total of 1520 drift cells in the FMD. They are 2 cm by 12 cm in cross section, and vary in length from 34 cm to 241 cm. The gas mixture used is 92.5% argon, 5% carbon

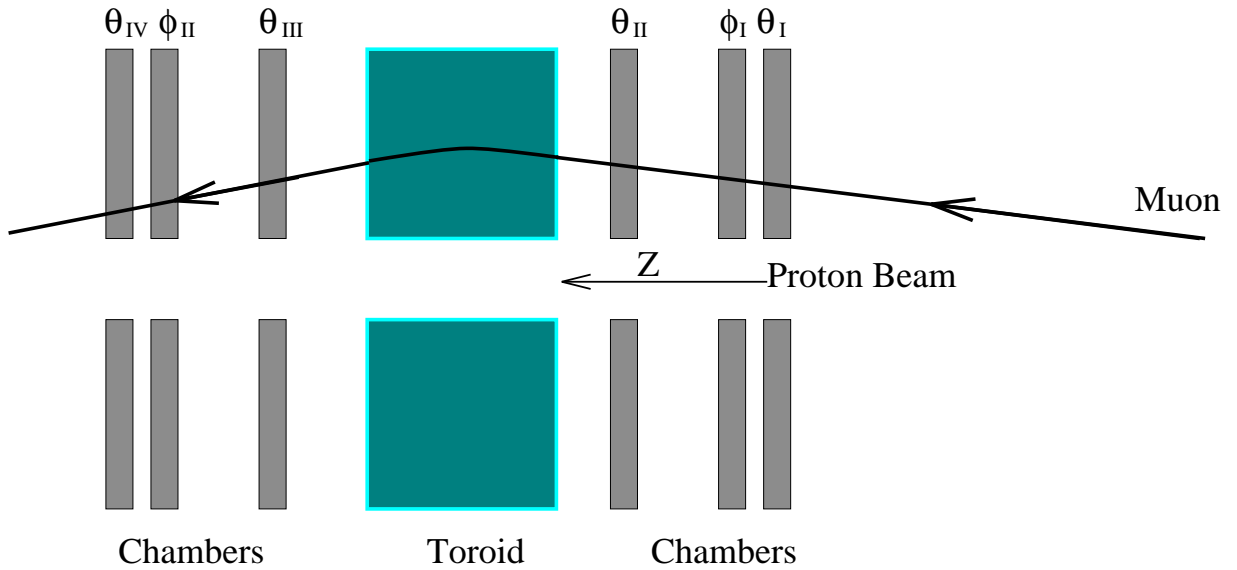


Figure 1.6: Schematic diagram representing a cross section view of the FMD.

dioxide and 2.5% methane. Each cell has a single nichrome resistive sense wire of $40\ \mu\text{m}$ or $50\ \mu\text{m}$ in diameter. The cells are linked into pairs by a $330\ \Omega$ resistor joining the ends of the sense wires of the paired cells. Each cell therefore has only one free end at which the signals from the wire can be sampled. This reduces the total number of electronic channels needed by a factor of two, at the expense of less accurate charge division information. The planes at the front and back of the cell have etched copper strips on their inner surfaces which act as drift voltage electrodes. The total drift voltage of $2.88\ \text{kV}$ provides an average field in the cell of $0.48\ \text{kVcm}^{-1}$. This field is uniform across most of the cell, except for at the edges of the cell and close to the sense wire. The sense wire at the centre of the cell is at a voltage of $4.2\ \text{kV}$, which creates a high field in the close vicinity of the wire, causing avalanching, and hence amplifying the signal on the wire. When a muon passes through a drift cell, the electrons produced from the resulting ionization drift towards the sense wire, and once they get very close to the wire, the strong electric field causes an avalanche of ionization. This produces a pulse which propagates in both directions along the wire, and is fed, via a pre-amplifier into analogue to digital converters (FADC's). These sample the cell output every $9.61\ \text{ns}$, ten times the bunch crossing frequency. Each FADC has a memory 256 time bins deep, so that at any moment a $2.5\ \mu\text{s}$ history of the drift cell is stored, which is longer than the maximum drift time for ionisation in a cell. If the event is triggered the FADC stops sampling and the memory is 'frozen' until the contents have been transferred to the front end processor. The Qt analysis performed on the digital pulses from the FADC's is described in chapter 2, together with a description of the space-point and track reconstruction.

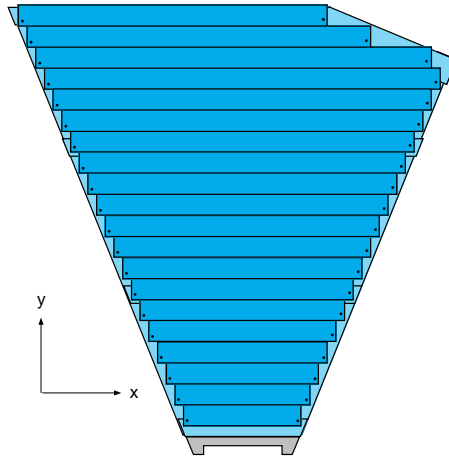


Figure 1.7: *Individual octant from a θ layer. Cells are mounted with the sense wires strung tangentially around the beam pipe.*

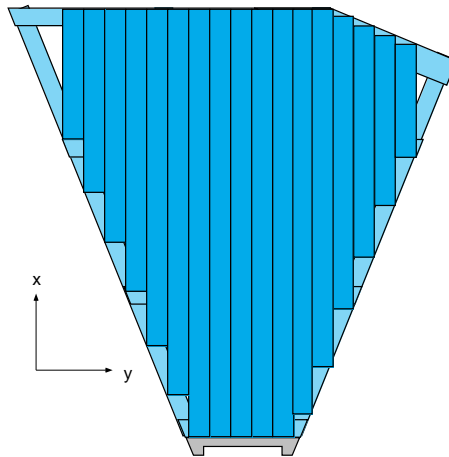


Figure 1.8: *Individual octant from a ϕ layer. Cells are mounted with the sense wires strung parallel to each other, and with the central wire strung radially.*

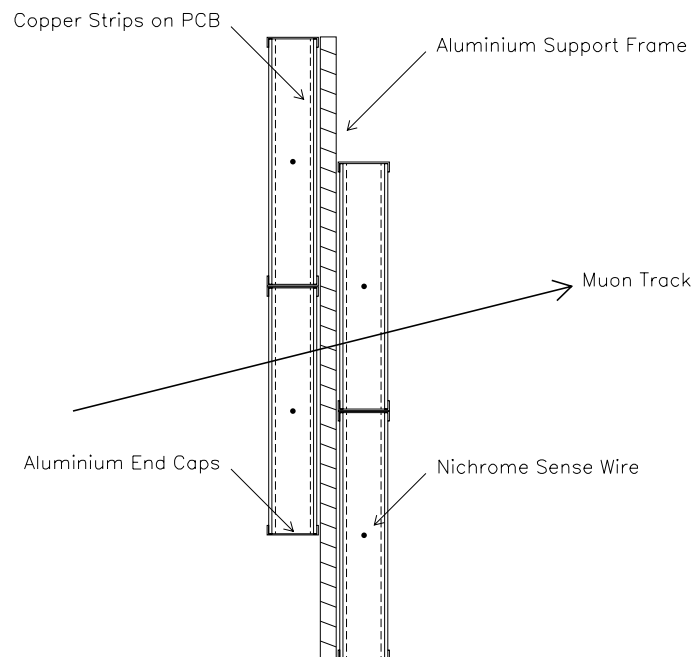


Figure 1.9: Arrangement of drift cells in the FMD.

1.6 The Luminosity System

The luminosity system must be able both to measure accurately the luminosity for cross section measurements, and provide a fast on-line luminosity measurement to enable the HERA machine group to steer the beams and become aware of problems. The luminosity is readily determined from the rate of the Bethe-Heitler process, $ep \rightarrow ep\gamma$, which has a large and calculable cross section. The luminosity monitor therefore needs to detect scattered electrons and outgoing photons in coincidence. It consists of an electron tagger and a photon detector and is shown in figure 1.10. Bremsstrahlung processes from the residual gas in the beam pipe ($eA \rightarrow eA\gamma$) form the most significant background, but these may be subtracted using data from the electron pilot bunches. The luminosity, L , is therefore given in terms of the total rate of bremsstrahlung processes, R_{tot} , and the rate due to pilot bunches, R_0 :

$$L = \frac{R_{tot} - (I_{tot}/I_0)R_0}{\sigma_{vis}} \quad (1.1)$$

where I_{tot} and I_0 are the total beam current and pilot beam current respectively, and σ_{vis} is the visible part of the $ep \rightarrow ep\gamma$ cross section, with the acceptance and trigger efficiencies included.

Whilst the on-line luminosity measurement is made by detecting the electron and photon in coincidence, the off-line measurement uses only the detected photon for the final total

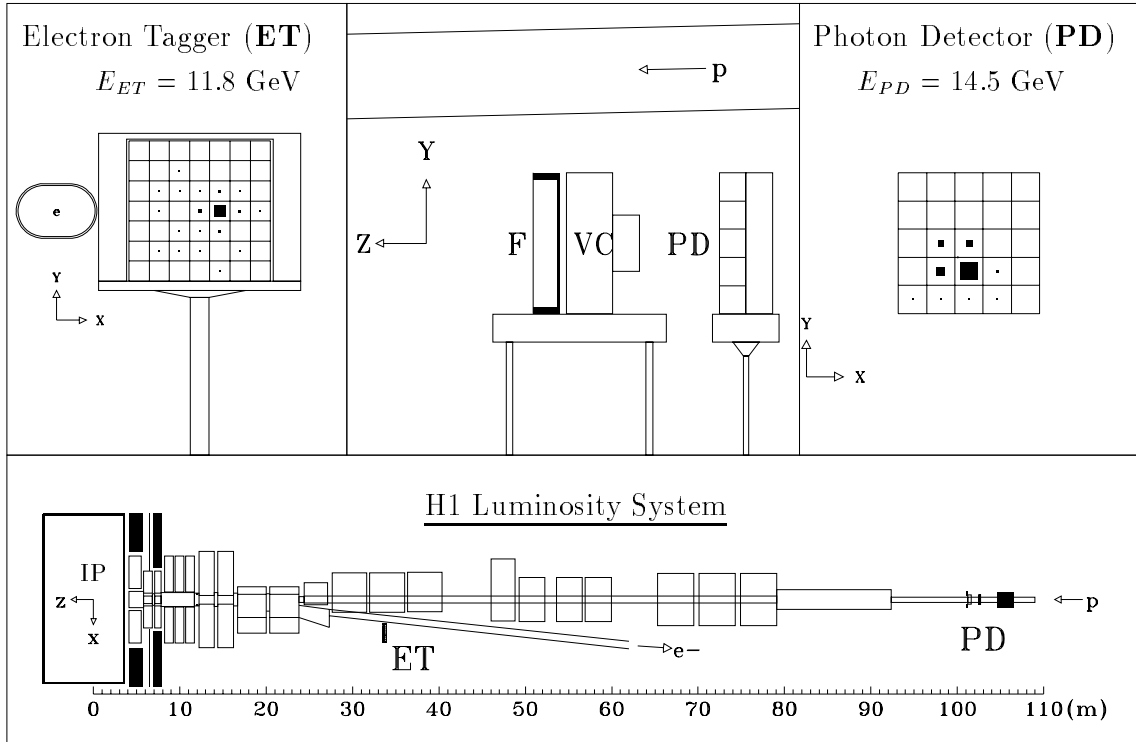


Figure 1.10: Schematic diagram showing the layout of the luminosity system. **ET** is the electron tagger, **PD** the photon detector, **F** is the lead filter, and **VC** the Čerenkov counter.

integrated luminosity. This method is used in order to keep the systematic error to a minimum. The determination of the luminosity at H1 is discussed in greater detail in [10]. The angular distribution of the process $ep \rightarrow ep\gamma$ is peaked along the direction of the electron beam, so the detectors need to be placed very close to the beam pipe. The electron tagger is positioned at 33 m downstream from the interaction point, has a polar angular acceptance of $0 < \theta < 5$ mrad, and accepts electrons with an energy fraction of the beam energy in the interval $0.2 \lesssim E_{e'}/E_e \lesssim 0.8$. This detector is also important in tagging and triggering on photoproduction events where the electron is scattered at very low angles, with $Q^2 < 0.01$ GeV². The photon detector is positioned at 103 m downstream from the interaction point, and is protected from the high synchrotron radiation flux by a lead filter. A water Čerenkov counter follows. The ET and PD consist of total absorption crystal Čerenkov counters, with an absolute energy calibration of precision better than 1%, and an energy resolution of approximately $15\%/\sqrt{E}$.

1.7 Timing Devices

Much of the background at H1 arises from interactions of the proton beam with the wall of the beam pipe, or with residual gas inside the beam pipe. The main task of the time of flight hodoscope (ToF) is to separate real electron proton collisions from this type of proton induced background. The ToF is positioned upstream of the interaction point, so that particles from background interactions which travel with the proton beam will give a signal in the ToF at a time $\sim z/c$ before the bunch crossing time, where z is the distance between the interaction point and the ToF and is approximately 2 m. Particles produced in an ep collision, however, give a signal at a time $\sim z/c$ after the bunch crossing, and in this way may be separated from the background by a device with good time resolution. The ToF consists of two planes of scintillator which are perpendicular to the beam axis. Each plane consists of a 3 cm layer of plastic scintillator sandwiched between 6.5 mm thick lead layers. The purpose of the lead is to protect the scintillator from synchrotron radiation, and limit the numbers of triggers which arise as a result of this background. The signals are read out by 24 photomultiplier tubes and then amplified and strobed into three time windows: background, interaction and global, and a signal is sent to be used in the first level trigger decision. The ToF has a resolution of 4 ns, compared with the time difference between signal and background of approximately $2z/c \simeq 13$ ns. In 1995, the ToF was replaced by the SPACAL (section 1.4.3).

In addition to this device, two double scintillator veto walls are positioned upstream of the interaction point at $z = -6.5$ m and $z = -8.1$ m. The purpose of these detectors is to identify upstream proton induced background events. The outer veto wall covers a region approximately equal to the iron endcap, and the inner wall covers the region near to the beam pipe, with a minimum radius of 11 cm. The outer and inner veto walls have resolutions of 8 ns and 3 ns respectively.

1.8 Triggering and Data Acquisition

A sophisticated triggering system is necessary at HERA to distinguish genuine electron-proton events from the high rate of background processes. The main background sources are photons from synchrotron radiation, interactions between the proton or electron beams and the residual gas in the beam pipe or the wall of the beam pipe, and cosmic rays. These background events outnumber interesting physics events by several orders of magnitude.

Bunch crossings occur every 96 ns at HERA, the first collider to operate at this high

collision rate. This creates a very challenging environment in which to operate, and to cope with the resulting high rates H1 uses a ‘pipelined’ trigger. If an event is triggered, the central trigger sends an ‘L1 keep’ signal to all the different subsystems. This occurs exactly 24 bunch crossings after the event. Rather than having H1 being essentially inactive whilst this process is taking place, the output from all the subsystems is stored in memory (pipelined) for this length of time. If the L1 keep signal is negative, then the output from the subsystems continues, and the information from this event simply falls off the end of the pipeline. A positive signal, however, freezes the pipelines so that the data from the triggered event may be transferred to the front end processors and read out. From the time when the L1 keep signal is sent until the read out is complete and the output has been sent to the central data acquisition, the detector is effectively disabled. This is what is known as the ‘dead time’, and lasts for 1-2 ms per event. H1 uses a multilevel trigger system to reduce the dead time as much as possible. Further trigger decisions can be made at levels 2 and 3 (L2 and L3) to abort the readout if the event is identified as background. This takes approximately 20 μs for L2 and 800 μs for L3.⁵

The output from each subdetector is sent to the subdetector trigger systems, which subsequently output typically 8 bits of information, the trigger elements, to the central trigger, where a level 1 (L1) decision is made. At L1, the central trigger takes logical combinations of the trigger elements from all subdetectors and tests them against a set of predefined subtriggers. There are 128 different subtriggers, most of which are designed to trigger on classes of physics events, and a few which are used to obtain samples of background events, *eg.* cosmic or beam halo muons. These latter triggers are known as monitor triggers. If a trigger fires at too high a rate, it may have a ‘prescale factor’ applied to it. The prescale factor defines how many times a particular subtrigger condition must be met before an event is read out. In general, physics triggers are not prescaled if at all possible, whilst monitor triggers have high prescale factors.⁶

At level 4 (L4), a highly simplified version of the full reconstruction is performed by a farm of fast processors online. This rejects events from beam-gas and beam-wall interactions, and events accepted at L1 as a result of trigger noise. Approximately 30% of physics triggers from L1 survive the L4 cuts.

Events which have passed L4 are written to semi-permanent storage on disk and are fully reconstructed off-line by the H1 reconstruction software package H1REC and put on to ‘production output’ (POT) tapes. Further data reduction takes place when the the events

⁵L2 and L3 were not active during the data taken which was used in the analysis presented in this thesis.

⁶During 1995, difficult background conditions were experienced and some physics triggers were kept at a high prescale throughout the running period.

are written in a space-saving, convenient form for analysis, on to data summary tapes (DST's).

Chapter 2

Calibration and Alignment of the Forward Muon Detector

2.1 Introduction

The forward muon detector was described in section 1.5. This chapter will discuss the reconstruction of both the position of the hits in the drift cells, and of tracks passing through the whole detector. In order to perform this reconstruction, detailed knowledge of certain calibration constants (the global T_0 and the drift velocity) is essential. The determination of these constants is described in this chapter, followed by an investigation of the variation of the drift velocity with changing drift voltage. The results of the monitoring of the T_0 and the drift velocity over the 1994 and 1995 running are shown. The calibration constants discussed facilitate the reconstruction of the position of a hit within the drift cell itself, but in order to reconstruct the global position of a hit, detailed knowledge of the exact positions of each octant is crucial. The final sections of this chapter will cover the alignment of the layers of the FMD, using both physical surveys and cosmic muon data, together with tests of the alignment procedure using Monte Carlo data.

2.2 Reconstruction in the FMD

2.2.1 Qt Analysis

The Qt analysis takes place online once an event has been triggered. It analyses the digital pulses from the FADC's and returns information on the time of arrival of a pulse (relative to the appropriate bunch crossing) and on the integrated charge at the two wire

ends. The pulses have a steeply rising edge followed by a long tail, and the further the pulse has travelled along the wire, the flatter it becomes in shape. In order for a pulse to be recognised, the Qt algorithm requires that it must pass a certain threshold (which is set above the noise level) for two consecutive time bins. A straight line is fitted to the rising edge of the pulse, and extrapolated back to the pedestal level to find the arrival time of the pulse. It is the average of the arrival times for the pulses at each wire end which is taken as the raw drift time. The charge integration is done over 8 time bins following the arrival of the pulse.

2.2.2 Space-point reconstruction

In order to reconstruct a muon track it is necessary to convert the raw times and charge information, given by the Qt , to space points. The distance along a sense wire (the x coordinate in the local coordinate system of the FMD) is determined from charge division, by comparing the integrated charge from both ends of the wire, Q_1 and Q_2 :

$$x \propto \frac{Q_1 - Q_2}{Q_1 + Q_2} \quad (2.1)$$

This process gives a distance which is accurate to within a few percent of the total wire length. Both this and the Qt analysis are discussed in greater detail in [12].

The drift distance (the y coordinate) is the distance between the sense wire and where the muon passed through the drift cell. This is found using the raw drift time information, and the resulting y -resolution is of the order of $350 \mu\text{m}$.

The time of arrival of the pulse is dependent not only on the time it takes the charge to drift to the sense wire, but also on the time of flight from the interaction point, and on the time taken for the the pulse to propagate down the sense wires and the cables. The time of flight is simply accounted for by knowledge of the distance from the drift cell to the interaction point, but the latter effect causes relative time differences between the cells due to differing wire lengths. These relative time differences may be found from test pulse runs, which involve sending test pulses from the FADC's at a fixed time to the pre-amplifiers of every cell in the FMD chambers. The measurement of arrival times for the pulses allows calibration for the relative T_0 's of each cell pair. In this way, the raw drift times may be converted to a corrected time, T_{corr} , and the drift distance is then given by the simple equation:

$$y = v \times (T_{corr} - T_0) \quad (2.2)$$

where T_0 is a constant, global correction, which can be explicitly defined as the corrected time obtained for a muon passing very close to the sense wire. The drift velocity, v , is

the speed at which primary electrons move through the gas in the drift cell.

2.2.3 Track reconstruction

The first stage in reconstructing a forward muon track [13] involves matching the hits in adjacent planes of each octant into pairs. This is done by looking at the distance between any two hits in x (the charge division coordinate) and in y (the drift distance). If these separations are greater than some maximum allowed values then the two hits are not paired. The formation of hits into pairs solves the left-right ambiguity in the drift coordinate. The second stage of reconstruction combines the pairs into segments, either in layers θ_1 and θ_2 before the toroid, or in layers θ_3 and θ_4 after the toroid. At least one pair is required to form a segment, and the second component may be a pair or an unpaired drift ambiguous hit. Each hit in the segment is fitted to a straight line using a least squares fit, and a maximum χ^2 cut is placed on the segment. In the case where two segments are fitted with the same drift ambiguous hit, the segment with the lowest χ^2 is retained. The final process is the formation of segments into tracks, and it is here that the measurement of momentum is made. Each segment is extrapolated to the centre of the toroid in a straight line, and if two segments are close together in r and ϕ they are considered as track candidates, and all other segments are rejected. The segments remaining are then extrapolated through the toroid from the side with the least number of track candidates. Segments are extrapolated over a range of momentum values, taking account of both the bending in the magnetic field and energy losses inside the toroid. The coordinate information for both segments (one extrapolated) on the same side of the toroid is compared, and a χ^2 formed. The charge and momentum value are taken for the track which gives the minimum χ^2 for the fit.

2.3 Determination of the calibration constants

From equation 2.2 it is clear that good resolution in the reconstruction of the drift coordinate, y , is dependent on an accurate knowledge of the global T_0 and of the drift velocity. This velocity is dependent on the electric field in the cell, the gas mixture used, and on the pressure of the gas. The drift distance resolution is directly proportional to the time resolution of the FADC's, so if the velocity rises, the resolution is reduced. However, if it is too low, then the pulses may arrive outside the FADC time bin window and not be read out, or not give enough time for the L1 trigger to make a decision for an event.

Determination of both v and T_0 requires a large sample of muons in time with the HERA

clock¹, triggered by the H1 central trigger and free from background. Physics muons were considered unsuitable because of the large background and small rate, and cosmic muons could not be used as they are out of time with the HERA clock. The studies described in this chapter were carried out using beam halo data. High energy ‘beam halo’ muons are produced when the proton beam interacts with the beam wall. They follow the beams in the proton direction, and generally penetrate the whole of the H1 detector, including the FMD. Although this type of event clearly creates background for physics events, the beam halo muons are easily identified, and are very useful for calibration purposes. There are two monitor triggers which use the veto walls (section 1.7) to identify beam halo events. These are kept at a high prescale and collect beam halo data throughout the running period. All the beam halo data available for the 1994 and 1995 running periods was analysed.

2.3.1 The Drift Velocity

The drift velocity may be determined from the time distribution of the hits [14]. An ideal drift cell would have constant drift velocity across the whole volume, but in reality this is limited to the central region of the drift space. Hence the hits produce a top hat distribution which is smeared at the edges, as shown in figure 2.1. This smearing is partly due to a non-zero spatial resolution. The regions of a drift cell where the drift velocity is not constant occur as a result of a non-uniform electric field at the edges of the cell and very close to the sense wire. In determining the drift velocity, the central region of the time distribution which is constant is chosen, as this corresponds to a region of constant drift velocity. If the number of events within this region is N_{mid} , the length of the chosen region is D_{mid} , and the total number of events is N , then

$$D_{mid} = \frac{N_{mid} \cdot D}{N}, \quad (2.3)$$

where D is the total drift length ($D = 6.000 \pm 0.023cm$). Since the drift velocity, v is constant and it is clear that

$$v = D_{mid} / \Delta T. \quad (2.4)$$

Therefore,

$$v = \frac{N_{mid} \cdot D}{N \cdot \Delta T}, \quad (2.5)$$

where ΔT is the length of the chosen region in time.

The large peak in the first time bin of the time distribution, shown in figure 2.1, occurs as a result of using a T_0 which is too large in the reconstruction. Since the T_0 must be

¹The HERA clock is a standardised frequency sent out by HERA so that the experiments may be synchronised with the bunch crossing times.

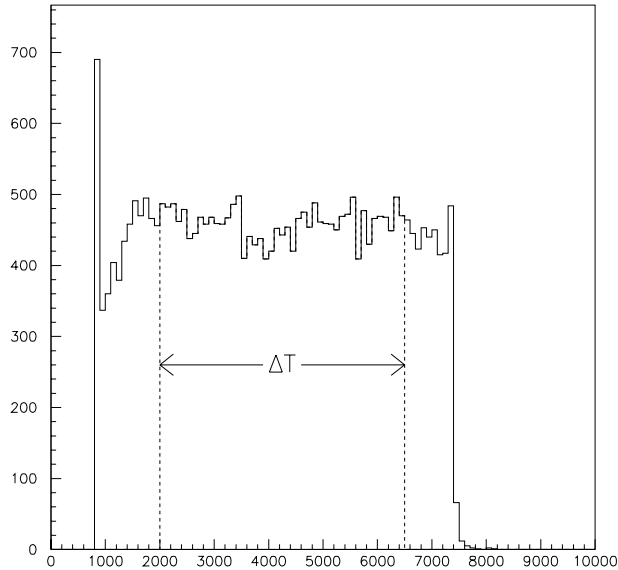


Figure 2.1: *Time distribution of the hits. The dotted lines show the middle range used to calculate the drift velocity. The time-scale is shown in ticks, where 50 ticks \equiv 9.6 ns.*

subtracted to give the corrected drift time (equation 2.2), the value for this corrected time may be less than zero if the T_0 is too large. When this occurs, the events fall into the first time bin. This does not effect the determination of drift velocity, since it is simply the ratio of the number of events in each region which is used in the calculation. Similarly, the effect of smearing at the edges of the time distribution should not affect the measurement.

2.3.2 Determination of the T_0

The determination of T_0 is done in two stages. Firstly, the value of T_{mid} is calculated, where the T_{mid} is defined as the drift time for half the maximum drift distance. The value T_{mid} can be measured in one of two ways. It can be taken as the mid-point of the time distribution, or, more accurately, determined using a checksum [14]. This method involves comparing the drift times (or y -coordinates) as measured by the different sublayers. In order to measure the T_0 , a pre-toroid segment from layers θ_1 and θ_2 may be used, or a post-toroid segment from layers θ_3 and θ_4 . Depending on the ‘stagger’ permutation of the cells, demonstrated in figure 2.2, this method yields two possible checksums. The first is derived from the ‘unlike stagger’ and is used to find the T_0 . It can be seen from the left hand diagram in figure 2.2 that the sums of drift time, as measured in the sublayers of θ_1

and θ_2 , are related to the total drift distance by the following equations.

$$\begin{aligned} v(T_1 - T_0 + T_2 - T_0) + \Delta z \cdot \tan(\theta) &= D, \\ v(T_3 - T_0 + T_4 - T_0) - \Delta z \cdot \tan(\theta) &= D, \end{aligned} \quad (2.6)$$

where θ is the angle of the muon track, and Δz is the difference in z between the two sublayers. By summing these two equations, an expression for the T_0 is obtained in terms of the sum of the drift times. This is what is meant by a ‘checksum’.

$$T_1 + T_2 + T_3 + T_4 = \frac{2D}{v} + 4T_0. \quad (2.7)$$

The quantity T_{mid} is then defined by the checksum

$$T_{mid} = \frac{1}{4}(T_1 + T_2 + T_3 + T_4). \quad (2.8)$$

T_{mid} is obtained from the mean of a plot of the above checksum (see figure 2.3), and once the drift velocity is known, then the T_0 is given by the simple equation

$$T_0 = T_{mid} - \frac{D}{2v}. \quad (2.9)$$

Similarly, the geometry of the ‘like stagger’, shown by the right hand diagram in figure 2.2 gives the checksum

$$Y_1 + Y_2 - Y_3 - Y_4 = 0. \quad (2.10)$$

This may be written in terms of Y rather than T as they are related by equation 2.2, and the terms containing the T_0 simply cancel. A plot of the checksum gives an approximately Gaussian distribution, the width of which gives the spatial resolution in the drift coordinate, y_{res} . From figure 2.4, the resolution obtained was

$$y_{res} = 376 \pm 9\mu\text{m}. \quad (2.11)$$

The non-zero mean of the checksum shown in figure 2.4 is a result of the effects of misalignment of the layers in the FMD.

2.4 Variation of Drift Velocity with Voltage

Studies were carried out at Manchester University [15], using a test cell similar to the drift cells in the FMD, in order to investigate the variation of the drift velocity with pressure and drift field. It was shown that the drift velocity varies with E/p (where E is the drift field and p the pressure of the gas in the cell) such that it rises to a maximum and then falls off at higher E/p . At the ‘plateau’ of the curve, slight variations in field or

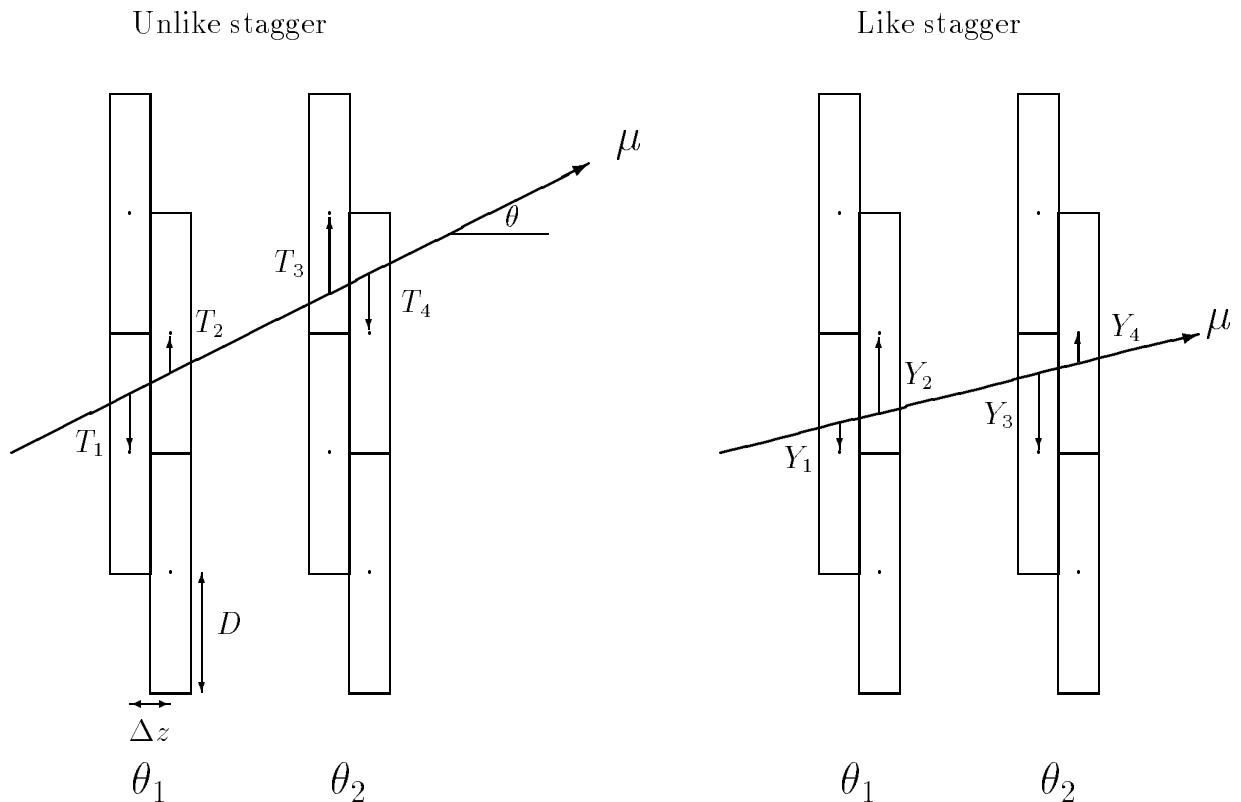


Figure 2.2: The two possible stagger permutations of the cells, for a segment through two layers.

pressure should not greatly affect the drift velocity. Figure 2.5 shows a simulation of this drift velocity curve, where the conditions have been chosen to match those of the drift chamber in the FMD at H1.

Changes in the atmospheric pressure affect the pressure of the gas inside the FMD, hence if the drift cells are not operating at the plateau of the drift velocity curve, daily or even hourly changes in the pressure could affect the drift velocity. The rate at which beam halo data is taken does not give sufficient statistics to allow calibration of the FMD over such a short time-scale. A study was therefore carried out to investigate the change in drift velocity with voltage to ascertain exactly where on the drift velocity curve the cells are actually operating. For normal data taking, the FMD operates with its drift cells at a voltage of 2880 V, but for the purposes of this study, special runs were taken of beam halo muons, where each of the four quadrants had voltages at different settings (H.V. set up (1) in table 2.1). In this manner, any systematic effects, such as changes in atmospheric pressure, may be safely neglected since all the data is taken at the same time with the only differences being the different voltage settings in the different quadrants. To account for any systematic differences which may exist between the octants, further runs were

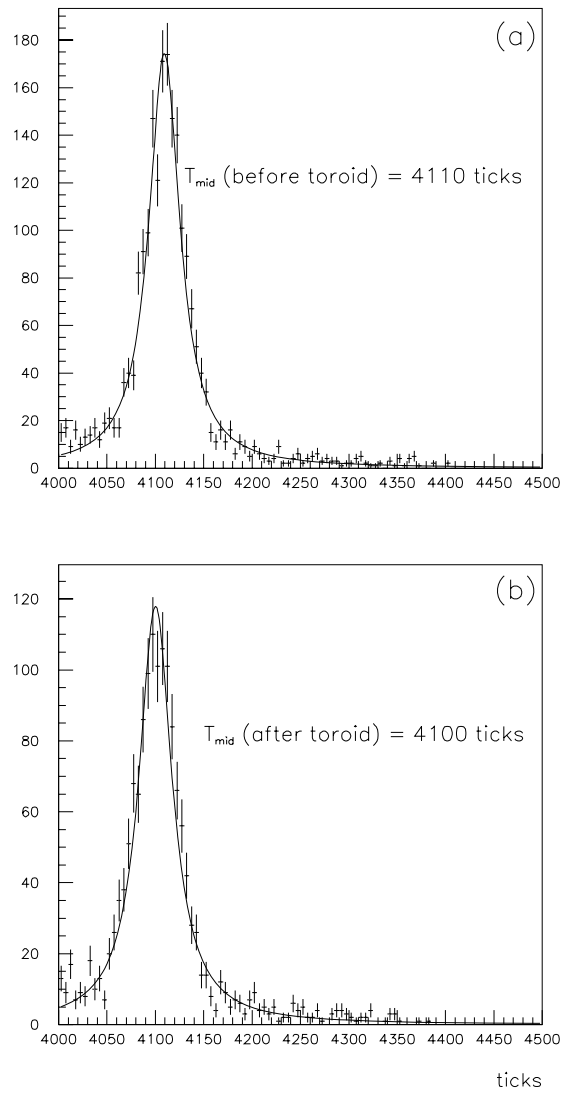


Figure 2.3: Checksums for T_{mid} ; (a) before and (b) after the toroid.

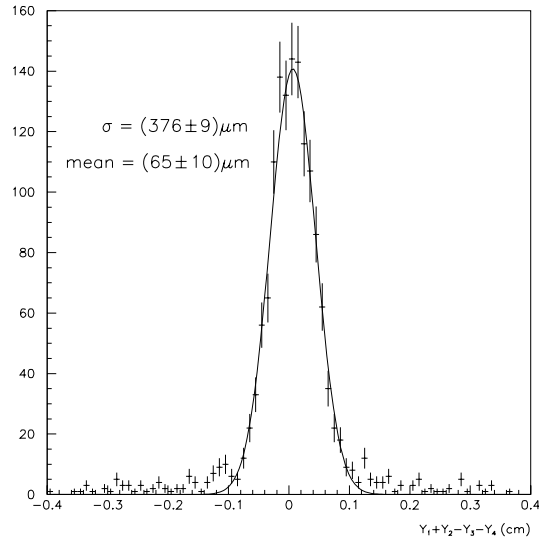


Figure 2.4: Checksum used to determine the resolution of the drift coordinate. Segments before the toroid were used in this case.

taken with the voltage settings rotated (H.V. set up (2) in table 2.1).

Quadrant	Octants	Drift Voltage (V)	
		H.V set up (1)	H.V. set up (2)
1	2,3	3080	2480
2	3,4	2880	3080
3	5,6	2680	2880
4	7,8	2480	2680

Table 2.1: The two voltage set ups for the drift velocity vs. voltage scan.

Beam halo muons are asymmetrically distributed in ϕ and tend to lie in the $y = 0$ plane, which leads to an asymmetric distribution of hits in the forward muon chambers. This effect is seen in the hit map of the θ layers of the FMD shown in figure 2.6. The octants 1, 4, 5 and 8 have the most even and fully populated distribution, and therefore give the most reliable values for a drift velocity calculation. These octants were therefore used to examine the variation of the drift velocity with voltage. The pattern of horizontal stripes visible on the hitmap is an effect of an inefficiency in the iron rather than the FMD. The structure in the lower left hand octant which lies parallel to the outer edge of the octant is the result of a dead cell.

The results of this study are presented in figure 2.7, showing a clear rise of drift velocity with voltage which appears to become more gradual as the voltage increases. This may be compared with figure 2.8, in which the drift velocity is calculated for the same octants,

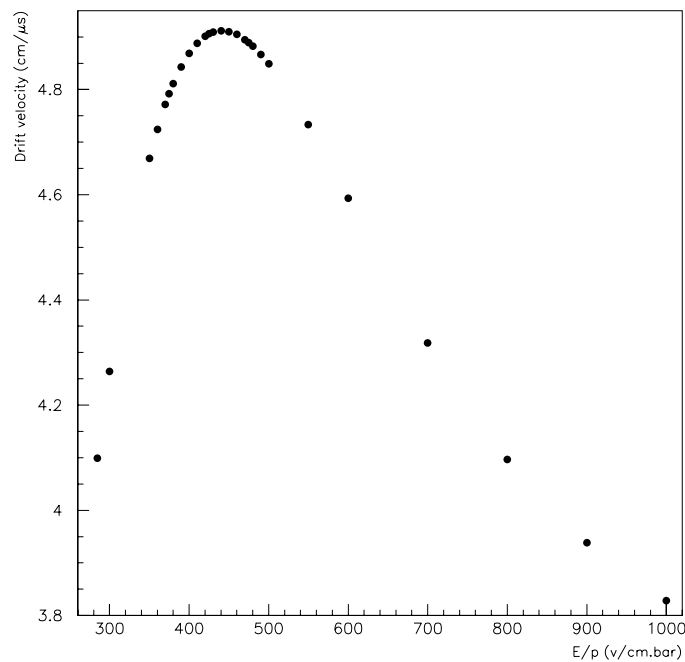


Figure 2.5: Simulation of the variation of drift velocity with E/p , where E is the drift field and p is pressure of the gas.

where the voltages are at their standard settings, *ie.* the same for every octant. The standard operating drift voltage of the FMD, 2880 V, corresponds to the third point on the curve in figure 2.7. The errors on the plots are statistical only and do not include any systematic effects which may arise from, for example, the breakdown of the assumption of a uniform drift field across the cell. The level of systematic error is revealed by the measurements of the drift velocity from quadrants which are all at the same voltage. In figure 2.8 the points lie on a straight line, within the statistical errors.

From the curve shown in figure 2.7, it seems that the FMD is operating near the plateau of the drift velocity curve. To investigate whether the curve then turns over and starts decreasing at higher voltages was not possible, because running the detector at yet higher voltages presents a risk of severely damaging the chambers. It is important therefore, that the drift velocity is monitored as closely as possible during running periods, so that any changes may be accounted for. This is discussed in the next section.

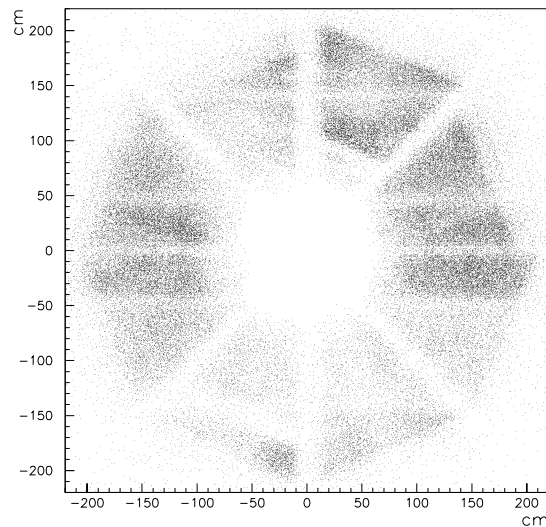


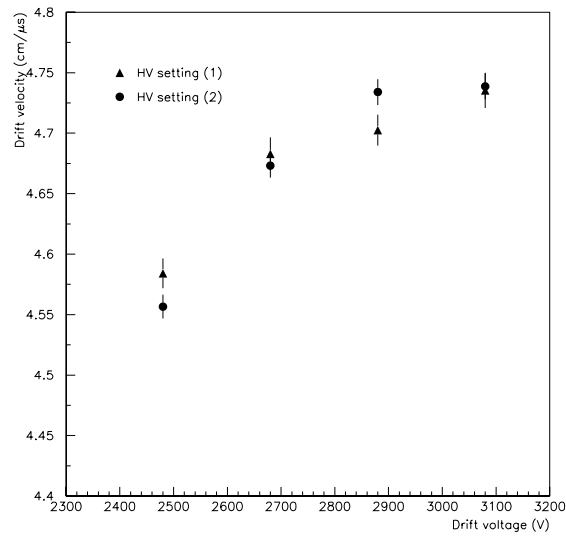
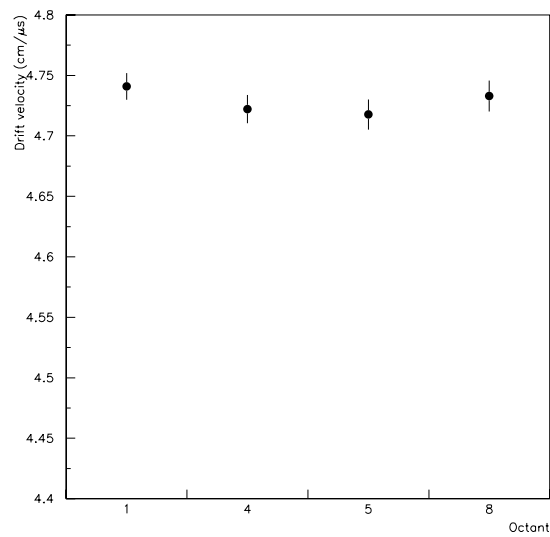
Figure 2.6: *Hit map of the θ layers of the FMD (from beam halo data).*

2.5 Monitoring of 1994 and 1995 Data

In order to achieve the best possible calibration of the FMD, the drift velocity and T_0 were monitored during all of the 1994 and 1995 running periods, and the values for these calibration constants were entered in the database on a run dependent basis. This was achieved by calculating the drift velocity and T_0 from consecutive samples of beam halo data taken over a period of several runs, which was necessary to ensure that there were enough statistics. In this way, all the beam halo data for 1994 and 1995 was analysed. The variation of the drift velocity and the T_0 over the full running periods are shown in figures 2.9 and 2.10.

The gap in results between runs 87297 and 88367 in figure 2.9 corresponds to the period when the forward muon detector was not fully operational. During this time the FMD experienced problems with synchrotron radiation flooding the chambers, causing high currents and frequent trips. In order to prevent damage being caused to the detector, the chambers of θ_4 were switched off for much of this time. Also, the points in the period between runs 82005 and 82962 are not reliable because this was the period in which the change over was made from running with electrons to running with positrons. The value of the T_0 shows a clear jump around 88400, and this is due to changes made to the FADC and readout electronics.

In figure 2.10 the results from the 1995 monitoring can be seen. Runs after 122292 correspond to data taken after the installation of new mass flow meters to monitor the

Figure 2.7: *Variation of drift velocity with voltage*Figure 2.8: *Drift velocity per quadrant at constant voltage*

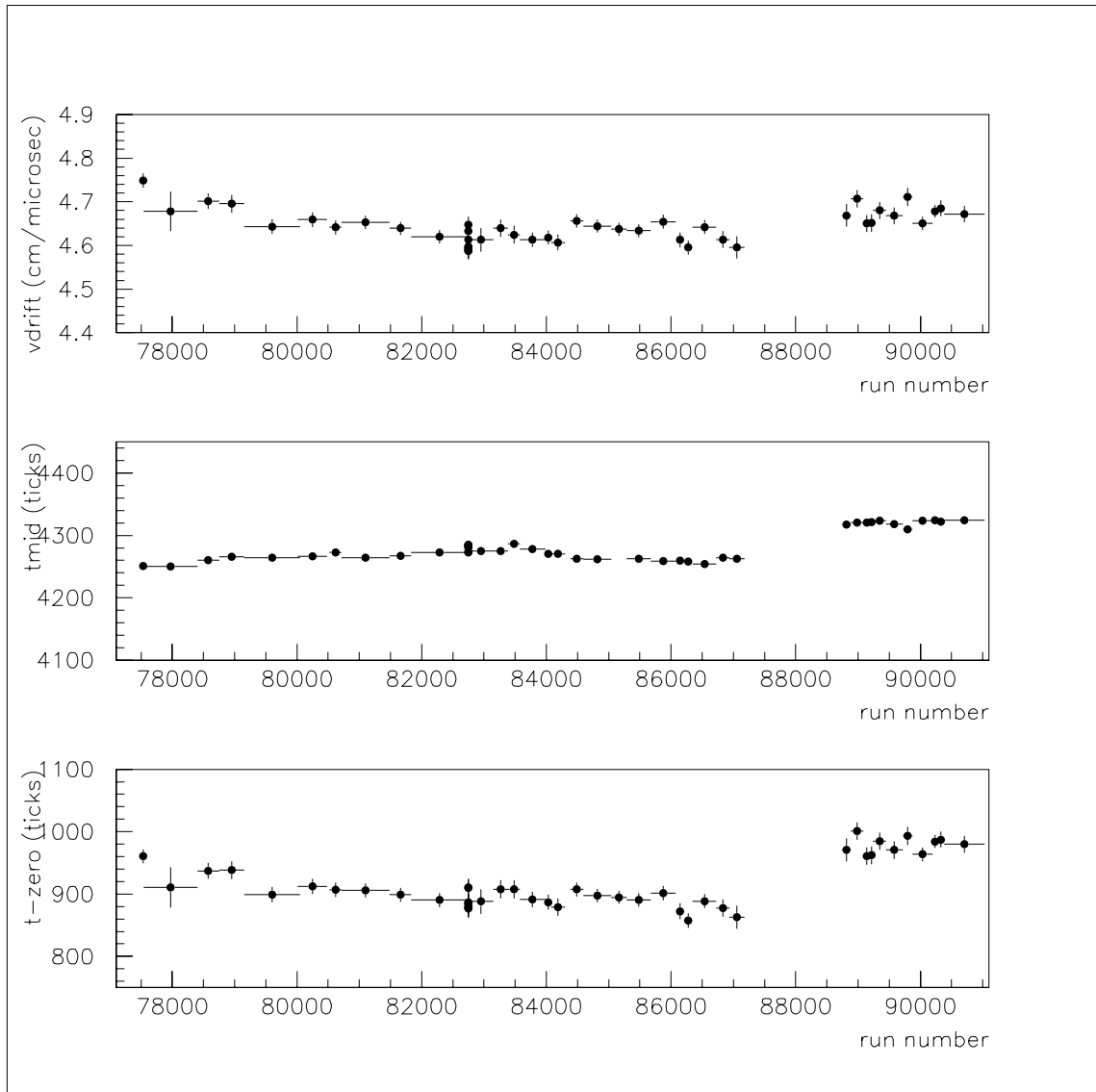


Figure 2.9: Plots showing the variation of drift velocity, T_{mid} and T_0 over the 1994 run period. The vertical error bars show statistical errors, and the horizontal bars refer to the period of runs over which the quantity was determined.

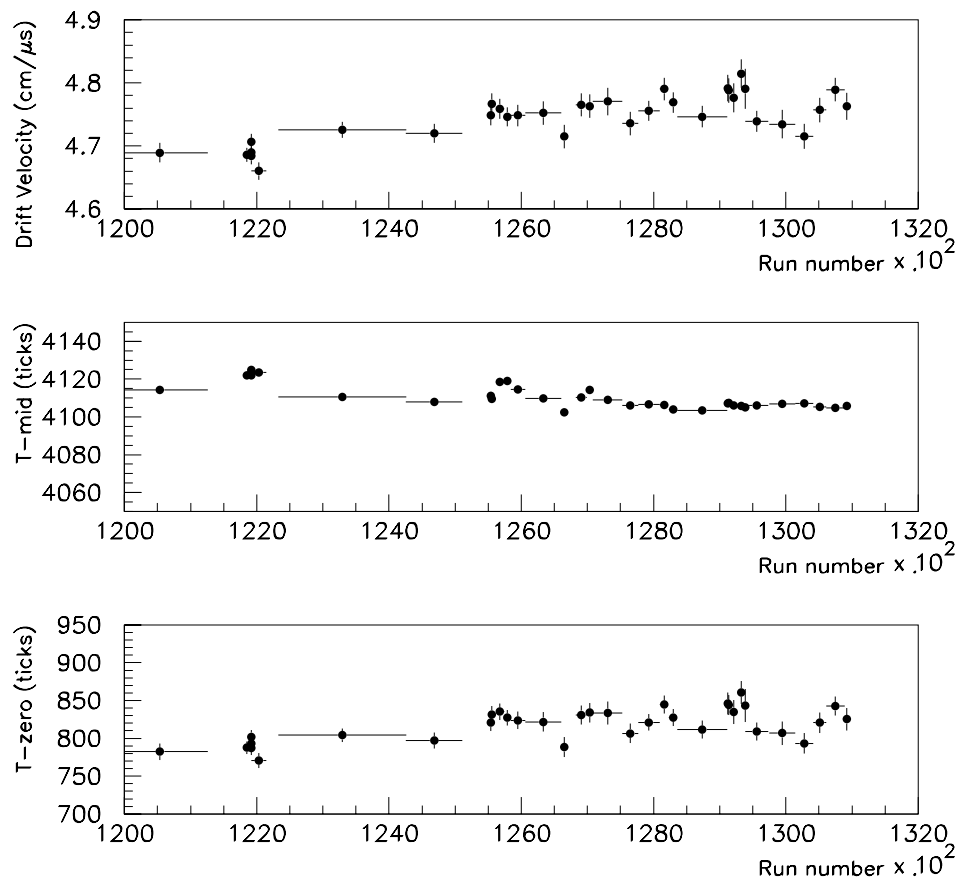


Figure 2.10: Plots showing the variation of drift velocity, T_{mid} and T_0 over the 1995 run period. Only the period where useful physics data was being taken is shown.

gas. It is important to ensure that the gas composition remains steady over the run period; changes in this, such as a slow leakage of oxygen into the system, will affect the drift velocity. After this time it can be seen that the drift velocity and T_0 are very stable and vary by only approximately $\pm 1\%$ and $\pm 3\%$ respectively over the remaining data taking period.

2.6 Alignment of the FMD

Although the drift cells and sense wires are aligned precisely parallel and are positioned on an octant to within an accuracy of approximately $50\ \mu\text{m}$ perpendicular to the wire direction, the movement of the octants on the door frames (as required to allow access to the detector) has resulted in the octants within a layer becoming misaligned by the order of a cm or more. Translational misalignments may occur along the beam direction and laterally with respect to the nominal positions, and there may also be rotational misalignments. Determination of the exact misalignment of each octant relative to others, to within the resolution of the detector, is necessary to exploit the potential precision for momentum measurements.

Alignment of the forward muon detector can be carried out in two ways:-

- A physical survey.
- Using tracks passing through the detector.

In practice, a mixture of both these methods is used. Physical surveys provide an essential starting point for the alignment procedure, but are difficult due to the crowded environment around the forward muon system. However useful measurements have been made of the relative z -positions of the theta layers, and of their positions relative to the toroid. These measurements are made at three different points on each octant, thus allowing the rotational misalignments around the x and y axes to be determined, as well as the translational misalignments in z , relative to the toroid.

In order to determine translational misalignments in x and y it has been necessary to study tracks passing through the detector. The requirements for this study are a large number of straight tracks passing through corresponding octants in each layer, covering the full area of each octant. Cosmic muons are therefore best suited for the purposes of alignment. The study requires straight tracks through all the layers of the FMD, so

the toroid was switched off and degaussed. Dedicated runs of cosmic muons were taken, triggered on the forward muon trigger, subtrigger 16.

The following sections deal with the techniques used to calculate alignment values, results obtained, and various checks carried out to ensure the validity of the values subsequently entered in the database.

2.6.1 Physical Surveys

Physical surveys of the FMD [16] were carried out both before and after the data taking period, whilst the chambers were still in place and had not been withdrawn to allow access to the toroid. The purpose of these surveys was to measure the relative z displacements of the octants. Measurements were made of the distance between the layers θ_1 and θ_2 , θ_2 and the toroid, the toroid and θ_3 , and θ_3 and θ_4 . They were made between three different points on corresponding octants, using a two metre rule which was accurate to approximately 1 mm. The z position of the toroid is well known, so that the z positions of each octant in each layer can therefore be determined. The plane of the octant is defined by the three points measured. The z positions of the ϕ octants were similarly determined in the most recent survey by measurements taken between the ϕ and θ layers. Due to difficulties with access however, only certain points on some octants could be measured.

Misalignments of the octants are taken into account during the reconstruction. Once the positions of the hits have been reconstructed in the local coordinate system of the FMD, the local coordinates are then transformed to the tilted frames of the individual octants. This is done by a rotation, θ , about the x axis and a rotation, ϕ , about the y axis at a fixed point at the bottom of each octant, and also translations, Δx , Δy and Δz . The angles θ and ϕ , as well as the translational alignment value Δz , are all determined for the measurements taken in the survey of the FMD. Determination of the quantities Δx and Δy , however, requires further studies of the detector using muons passing through it.

2.6.2 Checksum Method

Translational misalignments in x and y were determined by a checksum method [14],[17], using a large sample of cosmic muons. This method however, only gives relative values of misalignments, so in order to calculate absolute positions it has been necessary to assume that theta layers 2 and 3 have perfect alignment in x and y . To a certain extent, this decision is arbitrary, although it is thought that these layers are more likely to be well

aligned with respect to H1. As long as the forward muon detector is aligned with respect to some internal coordinate system, the momentum measurement should not be affected, and any errors in alignment with respect to H1 should be small enough so that linking of forward muon tracks to tracks in other parts of the detector is not affected.

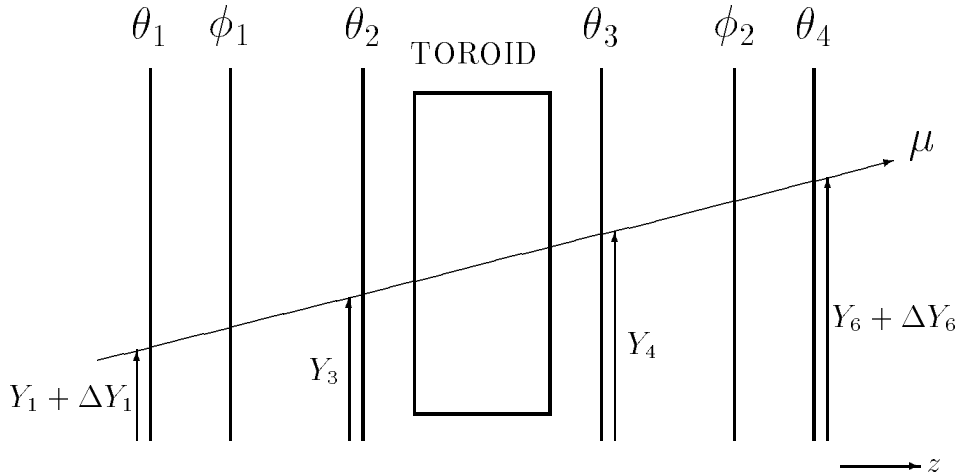


Figure 2.11: Schematic diagram of the FMD to show the checksum method of aligning the chambers. For the purposes of calculating the checksums, the layers are numbered 1-6, such that 1,3,4 and 6 are the θ layers, whilst 2 and 5 are the ϕ layers.

The principle behind this method simply lies in comparing the gradients of different segments of a straight track. The gradient measured from $\theta_1 \rightarrow \theta_2$ should be the same as $\theta_2 \rightarrow \theta_3$, and similarly for $\theta_3 \rightarrow \theta_4$. Taking, for example, theta layer 1, this is expressed in the simple relation

$$\frac{Y_3 - Y_1 - \Delta Y_1}{Z_3 - Z_1} = \frac{Y_4 - Y_3}{Z_4 - Z_3}, \quad (2.12)$$

where ΔY_1 is the misalignment in y of one particular octant of theta layer 1. It can therefore be seen that a plot of the checksum

$$\Delta Y_1 = (Y_3 - Y_1) - (Y_4 - Y_3) \frac{(Z_3 - Z_1)}{(Z_4 - Z_3)}, \quad (2.13)$$

should have a mean centred on the misalignment in y for theta layer 1, ΔY_1 . Large smearing effects occur due to the resolution of the chambers and multiple scattering in the iron toroid, and so high statistics are needed to give a good accuracy on the mean, ΔY_1 . In order to achieve this, a sample of approximately 100000 cosmic muons was used. The various checksums used to determine the misalignment values in both x and y for θ layers 1 and 4, and for both ϕ layers are listed in table 2.2. Only tracks which pass through the same octant in each layer are used for alignment, so that this procedure may be repeated to calculate the misalignments for each octant individually.

Misalignment quantities	Checksums used
$\Delta Y_1 (\theta_1)$	$(Y_3 - Y_1) - (Y_4 - Y_3) \times (Z_3 - Z_1)/(Z_4 - Z_3)$
$\Delta Y_2 (\phi_1)$	$(Y_3 - Y_2) - (Y_4 - Y_3) \times (Z_3 - Z_2)/(Z_4 - Z_3)$
$-\Delta Y_5 (\phi_2)$	$(Y_5 - Y_4) - (Y_4 - Y_3) \times (Z_5 - Z_4)/(Z_4 - Z_3)$
$-\Delta Y_6 (\theta_4)$	$(Y_6 - Y_4) - (Y_4 - Y_3) \times (Z_6 - Z_4)/(Z_4 - Z_3)$
$\Delta X_1 (\theta_1)$	$(X_3 - X_1) - (X_4 - X_3) \times (Z_3 - Z_1)/(Z_4 - Z_3)$
$\Delta X_2 (\phi_1)$	$(X_3 - X_2) - (X_4 - X_3) \times (Z_3 - Z_2)/(Z_4 - Z_3)$
$-\Delta X_5 (\phi_2)$	$(X_5 - X_4) - (X_4 - X_3) \times (Z_5 - Z_4)/(Z_4 - Z_3)$
$-\Delta X_6 (\theta_4)$	$(X_6 - X_4) - (X_4 - X_3) \times (Z_6 - Z_4)/(Z_4 - Z_3)$

Table 2.2: Table showing checksums used to determine misalignment values.

2.6.3 Results

Examples of four of the checksums used are shown in figure 2.12. The checksums shown are for tracks passing through octant 1 only. The broader peak for alignment in x in the θ layers is a result of the lower resolution in the x (charge division) coordinate, whilst for the ϕ layers the checksum in x gives the narrower peak as in this case it is the drift coordinate.

The translational alignment values calculated using this method are shown in table 2.3.

The same cosmic muon data sample was reconstructed a second time using the alignment values shown in table 2.3, and then the alignment procedure was repeated once more. The translational alignment values obtained were all zero within errors, hence no further improvements could be made by repeating the process iteratively. Examples of four of the checksums plotted from this procedure are shown in figure 2.13.

2.6.4 Checks on the alignment procedure

In order to ascertain whether the checksum method of calculating misalignments was effective, a study was carried out using a sample of 25000 simulated cosmic muons, with momenta ranging between 5 and 50 GeV, and angular range of $0^\circ < \theta < 30^\circ$. The field in the toroid was off for this sample of muons, as it would be for real cosmic muons used to calculate the alignment values. The effect of misalignment in the FMD is not included in the simulation, so misalignments were introduced by reconstructing the simulated hits using a set of random misalignments (for layers θ_1 , ϕ_1 , ϕ_2 and θ_4) in place of the usual alignment bank. Rotational misalignments were introduced of values typical of the size of the errors on the rotational misalignments calculated from the z -measurements of the FMD, but for the purposes of this study, the translational misalignments in layers θ_2 and

Layer	Octant	Misalignment quantity (in cm)	
		ΔY	ΔX
θ_1	1	$+2.217 \pm .006$	$+1.92 \pm .09$
	2	$+1.035 \pm .005$	$+2.83 \pm .06$
	3	$+0.455 \pm .006$	$-0.84 \pm .06$
	4	$+0.495 \pm .006$	$-0.21 \pm .07$
	5	$+0.163 \pm .005$	$+0.88 \pm .09$
	6	$+0.085 \pm .006$	$-0.53 \pm .06$
	7	$+0.938 \pm .005$	$-1.97 \pm .06$
	8	$+2.269 \pm .006$	$-0.49 \pm .08$
ϕ_1	1	$+1.73 \pm .11$	$+4.86 \pm .08$
	2	$+1.13 \pm .14$	$-1.98 \pm .09$
	3	$+0.79 \pm .11$	$+2.72 \pm .06$
	4	$+2.89 \pm .12$	$-4.07 \pm .07$
	5	$+1.76 \pm .11$	$+4.46 \pm .09$
	6	$+1.07 \pm .09$	$-1.77 \pm .06$
	7	$+0.69 \pm .12$	$+1.54 \pm .07$
	8	$+1.89 \pm .13$	$-3.86 \pm .08$
ϕ_2	1	$+0.39 \pm .08$	$+1.81 \pm .10$
	2	$-0.30 \pm .10$	$+2.52 \pm .06$
	3	$+0.91 \pm .08$	$-2.19 \pm .07$
	4	$+1.97 \pm .11$	$-4.38 \pm .08$
	5	$+3.84 \pm .09$	$+2.86 \pm .08$
	6	$+3.31 \pm .07$	$+0.90 \pm .07$
	7	$+1.15 \pm .07$	$+1.27 \pm .07$
	8	$+1.65 \pm .14$	$-2.73 \pm .08$
θ_4	1	$-2.370 \pm .007$	$-1.98 \pm .11$
	2	$-1.729 \pm .005$	$-3.26 \pm .07$
	3	$-0.552 \pm .005$	$-1.71 \pm .07$
	4	$+0.589 \pm .006$	$-0.50 \pm .10$
	5	$+1.422 \pm .005$	$-0.76 \pm .09$
	6	$+1.016 \pm .007$	$+1.37 \pm .08$
	7	$-0.934 \pm .005$	$+2.46 \pm .08$
	8	$-2.418 \pm .006$	$+1.27 \pm .09$

Table 2.3: Results from translational alignment using cosmic muon data.

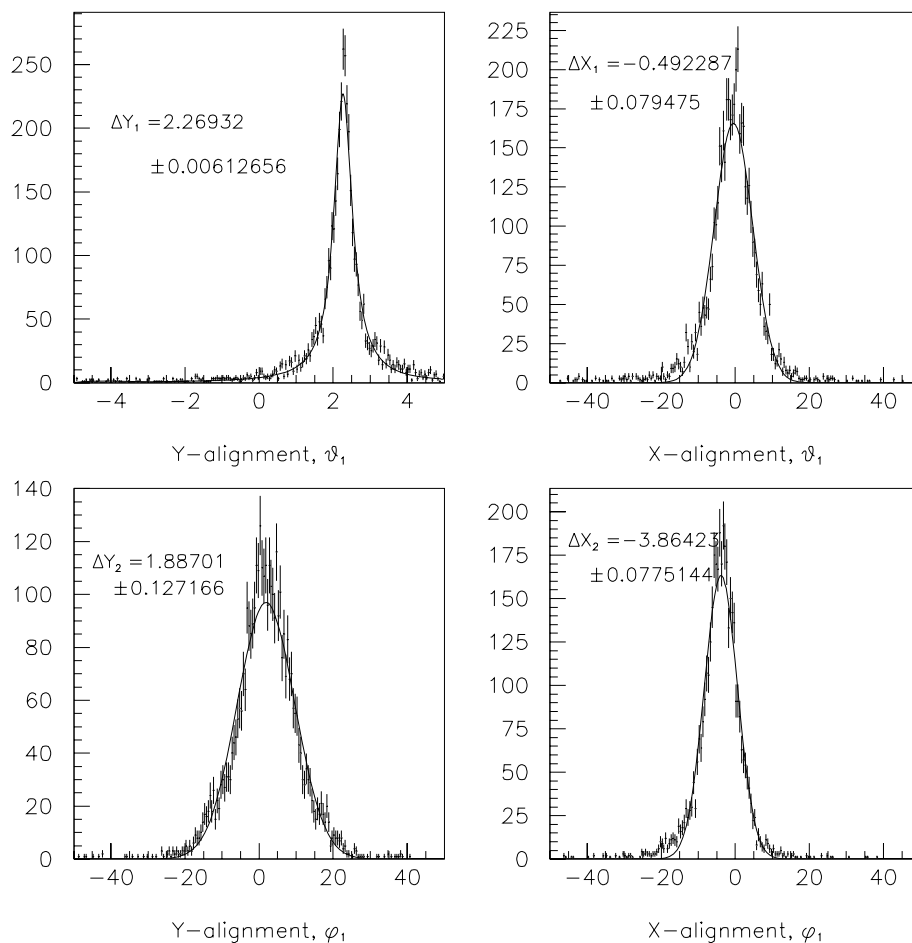


Figure 2.12: Examples of the checksums used in the alignment procedure. The upper two plots show the x and y translational alignment for θ_1 , and the lower two are the equivalent plots for ϕ_1 . The scale along the x axis is in cm.

θ_3 were assumed to be zero. The alignment procedure described in section 2.6.2 was then performed on the misaligned data, and the resulting values obtained compared with those used to misalign the system.

The results are shown in figure 2.14, and it can be seen that the calculated values for the misalignment quantities have approximately the same values as those used to misalign the system (the fact that the sign is reversed is to be expected). The alignment in the drift coordinate (y in the θ layers and x in the ϕ layers) is more effective than the alignment in the charge division coordinate, due to its higher resolution. The dashed line on each of the plots shows a line of gradient -1, *ie.* where the points are expected to lie, rather than a fit to the points.

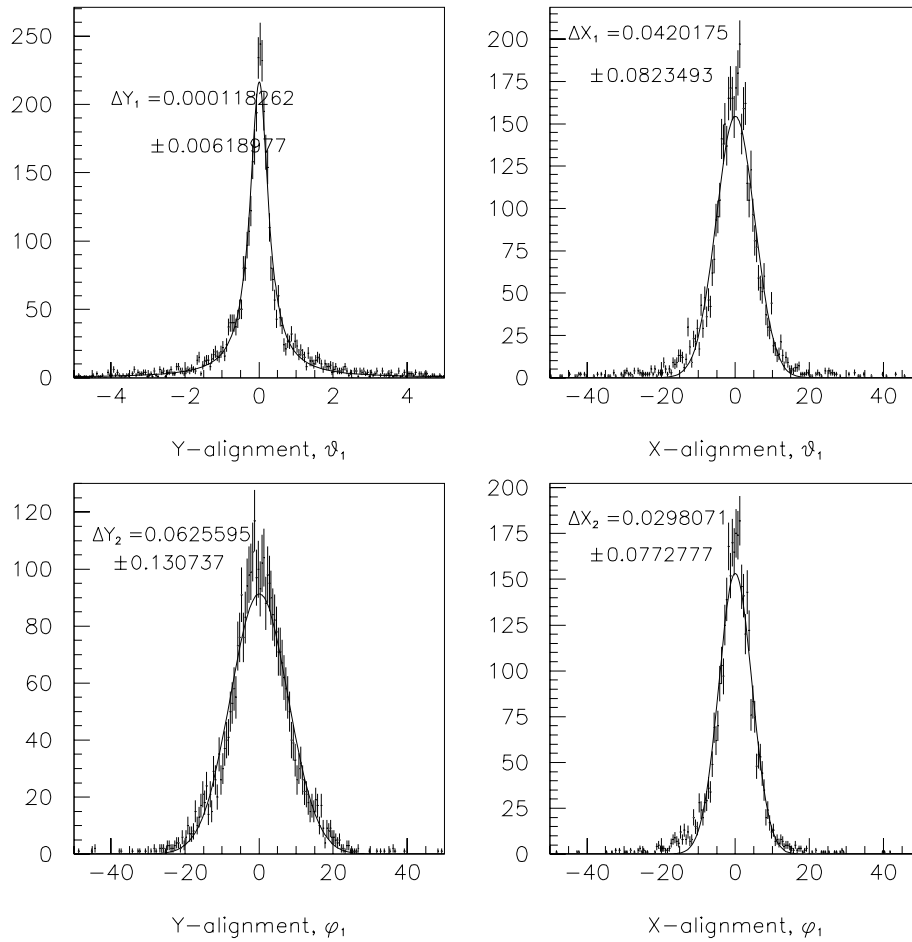


Figure 2.13: *Examples of the checksums used in the alignment procedure. The upper two plots show the x and y translational alignment for θ_1 , and the lower two are the equivalent plots for ϕ_1 . The scale along the x axis is in cm .*

2.6.5 The effect of misalignment on momentum resolution

A second study was performed using simulated data to test the effect of misalignments on the momentum measurement made by the FMD. In the study, a sample of 30000 simulated single muon tracks were used, but in this case, the toroid was on. The muons had momentum ranging between 2 and 50 GeV, and an angular range of $4^\circ < \theta < 18^\circ$.

The simulated data was reconstructed under three different conditions of alignment, to give three MC data samples:-

- Perfectly aligned layers.

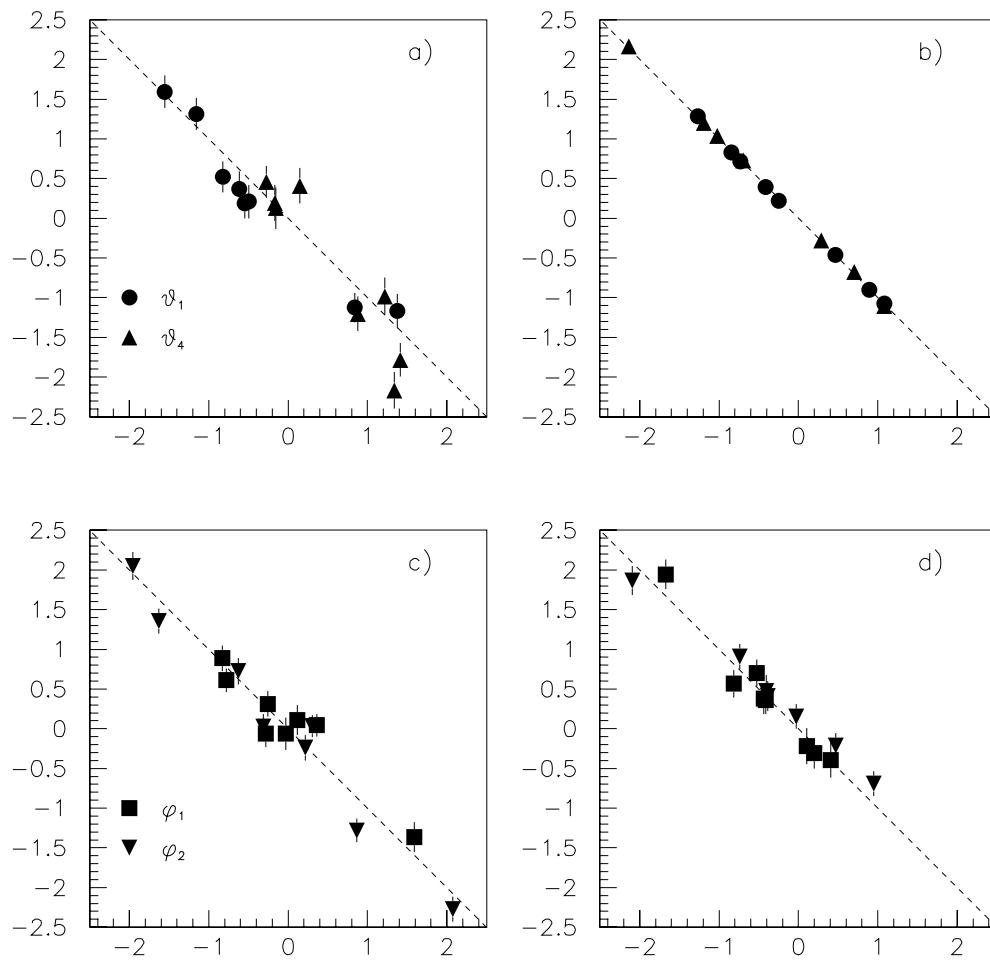


Figure 2.14: A comparison of the misalignment values found using the checksum method, with those used to misalign the system. Plot a) shows the x alignment for the θ layers, b) the y alignment for the θ layers, and c) and d) are the corresponding plots for the ϕ layers. The dashed line on each plot is of gradient -1.

- Translational misalignments in all layers.
- Re-alignment in layers $\theta_1, \theta_2, \phi_1, \phi_2$.

The misalignment of the FMD is not included in the simulation, hence the first sample was obtained by simply reconstructing the data without introducing any misalignments. The second data sample was obtained by including random translational misalignments in the reconstruction stage, as described in section 2.6.4. In this case however, all six layers were effectively misaligned, including layers θ_2 and θ_3 . In order to obtain the third sample, the translational misalignments in x and y were first calculated using the checksum method for layers $\theta_1, \theta_4, \phi_1$, and ϕ_2 , using the sample of toroid-off simulated cosmic muons (section 2.6.4). The reconstruction was then carried out taking account of both the misalignment and re-alignment values.

The inverse momentum resolution was measured from the width of the distribution:

$$\frac{\sigma_{1/p_{rec}}}{1/p} = \frac{1/p_{rec} - 1/p_{gen}}{1/p_{gen}} \quad (2.14)$$

where p_{rec} is the reconstructed momentum, and p_{gen} is the generated momentum. The inverse momentum is plotted, rather than the momentum, because it gives a more Gaussian distribution [17]. The inverse momentum resolution was measured in eight momentum bins between 2 and 50 GeV, for the three different samples of MC data.

Examples of resolution plots are shown in figure 2.15. These plots are for values of momentum between 14 and 20 GeV. Figure 2.16 shows the resolution in $1/p$ as a function of the momentum, p , for all three samples of MC data, and shows the alignment procedure improves the resolution dramatically. In the misaligned sample the correlation between generated and reconstructed momenta was very poor above approximately 20 GeV. For the re-aligned sample, the alignment procedure was carried out with the assumption that layers θ_2 and θ_3 were perfectly aligned, although random misalignment values were included for both these layers. Figure 2.16 justifies the claim that this assumption should not affect the momentum measurement.

2.7 Summary

Monitoring of the calibration constants, T_0 and the drift velocity, was performed over the 1994 and 1995 running periods. The results of these studies were implemented in the database at the end of each running period, so that the data might then be reconstructed with the best possible calibration. Similarly, the results for the alignment measurements

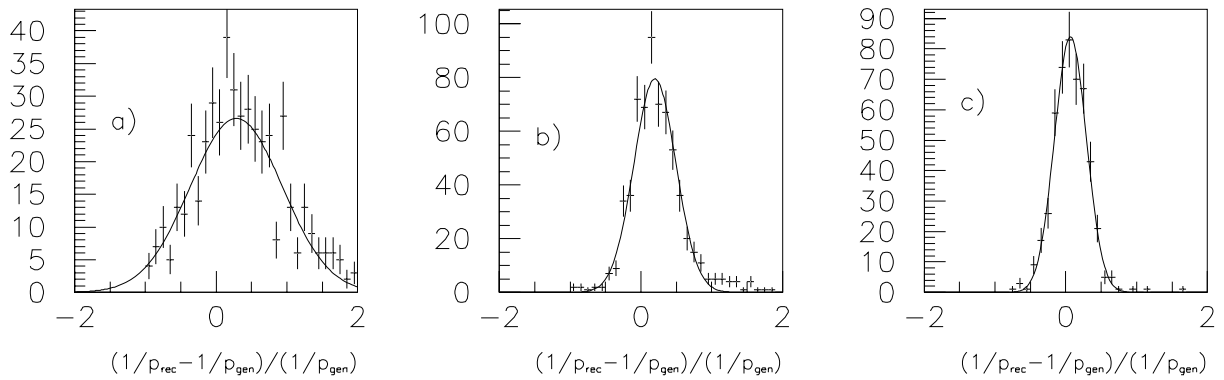


Figure 2.15: Plot a) shows the resolution in $1/p$ for a totally misaligned system, b) for the aligned system, and c) for a perfectly aligned system.

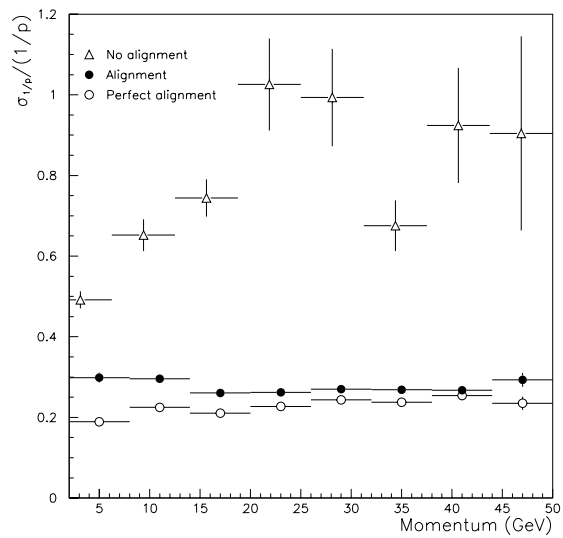


Figure 2.16: Inverse momentum resolution vs. momentum for a misaligned, aligned and perfectly aligned system.

were also implemented in the database. The studies of the change in drift velocity with voltage indicated that the drift chambers of the FMD are operating near the plateau of the drift velocity curve, and this is further demonstrated by the stability of the drift velocity over both years (see figures 2.9 and 2.10).

The implementation of both rotational and translational alignment values in the reconstruction clearly improves the momentum resolution immensely (see figure 2.16). The ability of the FMD not only to identify muons but to provide an independent momentum measurement is important in physics analysis involving muons in the forward direction, and without any alignment this would be virtually impossible. The problems with synchrotron radiation in 1994 meant that little useful data was taken by the FMD in that year, but during the 1995 running period, 2868 nb^{-1} of data was taken whilst both the FMD and the forward muon trigger were both fully operational. Analysis is currently underway measuring the cross section for elastic J/ψ production where both the muons from the J/ψ decay lie in the FMD [18]. The signal for J/ψ production in the forward direction is shown in figures 2.17 and 2.18. This measurement is of interest as it yields a cross section at a γp centre of mass energy (W) comparable to previous fixed target experiments, and allows the cross section dependence on W to be studied over a wide range in W using only H1 data (see section 3.4.4).

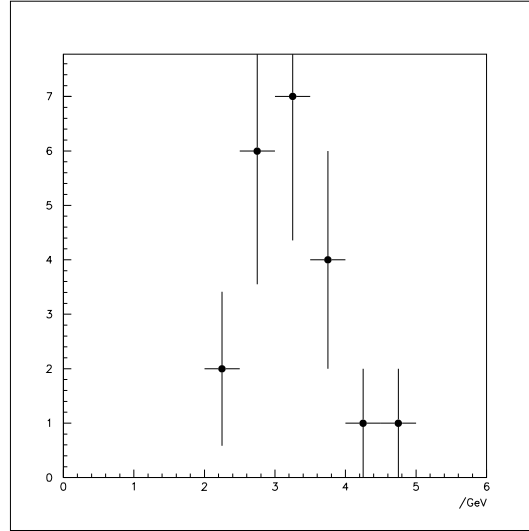


Figure 2.17: *Invariant mass spectrum for candidate $J/\psi \rightarrow \mu^+\mu^-$ events where both muons are detected in both the forward tracker and in the FMD. The invariant mass is formed using the momentum measurement from the FMD.*

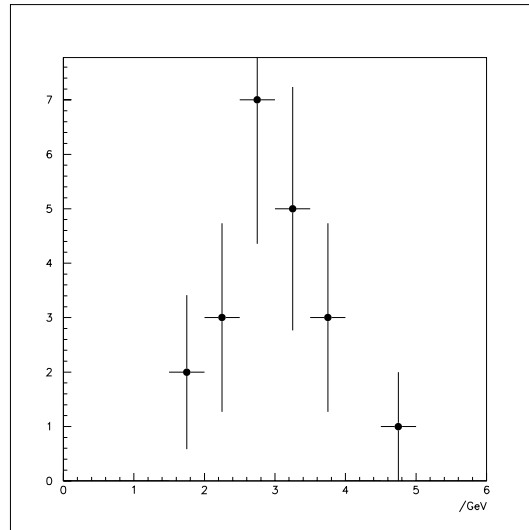


Figure 2.18: *Invariant mass spectrum for candidate $J/\psi \rightarrow \mu^+\mu^-$ events where both muons are in the forward direction. The invariant mass is formed using the momentum measurement from the Forward Tracker.*

Chapter 3

HERA Physics

3.1 Introduction

The high centre of mass energies available at HERA extend the accessible kinematic regions in ep scattering by two orders of magnitude compared to previous measurements. Deep inelastic scattering (DIS) events are characterised by the variables x and Q^2 , where x is the fraction of the proton's momentum carried by the struck quark and Q^2 is the negative four momentum transfer squared between the incoming and outgoing leptons. At HERA, DIS events can be measured down to x values of 10^{-5} , extending our knowledge of the internal structure of the proton, and Q^2 values of up to $\sim 10^5 \text{ GeV}^2$ may be reached. This creates an ideal testing ground for aspects of the standard model, particularly the theory of strong interactions, Quantum Chromodynamics (QCD). Events with $Q^2 \sim 0$ are known as photoproduction events, and the study of these allows the nature of the photon to be probed at previously inaccessible energies. Both DIS and photoproduction are discussed in greater detail below. The production of heavy quarks at HERA also forms an extensive area of study. Thus far this has been limited to the study of 'open charm' and $c\bar{c}$ bound states, although greater luminosity should provide the opportunity to explore the field of beauty production. The various mechanisms for the production of charm at HERA are discussed in the final section of this chapter.

3.2 Deep Inelastic Scattering

The deep inelastic scattering process $ep \rightarrow e(\nu)X$ can be considered in two stages. Firstly, there is an elastic scattering between the electron and a quark inside the proton. Secondly, hadronisation of the struck quark and proton remnant occurs, with colour

equalisation between the current and remnant jets. This process is a consequence of colour confinement; the struck quark is coloured and cannot be observed in isolation, implying strong inter-parton forces between the struck quark and the proton remnant. DIS cross sections depend on the elastic electron quark scattering amplitude and on the quark distributions within the proton, which are expressed as structure functions.

3.2.1 Kinematics

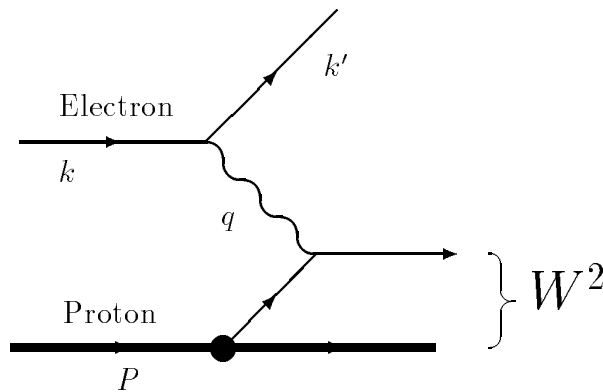


Figure 3.1: Diagram showing four vectors used to describe the kinematics of electron - proton scattering.

The four-vectors used to describe the kinematics of the DIS process are shown in figure 3.1. The process can be described by two independent Lorentz scalars, conventionally chosen to be Q^2 and x . In Lorentz invariant notation, these variables are given by

$$Q^2 = -q^2 = -(k - k')^2, \quad (3.1)$$

$$x = \frac{Q^2}{2P \cdot q}. \quad (3.2)$$

In the Quark Parton Model (QPM) [19][20], x is the fraction of the proton momentum carried by the struck parton (Bjorken x). A further Bjorken scaling variable, y , is the fraction of energy transferred to the hadronic system from the incoming electron, in the rest frame of the proton.

$$y = \frac{P \cdot q}{P \cdot k}, \quad (3.3)$$

where k , k' and P are the four-momenta of the incoming lepton, outgoing lepton, and the incoming proton respectively, and q is the four-momentum of the virtual exchange particle. Neglecting the masses of the electron and proton, these quantities are related by the equation

$$Q^2 \simeq xys, \quad (3.4)$$

where s is the centre of mass energy squared, defined as

$$s = (k + P)^2 \simeq 4EE_P. \quad (3.5)$$

E and E_P are the energies of the incoming electron and proton respectively. Again neglecting the proton mass, the invariant mass squared, W^2 , of the hadronic final state is given by

$$W^2 = (q + P)^2 = Q^2 \frac{1-x}{x}. \quad (3.6)$$

The two independent Lorentz scalars can in turn be reconstructed from two independent experimental variables. The fact that at H1 both the scattered electron and the hadronic final state are measured means that the kinematics may be determined from the measured electron variables, the measured hadronic variables or a mixture of both. The experimental quantities usually measured in lepton - nucleon scattering are the polar angle, θ , and the energy, E' , of the scattered lepton. The kinematic variables x , y and Q^2 are then given by

$$Q^2 = 4EE' \cos^2 \left(\frac{\theta}{2} \right), \quad (3.7)$$

$$y = 1 - \frac{E'}{E} \sin^2 \left(\frac{\theta}{2} \right), \quad (3.8)$$

$$x = \frac{Q^2}{sy}. \quad (3.9)$$

For the neutral current process $ep \rightarrow eX$ the exchange particle is either a virtual photon or Z^0 , although Z^0 exchange is suppressed by a factor

$$\sim \left(\frac{Q^2}{Q^2 + M_Z^2} \right)^2$$

with respect to γ exchange. Similarly the charged current process $ep \rightarrow \nu X$, where the exchange particle is W^\pm , is suppressed until Q^2 is of the order of M_W^2 . For most of the accessible kinematic region at HERA, Z^0 and W^\pm do not contribute significantly.

3.2.2 The Proton Structure Function

The total neutral current DIS cross section may be expressed as the 'Born' cross section with corrections for initial and final state electromagnetic radiation. The Born cross sections may be expressed in terms of three structure functions, $F_1(x, Q^2)$, $F_2(x, Q^2)$ and $F_3(x, Q^2)$, which describe the quark structure of the proton.

$$\frac{d^2\sigma_{NC}}{dx dQ^2} = \frac{4\pi\alpha_{em}^2}{xQ^4} \left[y^2 x F_1(x, Q^2) + (1-y) F_2(x, Q^2) \pm \left(y - \frac{y^2}{2} \right) x F_3(x, Q^2) \right] \quad (3.10)$$

The parity violating term involving $F_3(x, Q^2)$ relates to Z^0 exchange and is therefore negligible for $Q^2 \ll M_Z^2$.

In the low y region, the structure functions $F_1(x, Q^2)$ and $F_2(x, Q^2)$ are related by the Callan-Gross relation [21]

$$F_2 = 2xF_1, \quad (3.11)$$

which is a consequence of the spin half nature of the quarks. The differential cross section is then given by

$$\frac{d^2\sigma_{NC}}{dx dQ^2} = \frac{4\pi\alpha_{em}^2}{xQ^4} \left(1 - y + \frac{y^2}{2}\right) F_2(x, Q^2). \quad (3.12)$$

In the Quark Parton Model [19][20], the proton consists of non-interacting point-like particles, and a consequence of this is the ‘scaling’ of $F_2(x, Q^2)$ with Q^2 , *ie.* it is a function of the dimensionless variable x only, and is therefore independent of Q^2 at fixed x . Early ep scattering experiments at SLAC [1] observed such *scale invariance*, and this was interpreted as evidence for the existence of point-like particles inside the proton. However, scaling only holds absolutely for values of x around 0.1, and as x moves further away from this value, a slow evolution of the structure function with Q^2 is observed, an effect known as ‘scaling violation’. The evolution of the structure function with Q^2 is a consequence of the fact that the partons are not quite free, but may interact with one another. The inter-parton forces are described within QCD, the gauge theory of strong interactions, where quarks interact with each other via gluon exchange. Within QCD, the proton is pictured as three interacting valence quarks which radiate gluons, which in turn may form $q\bar{q}$ pairs, so that there is a distribution of ‘sea’ quarks within the proton in addition to the three valence quarks. At low Q^2 , the strong coupling constant, α_s , is very large, so that the quarks are very strongly interacting, a property known as ‘infra-red slavery’. However, α_s falls rapidly with increasing Q^2 , so that at high Q^2 the quarks may be considered as non-interacting. The behaviour of the quarks in the high Q^2 limit is known as ‘asymptotic freedom’. The evolution of the structure function with Q^2 is well described by the evolution equations of Dokshitzer, Gribov, Lipatov, Alterelli and Parisi (DGLAP) [22]. Once the structure function has been measured at some fixed value of x and Q^2 , these equations may be used to evaluate F_2 as a function of x and Q^2 .

The structure function $F_2(x, Q^2)$ has been measured at H1 over a wide range of x and Q^2 and is shown in figures 3.2 and 3.3. In the newly accessed low x region, it is observed to rise steeply with decreasing x at fixed Q^2 , which may be attributed to an increasing gluon density, and hence a growing sea quark density at low x [23]. Figures 3.2 and 3.3 are taken from [24].

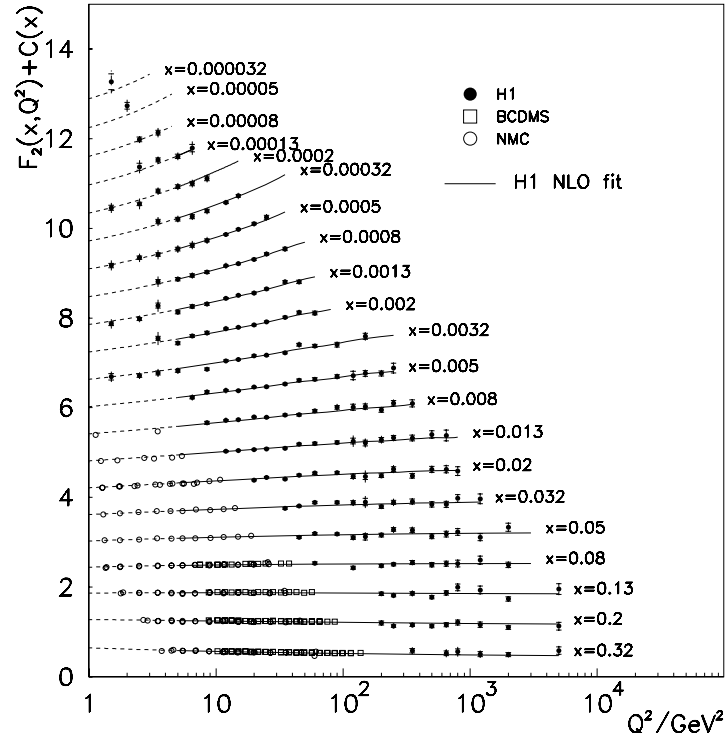


Figure 3.2: Measurement of the structure function $F_2(x, Q^2)$ as a function of Q^2 [24]. The H1 points are shown together with those from fixed target experiments BCDMS[25] and NMC[26]. The lines correspond to a NLO QCD fit. F_2 values are plotted on a linear scale, adding a constant, $C(x) = 0.6(i - 0.4)$, where i is the bin number and $i = 1$ for $x = 0.32$.

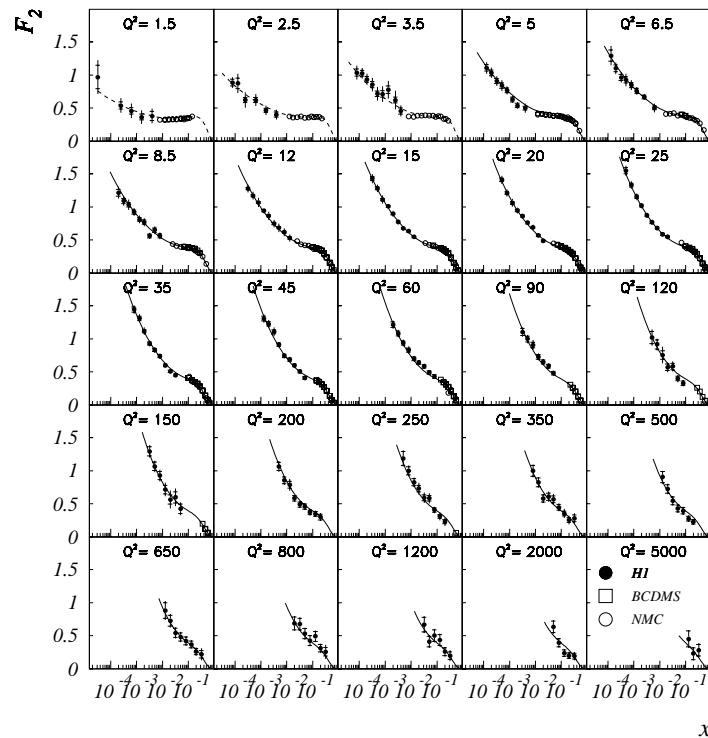


Figure 3.3: Measurement of the structure function $F_2(x, Q^2)$ as a function of x [24].

3.3 Photoproduction

The dominant process at HERA is ‘photoproduction’, in which the electron is scattered through very small angles and $Q^2 \sim 0$. These events can be viewed in terms of an interaction between the proton and a quasi-real photon. The rate is large because the amplitude for $e \rightarrow e\gamma$ diverges as $Q^2 \rightarrow 0$.

The cross section (σ_{ep}) obtained from ep interactions in H1 at $Q^2 \sim 0$ may be factorised into a photon flux multiplied by a photoproduction cross section ($\sigma_{\gamma p}$). The photon flux is the probability for a photon being emitted at the electron vertex and is given by the Weizsäcker Williams approximation (see section 5.4.2). At HERA photoproduction cross sections are measured at γp centre of mass energies an order of magnitude larger than in previous fixed target experiments. At $Q^2 \sim 0$, the centre of mass energy of the photon proton system, $W_{\gamma p}$, is given by

$$W_{\gamma p} \simeq 2\sqrt{E_\gamma E_p}. \quad (3.13)$$

3.3.1 Elastic scattering and Regge Models

In models based on Regge Theory [27], the scattering process is mediated by a virtual meson (a *reggeon*) or by a colourless object with the quantum numbers of a vacuum (the *pomeron*). Processes which fall into the latter category are described as *diffractive*. The exchange particles are described by *Regge trajectories*, linear paths in spin-mass squared space. Physically observed real resonances occur at integer values of spin in the s -channel ($M^2 > 0$). Exchanged virtual mesons have negative M^2 ($= t$) and in Regge theory their spin is complex and varies continuously with t . Regge trajectories are found to be linear, so they are usually parameterised in the form

$$\alpha(t) = \alpha(0) + \alpha' t, \quad (3.14)$$

where $W = W_{\gamma p}$, the centre-of-mass energy in the photon-proton system. Since the pomeron intercept, $\alpha_P(0)$, is much larger than that of mesons, elastic processes, *eg.* exclusive vector meson production, are mediated at HERA energies by the exchange of a pomeron, and the differential cross section at fixed t may be expressed in this model as

$$\frac{d\sigma}{dt} \propto \left(\frac{W^2}{W_0^2} \right)^{2\alpha_P(t)-2}. \quad (3.15)$$

The variation of the cross sections with t at fixed energy W has been found to be well described by an exponential parameterisation, and the general form of the cross section

is therefore given by

$$\frac{d\sigma}{dt} \propto \left(\frac{W^2}{W_0^2}\right)^{2\alpha_{\mathbb{P}}(0)-2} e^{bt}, \quad (3.16)$$

where the factor $(W^2/W_0^2)^{2\alpha'_{\mathbb{P}}t}$ is absorbed into e^{bt} . This model has been enormously successful in describing the elastic photoproduction of the light vector mesons, ρ , ω , ϕ , as well as elastic hadron-hadron cross sections. The energy dependence of the cross section is related to the intercept of the pomeron trajectory, $\alpha_{\mathbb{P}}(0)$, hence measurements of the W dependence of the cross sections for elastic processes give information on the nature of the exchange particle. Regge theory predicts that the parameter describing the t dependence of the differential cross section, the b -slope, should increase with energy, giving a sharper t -distribution. This phenomenon is described as *shrinkage*. For the elastic scattering process, $AB \rightarrow AB$, mediated by the exchange of a pomeron, the slope parameter, b , is predicted to be

$$b = 2b_A + 2b_B + 2\alpha'_{\mathbb{P}} \ln \left(\frac{W}{W_0}\right)^2, \quad (3.17)$$

where b_A and b_B are the slopes of the elastic form factors for particles A and B , and scale like the square of the radii.

Regge models may also be used to describe the behaviour of total cross sections. The total cross section may be related to the imaginary part of the forward ($t = 0$) scattering amplitude of the elastic process using the optical theorem, and can be described by the general form

$$\sigma_{tot}(s) = A_{\mathbb{P}} s^{\alpha_{\mathbb{P}}(0)-1} + A_{\mathbb{R}} s^{\alpha_{\mathbb{R}}(0)-1}. \quad (3.18)$$

Equation 3.18 was used by Donnachie and Landshoff to give a good fit to $p\bar{p}$, πp and γp data [28] with single values for $\alpha_{\mathbb{P}}(0)$ and $\alpha_{\mathbb{R}}(0)$. The resulting values for the pomeron and reggeon intercepts, which are found to be universal in hadron-hadron interactions, are given by

$$\begin{aligned} \alpha_{\mathbb{P}}(0) &= 1.08, \\ \alpha_{\mathbb{R}}(0) &= 0.55. \end{aligned} \quad (3.19)$$

These constants which accurately describe a range of total cross sections also govern elastic scattering. By using this model, fits to lower energy photoproduction data give predictions for the total photoproduction cross section at HERA energies. The contribution due to reggeon exchange dominates at low centre of mass energies because of the larger coupling to hadrons of the reggeons compared to the pomeron. However, this contribution falls off as $\sim s^{-\frac{1}{2}}$, so that at higher energies, the cross section is dominated by pomeron exchange. This is demonstrated in figure 3.4 (taken from [29]) which shows the W dependence of the total photoproduction cross section. A fit to the data with the form described above

is shown in figure 3.4 as a solid line. At $W_{\gamma p} = 200$ GeV, the total photoproduction cross section measured at H1 was $165 \pm 2 \pm 11 \mu\text{b}$ [29], where the first error is statistical and the second systematic.

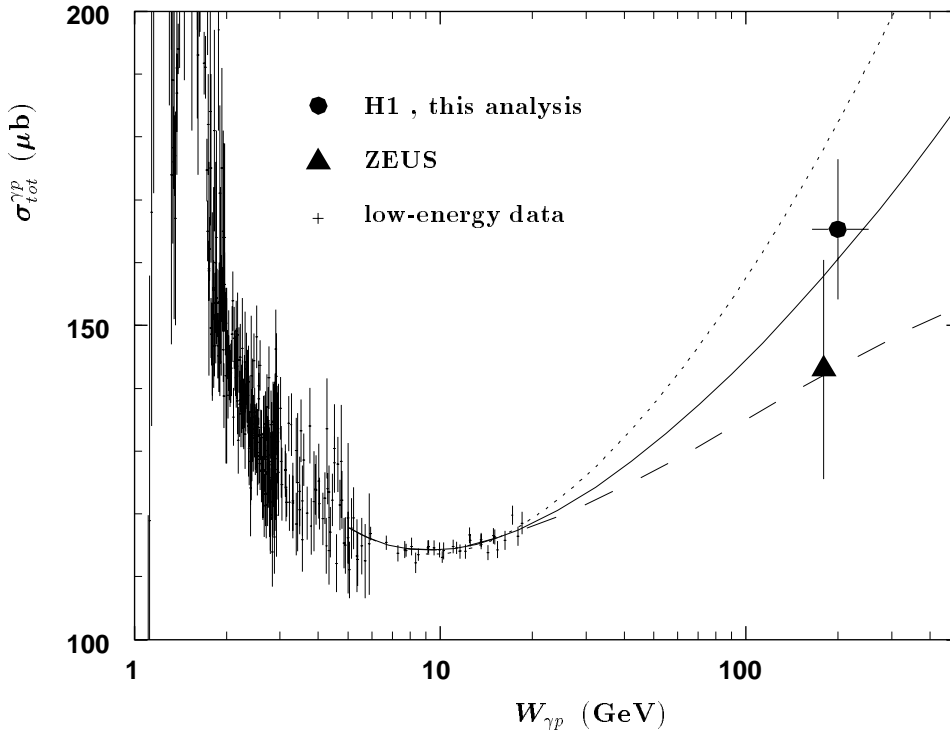


Figure 3.4: Total photoproduction cross section as a function of the γp centre of mass energy, where the HERA results from H1 and ZEUS are shown together with lower energy data. The solid line is the Donnachie Landshoff fit described above, whilst the dotted line shows the DL parameterisation including the recent high energy $p\bar{p}$ data at CDF[30]. The dashed line is the ALLM parameterisation[31].

3.3.2 The Vector Dominance Model

The largest contribution to the total photoproduction cross section arises from peripheral (soft) processes, in which the four momentum transfer squared between the photon and the proton is small, typically $|t| \ll 1 \text{ GeV}^2$. It has been observed in previous experiments that photon-hadron interactions display broadly similar characteristics to hadron-hadron interactions [32], indicating that the photon behaves hadronically, with the cross section reduced by a factor of the order of the fine structure constant. The hadronic component of the photon may be understood in terms of the QED splitting process $\gamma \rightarrow q\bar{q}$, and the subsequent development of the $q\bar{q}$ pair into the hadronic state. The photon wavefunction can be considered as a superposition of a bare photon component, $|\gamma_B\rangle$, and a hadronic

component, $|h\rangle$.

$$|\gamma\rangle = \sqrt{Z_3} |\gamma_B\rangle + c\sqrt{\alpha} |h\rangle. \quad (3.20)$$

The hadronic state must have the same quantum numbers as the photon in its bare state, *ie.* $J^{PC} = 1^{--}$, and zero charge strangeness and baryon number. In the simplest version of the Vector Dominance Model (VDM) [33], the vector meson states ρ , ω and ϕ are the sole constituents of the photon, *ie.* $|h\rangle$ is described as a superposition of these states.

$$\sqrt{\alpha} |h\rangle = \sum_V \frac{e}{f_V} \frac{m_V^2}{(m_V^2 + Q^2)} |V\rangle, \quad (3.21)$$

where m_V is the mass of the vector meson, V , and the sum is made over the states ρ , ω and ϕ . In this model, the bare component, $|\gamma_B\rangle$, does not interact with hadrons. The VDM can be used to relate photoproduction processes, $\gamma p \rightarrow X$ to the vector meson scattering process $V p \rightarrow X$, using the coupling of the vector meson to the photon. This idea is discussed further in section 3.4.4. The ideas of vector dominance were generalised[34] to include the higher mass vector mesons (ρ' , J/ψ , ψ' , Υ). An extended version of the VDM[35] also includes a spectrum of unbound states with the correct quantum numbers (*eg.* $\pi^+\pi^-$, $\pi^+\pi^-\pi^0$, $K\bar{K}\dots$).

3.3.3 Hard Scattering in Photoproduction

Although the photoproduction processes are predominantly ‘soft’, the observation of the occasional production of high p_T particles and jets in the final state indicates a hard component to the total cross section. These hard scattering processes give rise to outgoing partons with p_T of 1 GeV or more, and fall into one of two categories: direct and resolved processes. Examples of direct processes are photon gluon fusion and QCD Compton events. In both of these cases the photon couples in a point-like manner to a parton from the proton. Photon gluon fusion events are of particular interest as the major source of heavy flavour production at HERA, and this will be discussed further in section 3.4.

Events in which the photon couples through its hadronic structure are known as resolved process. Resolved processes include a component due to the VDM contribution, where the relative p_T^2 of the $\gamma \rightarrow q\bar{q}$ process is small, leading to the formation of a bound state. There is an additional ‘anomalous’ component where the $\gamma \rightarrow q\bar{q}$ process occurs with high relative transverse momentum. The p_T then provides a hard scale which ensures $\alpha_s(p_T^2)$ is small and subsequent QCD development is limited. Examples of direct and resolved hard γp process are shown in figure 3.5.

The hadronic nature of the photon may be expressed in terms of parton distribution functions within the photon. A photon structure function, F_2^γ may be defined, in analogy

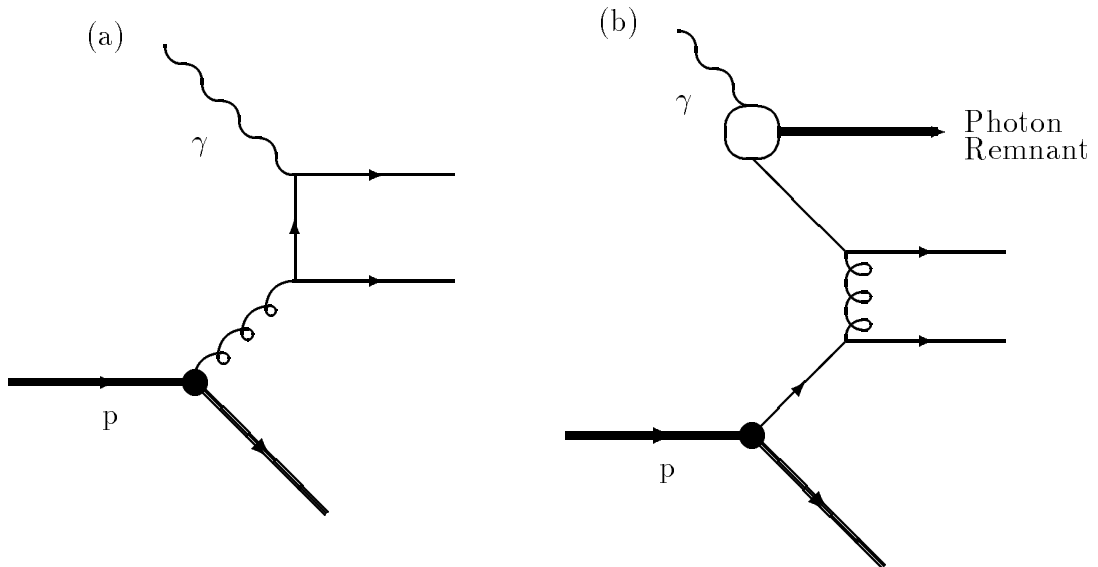


Figure 3.5: *Examples of hard photoproduction processes at HERA. Diagram (a) shows the direct process, photon-gluon fusion, and diagram (b) shows the resolved process.*

to the proton structure function, which describes the quark content of the photon. This has been measured over a restricted range of x_γ , the momentum fraction of the parton from the photon, in two-photon experiments. At H1, by assuming these measured values for F_2^γ , the x_γ spectrum of two jet events can be used to extract the gluon distribution within the photon, by subtraction of the quark contribution [36]. Whereas in DIS the virtual photon is used to probe the structure of the photon, in photoproduction the partons in the proton can be used to probe the quark and gluon content in the photon. In photoproduction however, where $Q^2 \sim 0$, it is the p_T^2 of the jets which sets the hard scale that makes perturbative QCD applicable.

3.4 Heavy Flavour Production

The production of heavy flavours in positron-proton collisions at HERA provides an important area of study. At HERA, charm is produced in $c\bar{c}$ pairs, giving rise to both open charm states, such as D^* and D^0 , and the ‘hidden charm’ ($c\bar{c}$ bound) states, such as J/ψ and ψ' ¹. The cross section for the production of $b\bar{b}$ pairs is significantly smaller than that for $c\bar{c}$ production (by a factor of ~ 400 [37]) and they have yet to be observed at H1. Charmed pair production occurring via inelastic collisions, where colour is transferred between the $c\bar{c}$ pair produced and the proton remnant, gives rise to both open charm and

¹The notation ψ' is used throughout this thesis to refer to the state labelled $\psi(2S)$ in [64].

bound states, and involves predominantly photon gluon fusion. The bound vector meson states, J/ψ and ψ' , may be produced in ‘diffractive’ collisions. In this case, the interaction may be ‘elastic’, in which case the proton stays intact, or the proton may dissociate. This section will examine the various charm production mechanisms, focusing in more detail on the production of the vector meson states, J/ψ and ψ' . A brief discussion on the ratio of the cross sections for the production of J/ψ and ψ' will conclude the chapter.

3.4.1 Open Charm

The production of charmed mesons at HERA occurs in both DIS and photoproduction. The cross section for charm photoproduction is almost an order of magnitude larger than that for the production of charm in DIS, but the dominant mechanism in both cases is that of photon gluon fusion. Contributions to the charm cross section from b decays are negligible due to the small b production cross section.

Measurements have been made at H1 of the charm contribution to the proton structure function, $F_2^{c\bar{c}}(x, Q^2)$, using the D^* and D^0 mesons produced in deep inelastic scattering. If the results from H1 are compared with those from EMC [39], a fixed target experiment at lower energy, then a steep rise of $F_2^{c\bar{c}}(x, Q^2)$ is observed with decreasing x , as shown in figure 3.6. This rise is consistent with the rise in the gluon distribution at low x , an indication that the principal production mechanism is photon gluon fusion. The overall charm contribution to the structure function was measured over the kinematic region $8 \times 10^{-4} < x < 8 \times 10^{-3}$ and $10 < Q^2 < 100 \text{ GeV}^2$ as [38]

$$\frac{F_2^{c\bar{c}}}{F_2} = 0.237 \pm 0.021 \pm 0.041. \quad (3.22)$$

The total charm photoproduction cross section, also dominated by photon gluon fusion, may be determined from the D^* photoproduction cross section using the fragmentation fraction $B_{c \rightarrow D^*} = 0.26$ [40], the charm quark fragmentation probability into a D^* meson. The charm photoproduction cross section may be factorised into the parton level photon gluon fusion cross section (calculable in perturbative QCD) and the gluon density in the proton, $x_g g(x_g, \mu^2)$.

$$\sigma(\gamma p \rightarrow c\bar{c}X) = \int dx_g x_g g(x_g, \mu^2) \cdot \sigma(\gamma g \rightarrow c\bar{c}), \quad (3.23)$$

where x_g is the momentum fraction of the proton carried by the gluon, and μ is the factorisation scale. (Usually μ is taken to be the mass of the charm quark.) Thus the charm photoproduction cross section provides the possibility of probing the gluon density

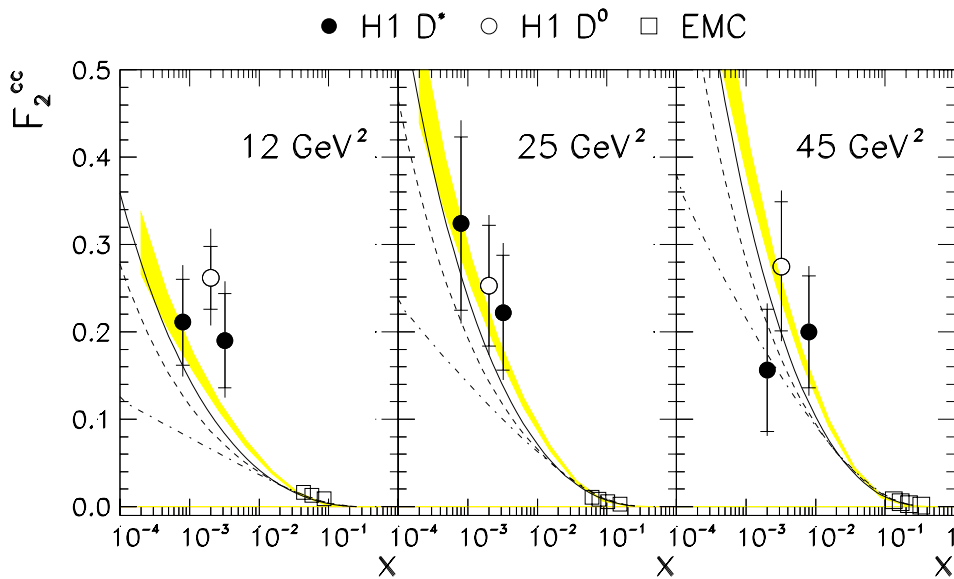


Figure 3.6: The charm contribution, $F_2^{c\bar{c}}$ to the proton structure function, compared to NLO calculations based on GRV-HO (full line), MRSH (dashed line) and MRSD0' (dashed-dotted line) parton distributions using a charm quark mass of 1.5 GeV. The shaded bands represent the prediction from the NLO fit to the F_2 measurements.

of the proton. Charm photoproduction may also occur via resolved processes, *ie.* where a parton from the photon interacts with a parton from the proton producing a $c\bar{c}$ pair (*eg.* $gg \rightarrow c\bar{c}$). This type of process dominates light quark production, but is only a small component of the production cross section for charmed quark pairs. The total charm photoproduction cross section at H1 [41] shows a sharp rise with $W_{\gamma p}$ compared to previous fixed target experiments. This is shown in figure 3.7.

3.4.2 Charmonium

The first charmonium state was discovered in November 1974 at Brookhaven [44] as a narrow resonance at ~ 3.1 GeV in the invariant mass spectrum of e^+e^- pairs from the reaction $p+Be \rightarrow e^+e^-X$. At the same time, a resonance was observed (also at ~ 3.1 GeV) at the e^+e^- storage ring, SPEAR, at SLAC [45], where a second resonance was discovered two weeks later at a mass of ~ 3.7 GeV [46]. These resonances, denoted the J/ψ and ψ' , were interpreted as the bound state of a new heavy quark and its antiquark in terms of a parton model. It was speculated that these heavy quarks carried a new quantum number, charm, which, like strangeness, was conserved in strong and electromagnetic interactions. The existence of the charm quark had been predicted in 1970 by Glashow, Iliopoulos and Maiani [47] to explain the non-existence of flavour changing neutral currents.

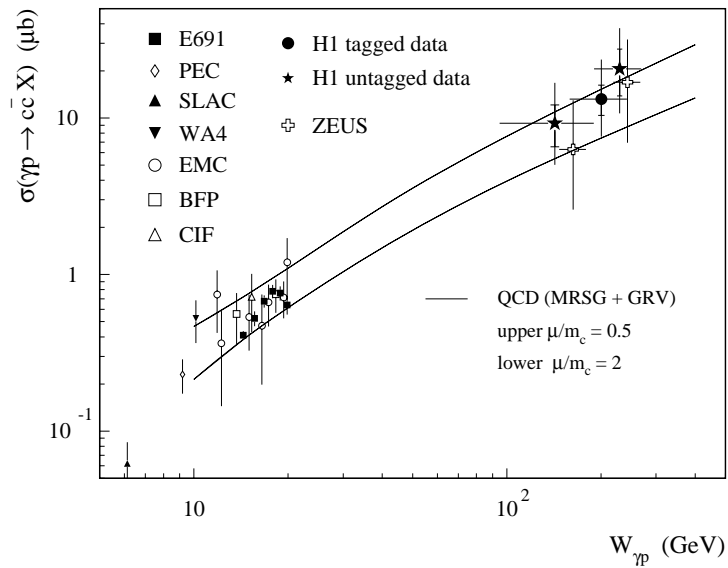


Figure 3.7: Total charm photoproduction cross section as a function of $W_{\gamma p}$. H1 points are shown together with those from ZEUS [42] as well as previous fixed target experiments [39][43]. The ‘tagged’ data refers to events where the scattered positron was detected in the electron tagger, and events where no scattered lepton is seen are referred to as ‘untagged’. The solid lines represent a NLO QCD calculation, where the upper and lower lines delimit the range of values expected by varying the renormalization scale within $0.5 < \mu/m_c < 2$.

In time a whole spectrum of $c\bar{c}$ states was uncovered, which are shown diagrammatically in figure 3.8. The spectrum of energy levels shows a remarkable similarity to that for another set of fermion-antifermion bound states, positronium, hence the term *charmonium* was given to the new particles. Positronium and charmonium spectra differ greatly in the scale of their structure. The difference in energy between the $1S$ and $2S$ levels in positronium is a few eV, whereas it is ~ 600 MeV for charmonium. This large difference, a factor of approximately 10^8 , is the result of the large mass of the charm quark compared to the electron, and the size of the strong coupling constant, α_s . Also shown in figure 3.8 is the energy threshold for the production of the lightest pair of charmed mesons (D^+D^-). The decay widths of the charmonium states below this threshold are very narrow, whilst those above are much broader, characteristic of hadronic decay. The leptonic decay widths, however, are comparable to those of other vector mesons (ρ , ω). The narrow widths below the $D\bar{D}$ threshold are attributed to the Zweig suppression of strong decay channels, whereas the higher mass states decay strongly: $\psi \rightarrow D\bar{D}$. This is demonstrated in figure 3.9. The strong decay of the J/ψ to hadrons depends on charge conjugation and colour considerations. Firstly, the J/ψ is in a colour singlet state, as are the final state hadrons, hence the state via which the J/ψ decays must also be in a colour singlet state. If the decay proceeds via gluons, this is only possible with two or more gluons. Secondly, the J/ψ

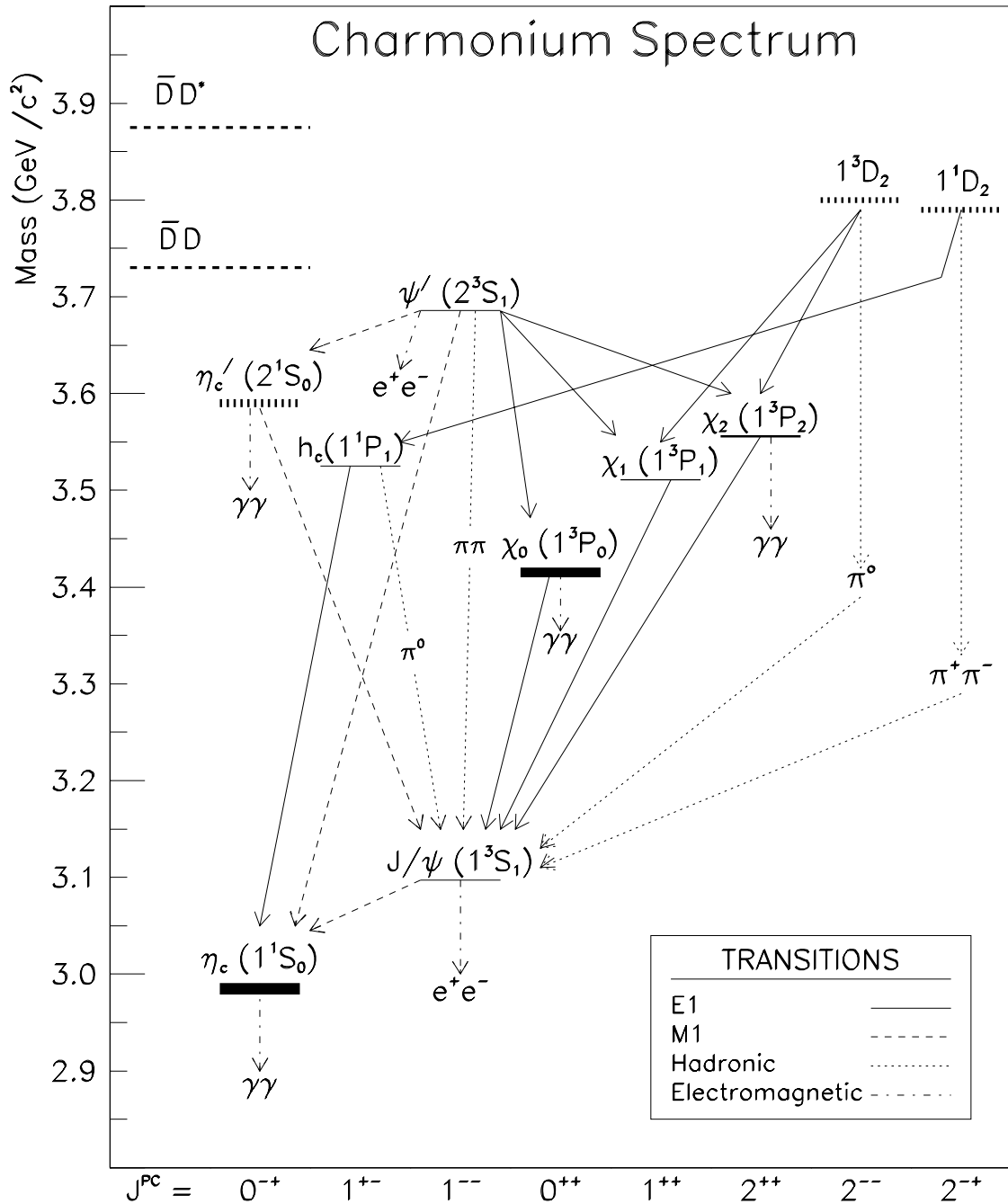


Figure 3.8: Energy levels for the charmonium system. The first observation of h_c has been reported [49], but this needs further confirmation.

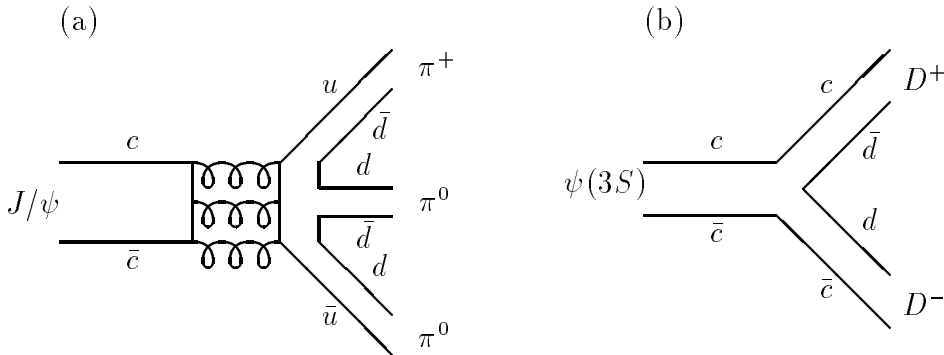


Figure 3.9: The strong decay of the J/ψ to three pions, (a), is suppressed compared to the decay of $\psi(3S)$, (b), to two charmed mesons.

has a charge parity $C = -1$, and therefore couples only to odd numbers of gluons. Thus the minimum number of gluons via which the decay may proceed is three. Alternatively, the J/ψ may decay to a light $q\bar{q}$ pair via an intermediate massive photon, although this latter mechanism accounts for only $\sim 17\%$ of the hadronic width, which is dominated by the three gluon decay.

The discovery of charmonium sparked particular interest, because of the large mass of the charm ($m_Q > \Lambda$, the QCD scale), perturbative QCD could be applied. The large scale provided by the mass implies that the bound state is of limited spatial extent and that the asymptotically free regime is approached. The charmonium spectrum may be described in terms of a non-relativistic $c\bar{c}$ potential model. In one model [48] the potential takes the form

$$V(r) = -\frac{4}{3} \frac{\alpha_s(r)}{r} + kr, \quad (3.24)$$

where the first term is a Coulomb-like potential and describes the behaviour at short $c\bar{c}$ separations, and the second term is introduced to describe quark confinement at larger distances.

3.4.3 Inelastic charmonium production

When using terms such as ‘inelastic’ and ‘elastic’ production, it is useful to define the kinematic variable z ,

$$z = \frac{p \cdot p_\psi}{p \cdot q}. \quad (3.25)$$

In the proton rest frame, this is $z = E_\psi/E_\gamma$. Inelastic events can then be defined as events with $z < 1$. The principle mechanism for inelastic ψ production is photon gluon fusion (see figure 3.10), where the photon interacts with a gluon from the proton via a charm quark, producing a $c\bar{c}$ pair, one of which then radiates a gluon, leaving a colour singlet diquark system. The production of the colour singlet $c\bar{c}$ pair in the hard interaction is

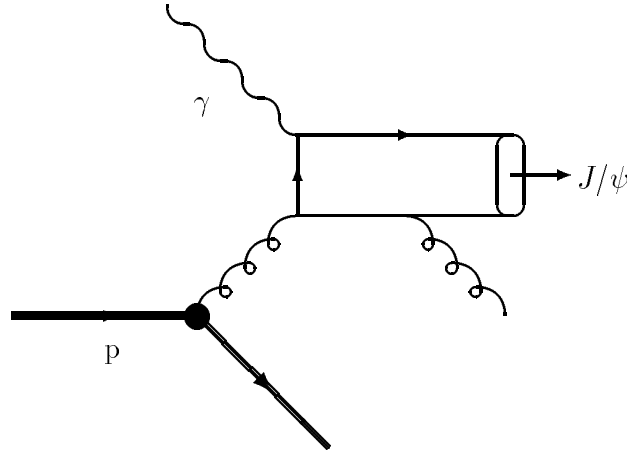


Figure 3.10: *Inelastic J/ψ production via photon gluon fusion.*

calculable in perturbative QCD within the framework of the colour singlet model [50], and is sensitive to the gluon density in the proton (equation 3.23). Once again, it is the mass of the charmed quark that gives the required hard scale that makes perturbative QCD applicable. The colour singlet model requires the $c\bar{c}$ pair to be produced with the correct spin, angular momentum and colour quantum numbers, so that their production is accompanied by the emission of a hard gluon to give the required colour singlet state (see figure 3.10). The formation of the bound J/ψ state from the colourless $c\bar{c}$ pair is a long distance non-perturbative process. The coupling of the $c\bar{c}$ to the J/ψ is dependent on the radial J/ψ wave function at the origin. The colour octet model [51], often used to describe the high production rates of J/ψ and ψ' at the Tevatron, describes the formation of the $c\bar{c}$ pair in a colour octet state as part of the hard interaction, and the subsequent transition to a colourless state proceeds non-perturbatively by the emission of soft gluons. At H1, the inelastic production of J/ψ mesons is well described by the colour singlet model, using a gluon distribution in the proton which rises toward low x_g . No evidence is observed for a colour octet contribution at H1 [52].

Resolved processes also contribute to inelastic J/ψ production, for example, gluon-gluon fusion, where a gluon from the photon interacts with a gluon from the proton producing a $c\bar{c}$ pair (see figure 3.11). These processes typically have very low values of the ‘elasticity variable’ ($z < 0.4$), and are sensitive to the gluon distribution in the photon. Gluon-gluon fusion is the principal production mechanism of charmonium in high energy hadron-hadron

collisions, but at HERA the cross section for this is small compared to that for direct processes. Resolved photon contributions to inelastic J/ψ production include

$$g + g \rightarrow J/\psi + g, \quad (3.26)$$

$$g + g \rightarrow J/\psi + \gamma. \quad (3.27)$$

The above production mechanisms contribute to the production of *prompt* J/ψ , *ie.* pro-

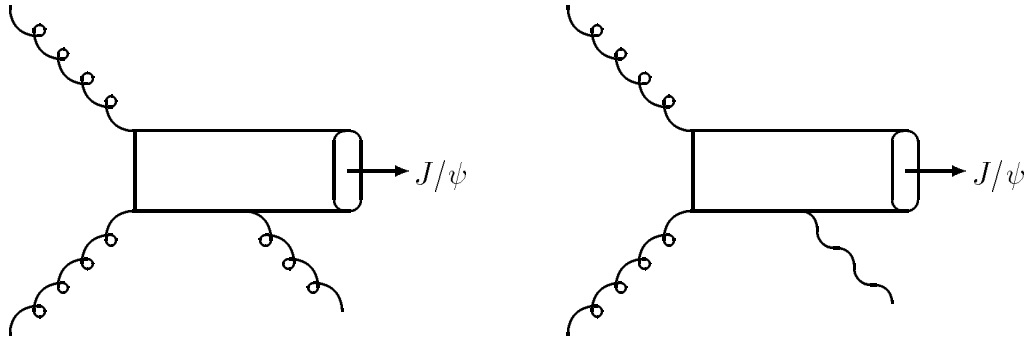


Figure 3.11: *Resolved photon contribution to inelastic J/ψ .*

cesses where the J/ψ is produced at the vertex in the hard interaction. *Indirect J/ψ* production occurs via *feed-down* from higher mass charmonium states and from the decays of b -mesons. At HERA, the latter contribution is negligible. Resolved photon processes lead to the indirect production of J/ψ via the radiative decays of the $1P$ χ states, although the cross section for this is small. In the case of positronium, two distinct states are observed; the spin singlet state para-positronium ($C = +1$) which decays to two photons, and the spin triplet state ortho-positronium ($C = -1$) which decays to three photons. The analogous states in charmonium are the 1S_1 η_c state which couples to two gluons, and the 3S_1 J/ψ , which couples to three. Hence the direct production of J/ψ via gluon-gluon fusion is accompanied by the emission of a third gluon from the resulting $c\bar{c}$ state. The $1P$ χ states, which, like η_c , have charge parity $C = +1$, couple to two gluons. Indirect J/ψ production mechanisms include

$$gg \rightarrow \chi_{0,2} \rightarrow J/\psi\gamma, \quad (3.28)$$

and the two photon process:

$$\gamma\gamma \rightarrow \chi_{0,2} \rightarrow J/\psi\gamma. \quad (3.29)$$

The production of χ_1 ($J^{PC} = 1^{++}$) is suppressed compared to $\chi_{0,2}$ ($J^{PC} = 0^{++}, 2^{++}$) as a result of the Landau-Yang theorem [53], which prohibits the production of a spin 1 particle from two gluons or two photons.

3.4.4 Diffractive ψ production

Diffractive models based on Regge theory of pomeron exchange [27] (section 3.3.1) are used to describe the ‘elastic production’ of ψ mesons² (see figure 3.12). In this model, the photon fluctuates to a virtual ψ meson which then interacts with the proton via the exchange of a colourless object. The term *elastic* is used to describe, for example, the process $\gamma p \rightarrow \psi p$, where a bound state vector meson is produced at the photon vertex, and the collision is elastic at the proton vertex. The truly elastic process $\gamma p \rightarrow \gamma p$ is $\mathcal{O}(\alpha_{em}^2)$, and therefore has a very low cross section. The term *quasi-elastic* will be used throughout this thesis to refer to both the elastic production of ψ mesons and production with proton dissociation, for events with $z > 0.95$.

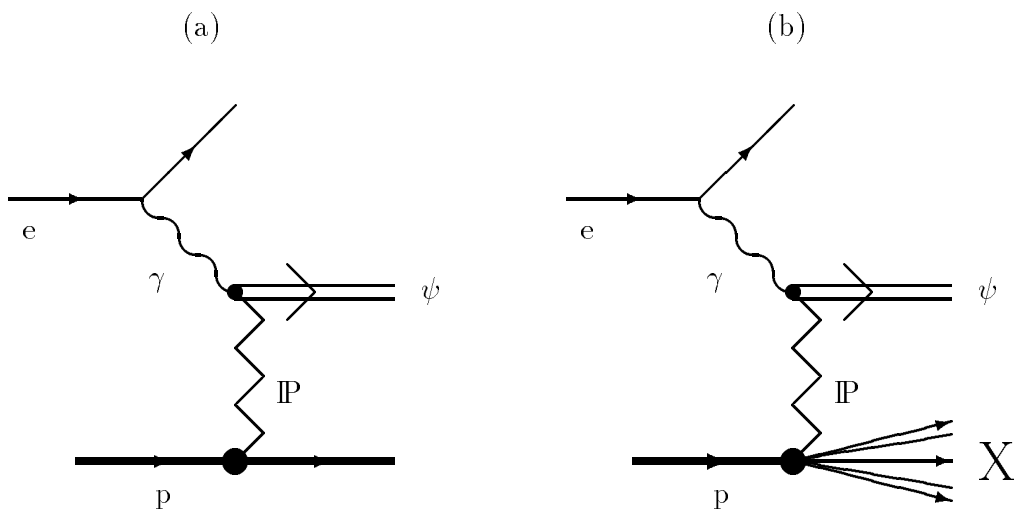


Figure 3.12: Diagram (a) shows the elastic production of a ψ' meson via the exchange of a colourless object. Diagram (b) show the case where the proton dissociates

The elastic production of ψ mesons is characterised by small values of the four-momentum transfer squared, t , and by the absence of any particles produced, other than the decay products of the ψ . The ideas of vector dominance (section 3.3.2) are used to link the process $\gamma p \rightarrow \psi p$ to the elastic scattering process $\psi p \rightarrow \psi p$, which may be described in Regge theory by the exchange of a single pomeron [28]. This model has been successfully used to describe light vector meson production (ρ , ω , ϕ ...) with a ‘soft’ pomeron, and predicts a slow variation of the elastic cross section with centre of mass energy, $W_{\gamma p}$, and an exponentially falling t distribution. The differential elastic cross section may be expressed as [54]

$$\frac{d\sigma(W, t)}{dt} = \frac{4\pi\alpha}{f_\psi^2} \frac{9}{\pi} (\beta')^2 \beta^2 (\alpha'_{IP} W^2)^{2\epsilon} e^{bt}, \quad (3.30)$$

²The use of ψ in this section denotes both the J/ψ and ψ' states.

which is equivalent to equation 3.16. The first term in the above equation is the vector dominance part, describing the coupling of the ψ meson to the photon. The terms β' and β are the couplings of the pomeron to charmed quarks (in the ψ) and light quarks (in the proton) respectively. The slope parameter, b , which describes the t distribution is given by equation 3.17, and ϵ is related to the intercept of the pomeron trajectory ($\epsilon = \alpha_P(0) - 1$). If the scattering process were mediated by the exchange of a ‘soft’ pomeron, then $\epsilon = 0.08$. However, when the results from H1 and ZEUS are compared with those from previous fixed target experiments at lower energy, the cross section for elastic J/ψ production appears to show a stronger rise with energy than expected with the soft pomeron. This is demonstrated in figure 3.13 which compares the cross section as measured at H1 at a number of values of $W_{\gamma p}$, with results from lower energy experiments. A steeper rise with centre-of-mass energy would imply the exchange of a ‘hard’ pomeron, as observed in diffractive DIS events, although in the case of J/ψ photoproduction, it is the mass of the J/ψ , rather than Q^2 , that sets the hard scale.

For photoproduction events, where $Q^2 \sim 0$, the four-momentum transfer squared, t , although not measurable directly, may be approximated by

$$t = (q - p_\psi)^2 \sim -p_T^2, \quad (3.31)$$

where p_T is the transverse momentum of the J/ψ meson with respect to the beam axis. This approximation is used to measure the b slopes for elastic photoproduction of J/ψ mesons, and for production with proton dissociation. The slopes obtained are shown in figure 3.14, which is taken from [52]. If the sample is separated into two regions in $W_{\gamma p}$, namely $30 < W_{\gamma p} < 90$ GeV and $90 < W_{\gamma p} < 150$ GeV, then the measured b -slopes for the elastic J/ψ events are $b = (3.7 \pm 0.3 \pm 0.2)$ GeV⁻² and $b = (4.5 \pm 0.4 \pm 0.3)$ GeV⁻² respectively. Within errors, there is no clear evidence for shrinkage at the present time.

Other models of elastic ψ production provide descriptions within QCD, in which the interaction between the ψ and the proton is mediated by two gluons, or a gluon ladder (figure 3.15). This approach has been adopted by Ryskin [55][56], who shows that in this model, the cross section would have a quadratic dependence on the gluon distribution in the proton, and would therefore be a sensitive probe of the gluon distribution. The energy dependence of the cross section is dependent on the low x behaviour of the gluon density of the proton in this model, hence the prediction of a faster rise of the cross section with energy, which describes the data.

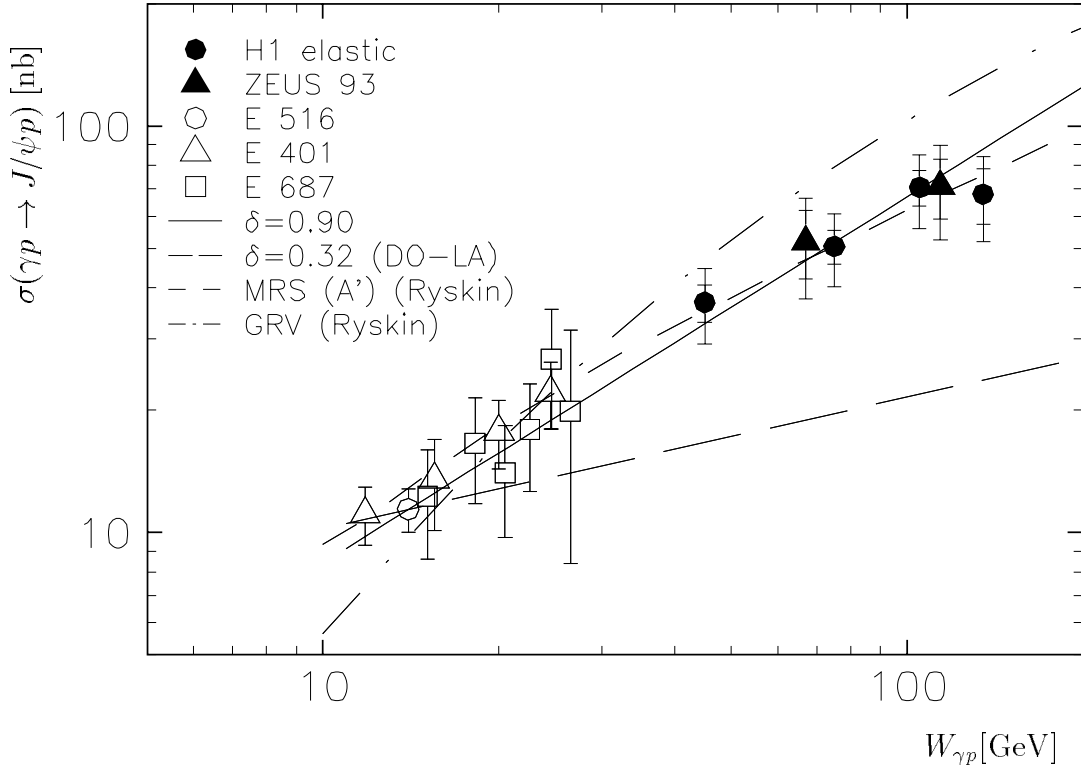


Figure 3.13: Total cross section for the elastic photoproduction of J/ψ . The H1 data [52] are shown together with data from Zeus [57] and from previous experiments at lower CMS energies [58][59][60]. The solid line shows a parameterisation of the energy dependence as $W_{\gamma p}^{\delta}$ with $\delta = 0.9$, and the long dashed line with $\delta = 0.32$, as expected for a soft pomeron. ($\delta = 4\epsilon$.) Both are normalised to the E516 point. Also include is a prediction from Ryskin, where the interaction is mediated by two gluons (or a gluon ladder).

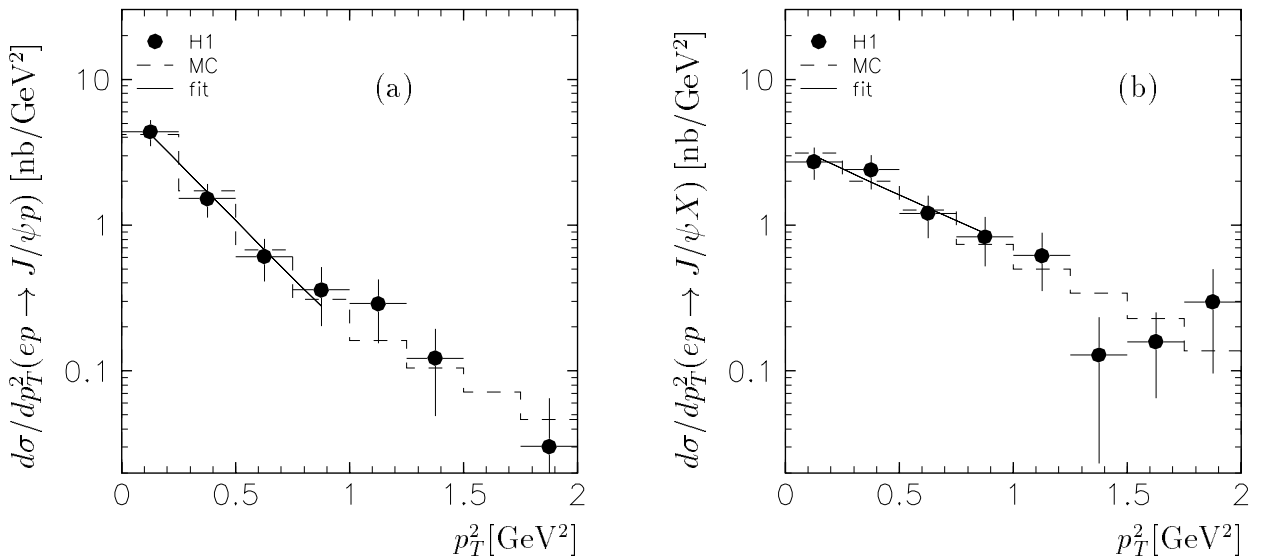
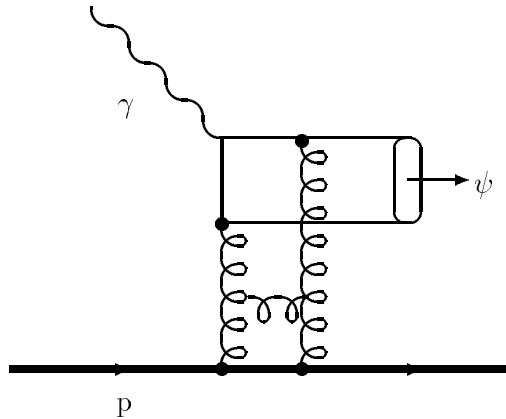


Figure 3.14: $d\sigma/dp_T^2$ for (a) elastic production of J/ψ mesons, and (b) production with proton dissociation. The data in both a) and b) are integrated over $30 < W < 150$ GeV. The points correspond to H1 data [52] and the histogram is the DIFFVM MC. The fit is of the form $\exp(-bp_t^2)$, where in a) $b = 4.0 \pm 0.3$ GeV $^{-2}$, and in (b) $b = 1.6 \pm 0.3$ GeV $^{-2}$.

Figure 3.15: *Diffractive production of ψ in the Ryskin model.*

3.4.5 Ratio of ψ' to J/ψ

In section 3.4.4, the ideas of vector meson dominance and elastic scattering via the exchange of a pomeron in the framework of Regge theory were used to describe the elastic scattering process $\gamma p \rightarrow \psi p$. The first part of this section will examine what the VDM model predicts for the ratio of cross sections for the elastic production of ψ' and J/ψ , whilst the latter part of the section will look at an alternative model describing the same process, and how this relates to the ratio of the cross sections.

In the VDM, the ratio of the integrated cross sections for the photoproduction of ψ' to J/ψ depends only on the couplings of the vector mesons to the photon, provided that the b parameter is the same for both ψ' and J/ψ production.

$$\sigma(W) = \frac{1}{b} \frac{d\sigma(W, t=0)}{dt}. \quad (3.32)$$

For J/ψ production,

$$b = 2b_p + 2b_{J/\psi} + 2\alpha'_{\mathcal{P}} \ln \left(\frac{W}{W_0} \right)^2 \quad (3.33)$$

as described in section 3.3.1, where b_p and $b_{J/\psi}$ scale like the squared radius of the proton and J/ψ respectively. Since the radii of the J/ψ and the ψ' are much smaller than that of a proton (due to the large mass of the charm quark), the effect of their form factors on the t slope is much smaller than that of the proton. Hence the b parameter describing the t slope is dominated by the proton form factor, and is approximately the same for elastic photoproduction of J/ψ and ψ' . The couplings of the ψ' and J/ψ to the photon are related to the magnitude of the radial wavefunction at the origin, which in turn can be related to the leptonic decay width of the meson, as shown in figure 3.16. The width

for the decay $J/\psi \rightarrow e^+e^-$ is given by:

$$\Gamma(J/\psi \rightarrow e^+e^-) = \frac{4\pi\alpha^2}{f_{J/\psi}^2} \frac{m_{J/\psi}}{3} \quad (3.34)$$

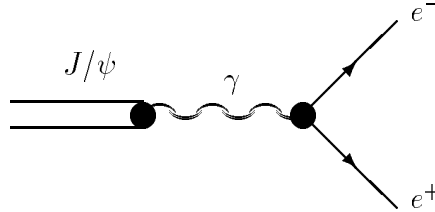


Figure 3.16: J/ψ decay to electron pair via an intermediate photon.

In the VDM, the ratio of the cross sections is therefore expected to be well approximated by the simple equation:

$$\frac{\sigma(\gamma p \rightarrow \psi' p)}{\sigma(\gamma p \rightarrow J/\psi p)} = \frac{\Gamma(\psi' \rightarrow e^+e^-)}{\Gamma(J/\psi \rightarrow e^+e^-)} \frac{m_{J/\psi}}{m_{\psi'}} \quad (3.35)$$

Using values for the mass and the decay widths from [64], this model predicts a ratio of $\sim 0.34 \pm 0.04$, where the error on the ratio comes from the uncertainties in the decay widths.

An alternative approach to this problem uses ‘colour dipole’ phenomenology to describe the diffractive photoproduction of vector mesons [61]. The photon first fluctuates to a colour dipole $c\bar{c}$ pair which interacts with the proton, where the interaction is mediated by the exchange of two gluons, before combining into the final state vector meson. The amplitude for the whole process, $T(\gamma p \rightarrow \psi p)$ may be factored into the product of those processes, *ie.*

$$T(\gamma p \rightarrow \psi p) = T(\gamma \rightarrow c\bar{c})T(p c\bar{c} \rightarrow p c\bar{c})T(c\bar{c} \rightarrow \psi). \quad (3.36)$$

The amplitude may be factorised in this way since the interaction of the $c\bar{c}$ pair with the proton takes place over a much shorter time-scale than either the fluctuation to the $c\bar{c}$ pair, or the final formation into the vector meson state. The transverse size of the $c\bar{c}$ fluctuation decreases with increasing Q^2 . The production amplitude for the final state vector meson is related to the cross section for the interaction with a proton of the $c\bar{c}$ colour dipole, $\sigma(r)$ (where r is the transverse separation of the $c\bar{c}$ pair), where $\sigma(r)$ receives its dominant contribution from [61]:

$$r \sim r_S \sim \frac{C}{\sqrt{m_V^2 + Q^2}}, \quad (3.37)$$

where C is estimated to be 6 [61]. This leads to the probing of the wave function of the vector meson at the *scanning radius*, r_S . The wave function for the 2S state, ψ' , has a node, and in the photoproduction limit, the amplitude receives strong cancellations between contributions to the amplitude from r above and below the node, leading to suppression of the 2S state relative to the 1S state, J/ψ [62]. As Q^2 increases, the scanning radius becomes smaller and the node effect negligible, so that the ratio of the production cross sections should increase. Kopeliovich and Zarkharov evaluate the size of this ratio at $Q^2 = 0$ [63]. The wave function for the diffractively produced $c\bar{c}$ pair, $|c\bar{c}\rangle$, is expressed as the product of the quark wavefunction of the photon and the amplitude of the colour dipole interaction with the proton. The ratio of the cross sections for the production of ψ' to J/ψ is then given by the ratio of the overlap integrals of the wavefunction $|c\bar{c}\rangle$ with those for the 1S and 2S bound states [63].

$$\frac{\sigma(\gamma p \rightarrow \psi' p)}{\sigma(\gamma p \rightarrow J/\psi p)} = \left| \frac{\langle \psi' | c\bar{c} \rangle}{\langle J/\psi | c\bar{c} \rangle} \right|^2 = 0.15 \quad (3.38)$$

The colour dipole model (CDM) differs from the naive VDM in attempting to model the photon fluctuation to a charm-anticharm pair, and subsequent conversion to a vector meson. The production of heavy vector meson states differs from light vector meson production in that there is a hard scale present in the interaction due to the mass of the charm quark. This hard scale, rather like p_T in the ‘anomalous’ contribution to the photon structure (see section 3.3.3), may inhibit the fast development of full vector meson state in advance of the target. The colour dipole model takes account of this, and views the interaction as taking place between the proton and the $c\bar{c}$ pair, rather than the elastic scattering of two hadrons. Measurement of the ratio of the total ψ' to J/ψ cross section is a sensitive means of testing the validity of each model, with the cross section ratio possibly differing by a factor of two. A further means by which the models may be distinguished comes from the Q^2 dependence of the ratio, which rises with Q^2 in the CDM, but is flat for the VDM.

Chapter 4

Event Selection

4.1 Introduction

Various production mechanisms for the quasi-elastic photoproduction ψ' mesons at H1 were discussed in the last chapter, and over the next two chapters, the measurement of the cross section for this process is presented. The method used for this measurement is to identify and count the number of ψ' mesons produced in this way, and obtain a cross section by determining the overall acceptance using Monte Carlo for triggering on and reconstructing such events. The data used to make this measurement were taken at H1 over 1994 and 1995.

The cross section is measured in a kinematic region where the acceptance is highest. The the first part of this chapter will explain the kinematics of the elastic production of ψ' mesons, and how the various kinematic variables are reconstructed. This is followed by a discussion of the Monte Carlo (MC) generator, DIFFVM, used in this analysis in the determination of the acceptance, and of the simulation of MC events in H1. Although the MC was used to determine the overall acceptance for a ψ' event, the individual efficiencies for trigger elements and lepton identification were also determined from data, in order to ensure that the MC gave a good simulation of the real data. Comparisons between these efficiencies determined using both data and MC were then used to estimate the systematic uncertainty on the overall acceptance determined from the MC. A brief overview of triggering at H1 was given in section 1.8. The various triggers used to specifically select charm candidates are described in this chapter, together with a study of the efficiency of the trigger elements which comprise these triggers. Efficiencies are evaluated both from MC simulations and, by using the redundancy of H1, directly from data. The ψ' candidates are identified from their decays into one of four channels, shown in table

4.1. Although these branching ratios are small, it is the distinctive leptonic decays that

Decay Channel	Branching Ratio (%)
$\psi' \rightarrow J/\psi(\rightarrow \mu^+\mu^-)\pi^+\pi^-$	1.9 ± 0.2
$\psi' \rightarrow J/\psi(\rightarrow e^+e^-)\pi^+\pi^-$	2.0 ± 0.2
$\psi' \rightarrow \mu^+\mu^-$	0.77 ± 0.17
$\psi' \rightarrow e^+e^-$	0.88 ± 0.13

Table 4.1: *Decay channels used to identify the ψ' , and the corresponding branching ratios. The branching ratios are taken from [64].*

make the identification possible. A crucial step in the reconstruction of a ψ' candidate is therefore the identification of electrons or muons in an event. The methods used to achieve this are discussed, and the efficiencies derived from both data and MC are shown. If the ψ' meson is produced in isolation in H1, the decay channels shown in table 4.1 will lead to either four or two tracks in the observed final state. The selection criteria used to define a ‘good’ track are described in this chapter. The final selections used to measure the cross section are then described for each of the decay channels, and the chapter concludes with a brief outline of the kinematic acceptance of the chosen selection for such events, as a function of the kinematic variables.

The next chapter shows the signals obtained from the final event selection, and then describes how the MC is used to determine the overall acceptance. The means of determination of the systematic uncertainties in this acceptance are also presented. The cross sections are presented separately for each of the four track decay channels from the 1994 and the 1995 data, and a combined measurement is then performed. This is followed by a presentation of the same cross section determined from the two track decay channels. In this case, data from 1994 and 1995 was combined, which was necessary due to poor statistics and difficulties in background determination. The measurement was performed as a cross check on the cross section as obtained from the four track sample. Finally, the results are compared with previous measurements from lower energy fixed target experiments, and with theoretical predictions.

4.2 Event kinematics

Events are rejected where the scattered positron is detected in the main calorimeters in order to restrict the sample to the region where $Q^2 < 4 \text{ GeV}^2$ ($Q^2 < 1.2 \text{ GeV}^2$ in 1995 data). The cross section peaks sharply at low Q^2 , so the data sample retained has Q^2 very close to zero. The photoproduction cross section of a particular vector meson is dependent on the variables $W_{\gamma p}$, the centre of mass energy of the photon proton system,

z , the elasticity of the event, and t , the four momentum transfer squared. Reconstructing the event kinematics becomes more difficult when the scattered lepton is not detected. In this case, the kinematic variable, y defined in equation 3.3, can be reconstructed using the Jaquet-Blondel method.

$$y_{JB} = \sum \frac{(E - p_z)}{2E_e}, \quad (4.1)$$

where the sum is made over all particles in the event (excluding the scattered electron). E_e is the electron beam energy, and y is the fraction of the the electron beam energy taken by the photon in the rest frame of the proton. This variable is insensitive to losses of tracks very close to the proton beam direction where $p_z \simeq E$. The variables $W_{\gamma p}$ and z are then given in terms of the reconstructed y_{JB} and the beam energies by

$$W_{\gamma p}^2 \simeq 4E_e E_p y_{JB}; \quad (4.2)$$

$$z_{rec} = \frac{(E - p_z)\psi'}{2y_{JB}E_e}. \quad (4.3)$$

Figure 4.1 shows the reconstructed versus the generated values of W and y , for Monte Carlo events, where the ψ' has been reconstructed using the techniques discussed later.

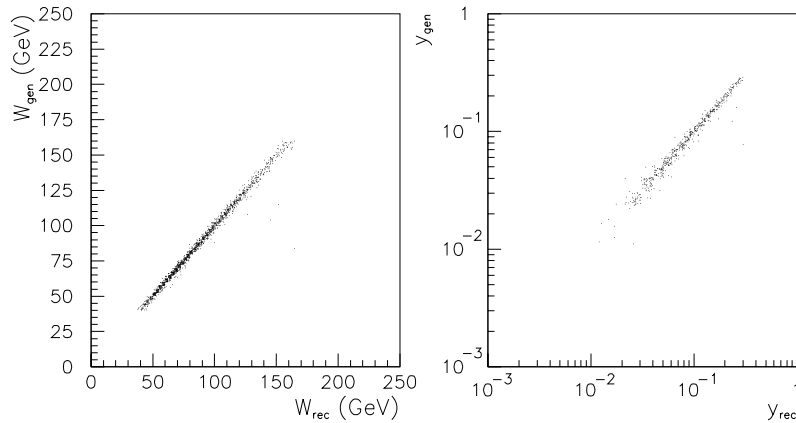


Figure 4.1: *The left hand plot shows the generated values for $W_{\gamma p}$ versus the reconstructed values, and the right hand plot shows the same for y_{JB} .*

Events with a high value of z ($z > 0.95$) are described as ‘quasi-elastic’, and are generally very clean events with the decay products of the ψ' being the only activity in the detector. Purely elastic events have $z=1$, whilst events where the proton dissociates have values of z close to 1. The quantity z is reconstructed with a much wider spread in z than is

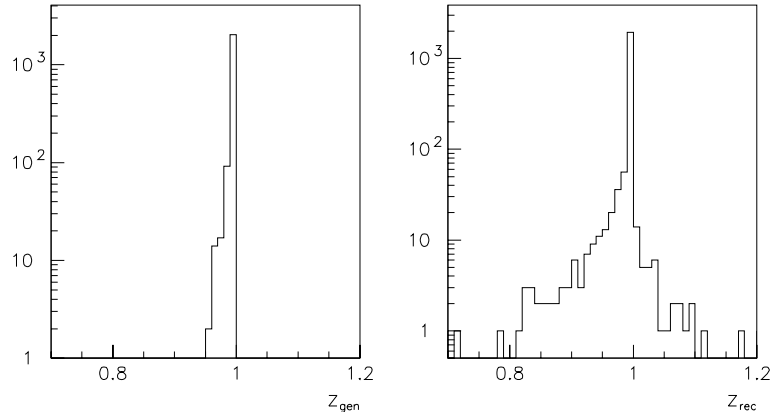


Figure 4.2: *Generated and reconstructed values for the elasticity variable z*

obtained from the generated values (see figure 4.2). No cuts are placed specifically on z in the analysis, although the region of acceptance in z is limited to $z > 0.95$ by the demand that there are exactly two or four reconstructed tracks in the event. The kinematic acceptance of the selection described below is shown at the end of this chapter.

4.3 Monte Carlo Simulation

4.3.1 The DIFFVM event generator

The Monte Carlo generator used in this analysis was DIFFVM [65], which is based on the Vector Dominance Model described in section 3.3.2. DIFFVM was originally designed to describe the elastic production of light vector mesons (ρ, ω, ϕ) and has now been generalised to describe the production of the charmonium states J/ψ and ψ' . Both the purely elastic process ($\gamma p \rightarrow \psi' p$), and the process in which the proton dissociates ($\gamma p \rightarrow \psi' X$) are modelled. The cross section behaviour is assumed to vary with the centre of mass energy, $W_{\gamma p}$, according to

$$\sigma \propto W^{4\epsilon}, \quad (4.4)$$

where the parameter ϵ is set at 0.225, in accordance with the analysis of the J/ψ data at H1 [52] (see section 3.4.4). The dependence of the cross section on the four-momentum transfer, t , is given by

$$\frac{d\sigma}{dt} \propto e^{bt}, \quad (4.5)$$

where $b = 4.0 \text{ GeV}^{-2}$ is taken in the elastic case, and 1.6 GeV^{-2} for proton dissociation. These parameters are also taken to match those from the J/ψ data. The b parameters are set at a constant value with no energy dependence, *ie.* $\alpha'_{\mathcal{P}}$ is set to zero. Analysis of the p_T distributions of the J/ψ data showed that the measured b -slopes were consistent with a constant value over the energy range covered by the measurement.

In the case where the proton dissociates, the cross section dependence is taken to be

$$\frac{d\sigma}{dM_X^2} \propto \left(\frac{1}{M_X^2} \right)^{\alpha_{\mathcal{P}}(0)}, \quad (4.6)$$

where M_X is the mass of the proton remnant, and $\alpha_{\mathcal{P}}(0) = 1.0808$ in accordance with measurements from pp scattering experiments [28].

In order to determine the acceptance for ψ' events, a mixture of elastic and proton dissociative events was used, and the fraction of each was taken as 45% elastic and 55% proton dissociation, to match the ratio from the J/ψ analysis [52].

In the case where the ψ' decays directly to two leptons, the angular distribution of the decay particles is generated in DIFFVM assuming s-channel helicity conservation. If θ^* is the angle in the J/ψ rest frame between the direction of the positively charged lepton and the J/ψ direction in the γp cms, then the differential cross section is given by

$$\frac{d\sigma}{d \cos \theta^*} = \frac{1 + \cos^2 \theta^*}{2}. \quad (4.7)$$

When the ψ' decays to a J/ψ and two pions, the distribution of the three particles is generated according to three body phase space. Previous experiments have measured different invariant mass distributions of the dipion system compared to that expected from phase space. The MC was therefore reweighted in order that the dipion mass distribution agree with measured distributions. This is discussed further in section 5.2.

4.3.2 Simulation

The generator DIFFVM simulates the process occurring at the event vertex, namely $\gamma p \rightarrow \psi' X$. The next stage is the simulation of the passage of the resulting final state particles through the detector. This is done by the H1 simulation package H1SIM [66], which is based on the GEANT package. The generated particles are tracked through the detector, and the response of the detector as the particles pass through is modelled. The output from the simulation has the same form as that produced by real data, so that it is available to be reconstructed in the same way. The response of the individual subtriggers and trigger elements is also simulated, although the trigger prescale factors

are not taken into account. The simulation is carried out using a database that matches changes with run range in the data, so that factors such as dead wires may be included in the simulation. The motivation behind this is that the simulated data should resemble real data in every respect. In this analysis, the MC simulated data is used to calculate the overall acceptance of ψ' events, hence it is important that the simulation gives an accurate representation of the detector in terms of acceptances, reconstruction efficiencies and resolutions. These will be discussed in the following sections.

4.4 Triggering

4.4.1 L1 subtriggers

Events where the J/ψ or ψ' decays to two electrons are triggered on either an electron from the decay (subtrigger 52), or by requiring a particular event topology (subtrigger 54). Events where the J/ψ or ψ' decays to two muons are triggered on one of the muons from the decay, where the muon is identified as a track in the instrumented iron. There were three main triggers which utilised this information in 1994 and 1995 running, namely subtriggers 18, 19 and 22.

The trigger elements which comprise these triggers are shown in table 4.2, and described in the following sections.

Subtrigger	Trigger elements
st52	LAr_BR AND $DCRPh_Ta$ AND $zVtx_Cls$ AND (NOT LAr_IF)
st54	$Topo_BR$ AND $DCRPh_TNeg$ AND $zVtx_Cls$
st18	Mu_ECQ AND $DCRPh_Ta$ AND ($zVtx_small$ OR $zVtx_sig1$)
st19	Mu_Bar AND $DCRPh_Ta$ AND ($zVtx_small$ OR $zVtx_sig1$)
st22	Mu_BEC AND ($zVtx_small$ OR $zVtx_sig1$)

Table 4.2: Logical make up of the L1 subtriggers used in the analysis

4.4.2 The Liquid Argon bigray trigger element (LAr_BR)

Electrons are identified as electromagnetic clusters in the Liquid Argon Calorimeter. Typical energies of electrons from the decays of both J/ψ and ψ' are of the order of 1-2 GeV. This therefore presents a challenge to the LAr trigger, as these energies are only a few sigma above noise. The LAr trigger was originally designed to trigger on a high energy electron (or positron) from high Q^2 DIS events. In order to overcome the difficulties of

triggering on low energy electrons, a combination of information from the calorimeter and the proportional chambers is used. In 1994 the LAr bigray trigger element was introduced [67], which requires a track with momentum larger than 600 MeV pointing towards a signal from a LAr bigtower.

The efficiency of the LAr bigray trigger element was studied using a sample of dielectron events triggered by subtrigger 54 (*st54*), which is independent of the LAr calorimeter. Events within a window of ± 300 MeV of the nominal J/ψ mass were selected for the study, to ensure that a clean sample of electrons from J/ψ decays was obtained. This study was carried out on samples of data from both 1994 and 1995, and the results are shown in figures 4.3 and 4.4.

For the region $20^\circ < \theta(\text{el}) < 140^\circ$ and $p(\text{el}) > 1$ GeV, the efficiency of the LAr bigray trigger element was found to be $48.1 \pm 3.5\%$ from 1994 data, and $44.2 \pm 3.2\%$ from 1995 data. These and all subsequent efficiency results are summarised in table 4.3.

4.4.3 The topological trigger element (*Topo_BR*)

The trigger element *Topo_BR* is based on the requirement of two tracks from the proportional chambers (CIP and COP) lying back-to-back in the r - ϕ plane. In 1995 the trigger element was defined slightly differently to that in 1994, and had the additional requirement that there were no other rays apart from those with the back-to-back topology. The efficiency of this trigger element was studied using a sample of J/ψ events, where the J/ψ decays to two leptons. The sample was selected from events which had been triggered by the muon triggers (*st18*, *st19* and *st22*) and by the LAr bigray trigger (*st52*).

The results are shown in figures 4.3 and 4.4. For the region $20^\circ < \theta(\text{both tracks}) < 140^\circ$ and $p_T > 1$ GeV, the efficiency of the topological trigger element was found to be $57.6 \pm 2.0\%$ from 1994 data, and $55.6 \pm 3.1\%$ from 1995 data.

4.4.4 Muon trigger elements

Subtriggers 18,19 and 22 are comprised of trigger elements specifically designed to trigger on muon candidates, together with other trigger elements, for example z -vertex and track requirements. The instrumented iron provides 8 bits of information at L1, for muons in the backward endcap, the forward endcap, and the central barrel region. The trigger element *Mu_ECQ* is an OR condition of the inner and outer backward endcap elements, and the forward outer endcap element. The trigger element *Mu_BEC* triggers on a track

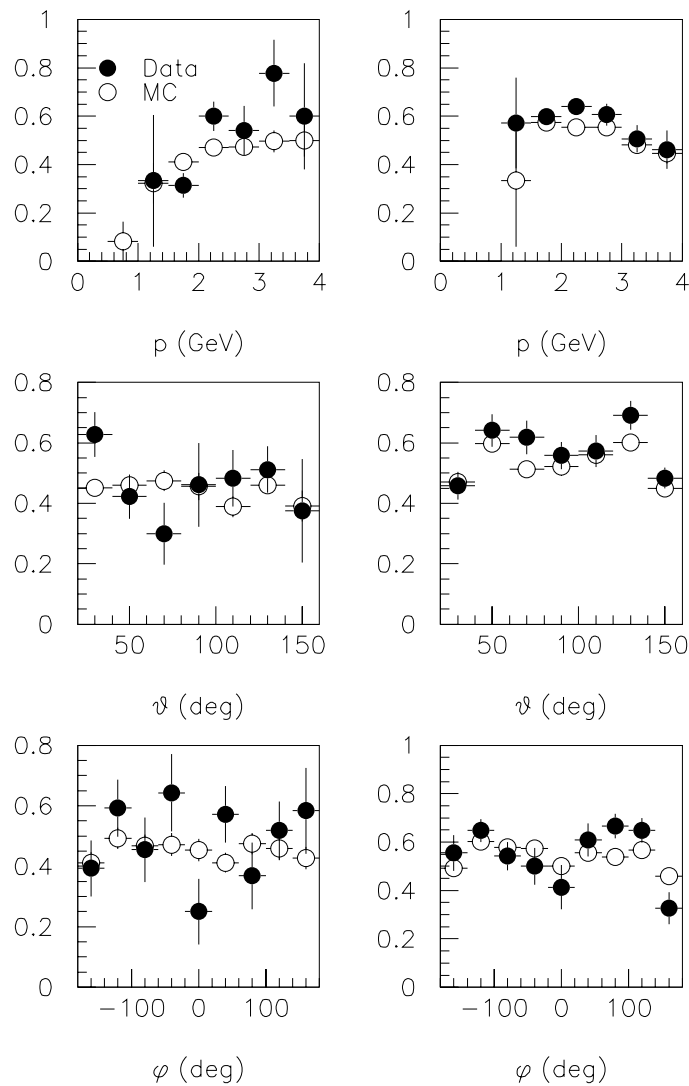


Figure 4.3: The three plots on the left hand side show the efficiency for *LAr_BR* as a function of momentum, θ and ϕ from 1994 data. The three right hand plots show the corresponding efficiencies for *Topo_BR*. The data points show the efficiency determined from the J/ψ sample of data, and the MC points are determined using a mixture of the elastic and proton dissociative ψ' DIFFVM MC.

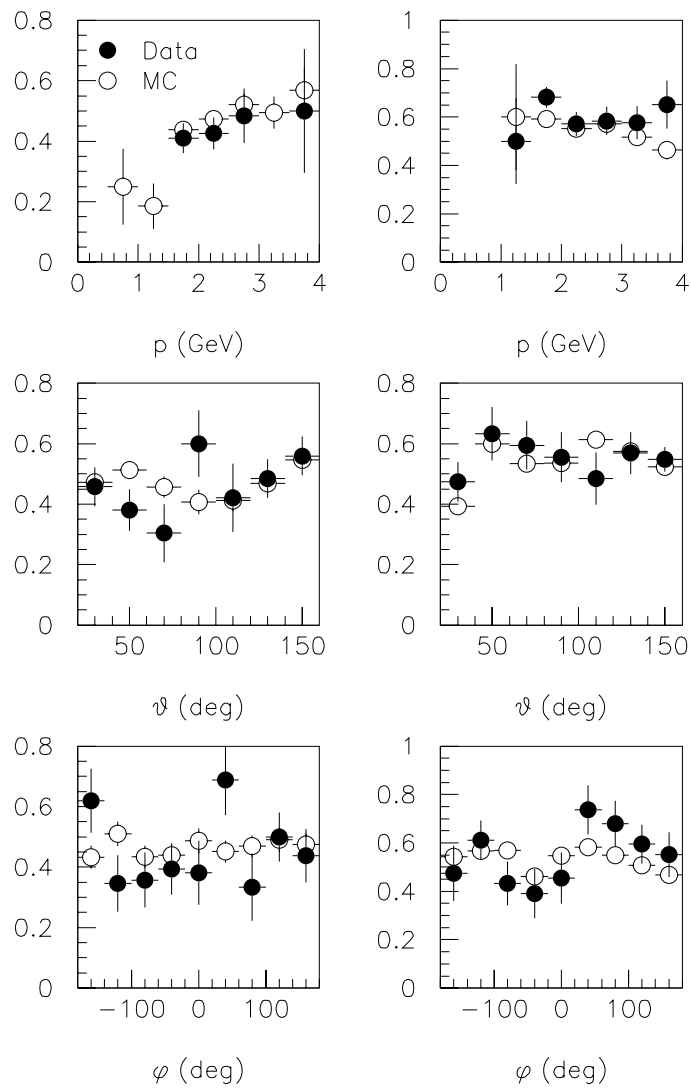


Figure 4.4: Efficiencies for the topological and LAr bigray trigger elements for 1995 data.

segment in either the inner or outer backward endcap, and *Mu_Bar* on a track segment in the central barrel. The efficiency of these trigger elements was studied using a sample of dimuon events triggered on the topological trigger (*st54*). A cut of ± 300 MeV was placed around the nominal J/ψ mass and the charged multiplicity of the event was restricted to four, to ensure that a clean sample of $J/\psi \rightarrow \mu^+\mu^-$ events was obtained. The results for 1994 data are shown in figure 4.5 and for 1995 data in figure 4.6.

The efficiency for the backward iron endcap trigger element in the region $140^\circ < \theta < 170^\circ$ and $p > 1$ GeV was found to be $65.8 \pm 3.7\%$ from 1994 data and $65.1 \pm 2.7\%$ from 1995 data. The efficiency for the forward outer endcap was measured over the region $10^\circ < \theta < 35^\circ$ and $p > 1$ GeV and was found to be $9.9 \pm 2.8\%$ and $12.8 \pm 2.4\%$ for 1994 and 1995 respectively. The efficiency of this trigger element rises with the momentum of the muon, and the low value for this figure is an artifact of the momentum distribution of the muons from the ψ' decay. The relatively large errors on these efficiencies reflect the poor statistics from this trigger element. Finally, the efficiency for the iron barrel was measured over the region $40^\circ < \theta < 140^\circ$, and $p > 2$ GeV, and was found to be $69.5 \pm 6.4\%$ (1994) and $68.9 \pm 4.5\%$ (1995).

4.4.5 The Z-Vertex trigger elements

The z -vertex trigger uses tracks from the proportional chambers of both the central and forward tracker. All possible tracks are extrapolated back to the beam axis, and a histogram with 16 bins, each of 5.4 cm in z , is constructed from the z positions of each track at $r = 0$. A z -vertex is identified by a peak in this histogram. Low multiplicity events, however, clearly do not have enough entries in the histogram to produce a significant peak. The trigger element *zVtx_Cls* demands that all entries in the z -vertex histogram lie within 4 neighbouring bins, and therefore favours low multiplicity events, because the number of wrong track combinations is reduced. This trigger element forms a part of both subtriggers 52 and 54, which were specifically designed to trigger on elastic J/ψ events. The trigger element *zVtx_small* is similarly designed for low multiplicity events. It demands that both the peak of the histogram and the total sum over all the other bins are smaller than certain pre-defined parameters. A further element *zVtx_sig1* looks for a significant peak in the histogram above a certain threshold level. The muon triggers used in this analysis, subtriggers 18, 19 and 22, have a z -vertex requirement of either *zVtx_small* OR *zVtx_sig1*.

The efficiency of these trigger elements was studied using a sample of data triggered by independent DIS subtriggers. Only events with 4 tracks or less were accepted, where there

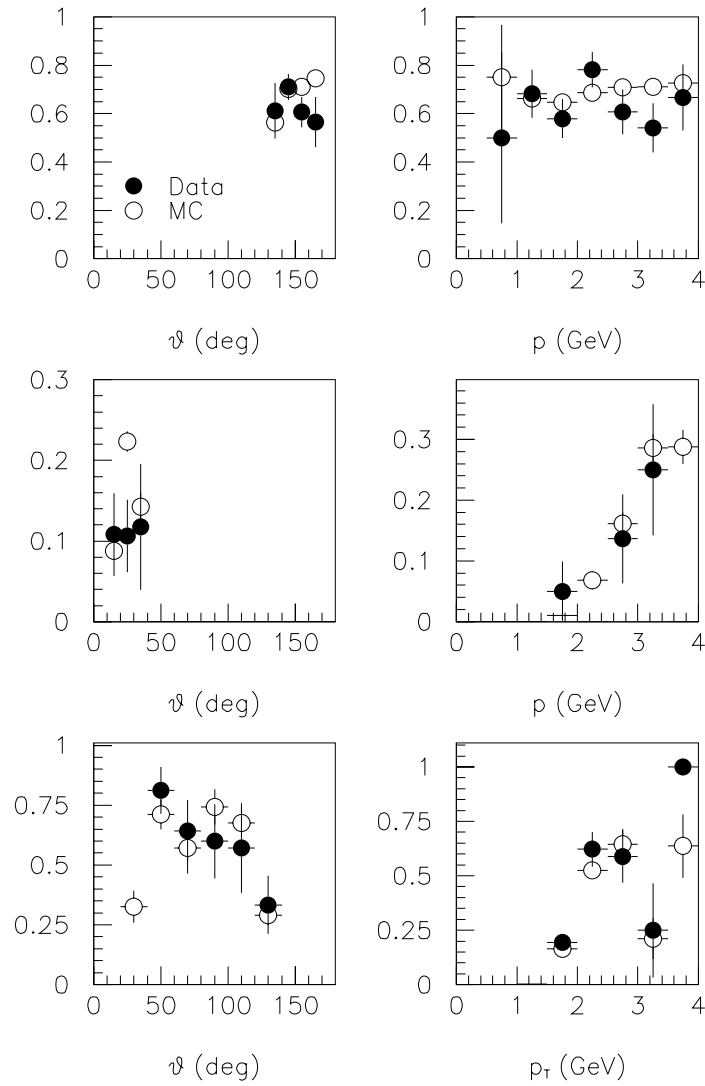


Figure 4.5: The upper two plots show the efficiency for the backward iron endcap trigger element as a function of θ and p for 1994 data. The middle two plots show the corresponding efficiencies for the forward outer iron endcap, and the lower two plots for the iron barrel.

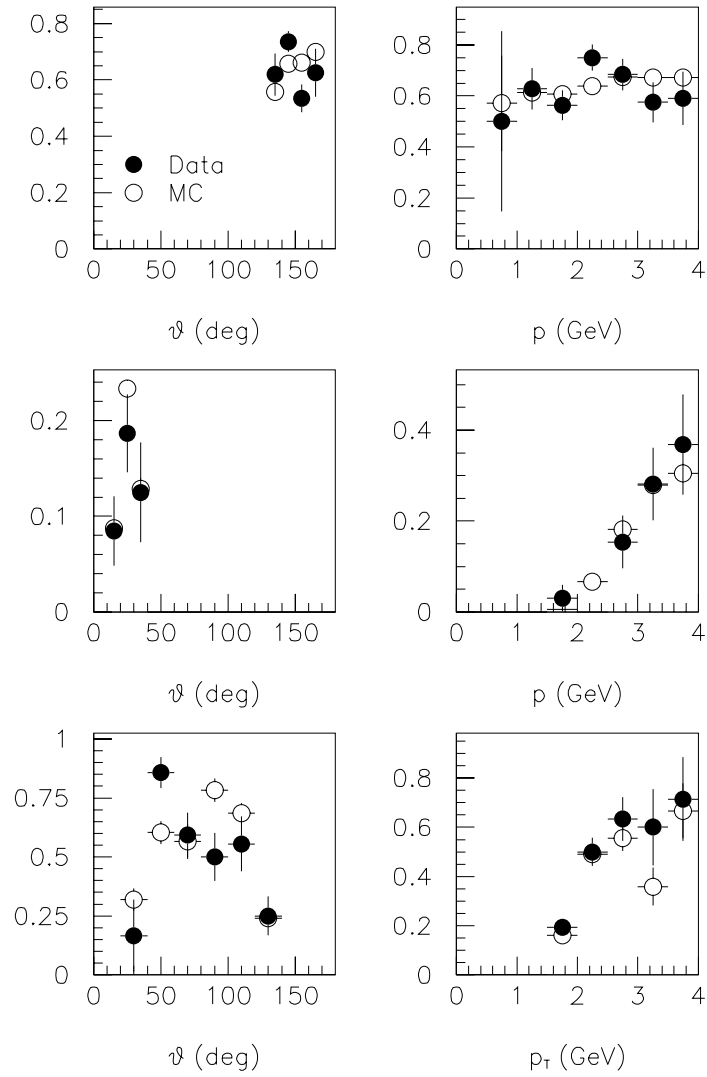


Figure 4.6: Efficiency plots for the backward and forward iron endcaps, and barrel trigger elements from 1995 data

were two identified leptons of opposite charge with an invariant mass that lay in the region $2.5 < M(l^+l^-) < 4.0$ GeV, and where both the lepton tracks lay in the angular region $20^\circ < \theta < 160^\circ$. This gave a sample of J/ψ candidate events, triggered independently of the z -vertex trigger, which were then used to determine the efficiency of the z -vertex trigger elements. The efficiency for the event to trigger the element $zVtx_Cls$ was found to be 85.7 ± 5.4 and 77.6 ± 4.8 from the 1994 and 1995 data respectively. Similarly, the efficiency for the condition $zVtx_small$ OR $zVtx_sig1$ was found to be 92.9 ± 4.0 and 89.5 ± 3.5 from the 1994 and 1995 data respectively.

4.4.6 Track trigger elements

The trigger elements $DCRPh_Ta$ and $DCRPh_TNeg$ are designed to trigger on tracks identified passing through the central tracker. The CJC is able to distinguish between tracks of low and high momentum, and determine the charge for low momentum tracks. In order to suppress background events, the tracks must have a distance of closest approach to the beam axis measured to be less than 2 cm. The trigger element $DCRPh_Ta$ requires that one track is found, whilst $DCRPh_TNeg$ requires at least one negative track.

The $DCRPh$ trigger elements were studied using a sample of low multiplicity events, with at least one identified lepton, triggered by the DIS trigger, $st0$, which does not require any tracks or vertex. Events were selected where there was exactly one reconstructed track in the central part of the detectors, and were tested to ascertain whether or not the track had fired the $DCRPh$ trigger elements.

The results are shown in figures 4.7 and 4.8. For the region $p > 0.5$ GeV and $50^\circ < \theta < 150^\circ$, the efficiency for the $DCRPh_Ta$ trigger element was found to be $72.7 \pm 1.0\%$ from 1994 data, and $76.1 \pm 1.0\%$ in 1995. The efficiency for the $DCRPh_TNeg$ trigger element was measured in the same region as $73.9 \pm 1.6\%$ in 1994, and $78.3 \pm 1.5\%$ in 1995 (for negative tracks only).

4.4.7 Veto elements

Subtrigger 52 has the requirement that the trigger element LAr_IF should not be set. This trigger element demands that the sum of the energy in the inner forward part of the LAr calorimeter passes a certain threshold value. Demanding that LAr_IF is not set prevents $st52$ from triggering on events which have a lot of energy in the forward direction. The efficiency was studied using a sample of quasi-elastic J/ψ events, where

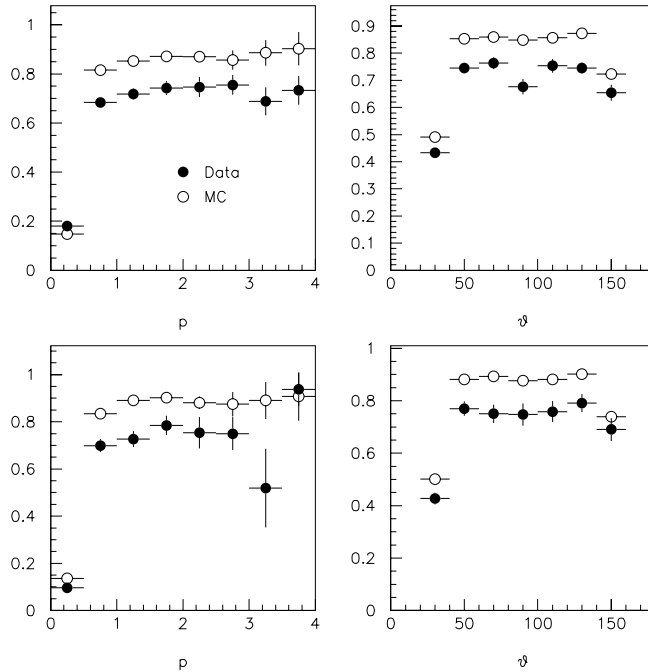


Figure 4.7: The upper two plots show the efficiency of the $DCRPh_Ta$ trigger element as a function of the p_T of the track and of θ . The lower two are the corresponding plots for the trigger element $DCRPh_TNeg$. The efficiencies are found using 1994 data.

the J/ψ decays to two leptons triggered by one of the subtriggers 54, 18, 19 and 22. Events where the two leptons were the only two tracks reconstructed were selected, and this sample was used to determine the probability of rejecting such events due to the NOT LAr_IF condition.

The set of subtriggers used in this analysis also contain various vetoes based on timing which are designed to deselect background events which are out of time with the bunch crossing, and should not trigger on real physics events. These are not simulated in the MC, and the rate at which they veto physics events is estimated to be less than 4% [68].

These efficiency studies were also carried out using DIFFVM MC simulated data, where a mixture of elastic and proton dissociative events were used. The results of the efficiencies for each trigger element determined from both data and MC are summarised in table 4.3.

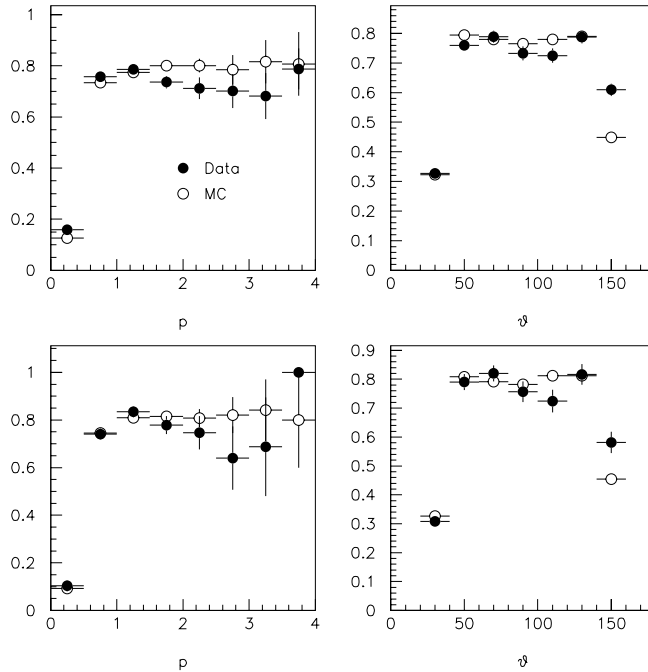


Figure 4.8: The upper two plots show the efficiency of the *DCRPh-Ta* trigger element as a function of the p_T of the track and of θ , using 1995 data. The lower two are the corresponding plots for the trigger element *DCRPh-TNeg*.

4.5 Lepton identification

Leptons are identified by linking a track reconstructed in the central or forward trackers to a track segments in the iron, or to clusters in the LAr calorimeter.

4.5.1 Identification in the Liquid Argon Calorimeter

The LAr calorimeter is used to identify both muons and electrons. Each track is extrapolated to the calorimeter, and any cells and clusters which lie within a certain radius (15 cm for the EMC and 30 cm for the HAC) of the extrapolated track are associated with it. Electrons are identified by a track linked to an electromagnetic cluster, where there is a minimal amount of activity ($E_{HAC} < 0.3 \text{ GeV}$) in the hadronic part of the calorimeter behind the linked cluster. Cuts are made on the ratio E/p where E is the energy of the electromagnetic cluster and p is the momentum of the associated track. Muons are identified as minimum ionising particles in the LAr calorimeter. A track is linked to clusters in both the electromagnetic and hadronic parts of the calorimeter. Cuts are made on the energy and the length of the clusters.

Trigger Element	Efficiency (%) in 1994		Efficiency (%) in 1995	
	Data	Monte Carlo	Data	Monte Carlo
<i>Mu_BEC</i>	65.8 ± 3.7	69.5 ± 0.8	65.1 ± 2.7	65.1 ± 0.6
<i>Mu_FOEC</i>	9.9 ± 2.8	14.5 ± 0.7	12.8 ± 2.4	14.5 ± 0.5
<i>Mu_Bar</i>	69.5 ± 6.4	68.3 ± 3.5	68.9 ± 4.4	67.5 ± 2.5
<i>LAr_BR</i>	48.1 ± 3.5	45.1 ± 1.2	44.2 ± 3.2	46.4 ± 1.4
<i>Topo_BR</i>	57.6 ± 2.0	54.1 ± 0.9	55.6 ± 3.1	53.2 ± 1.0
<i>zVtx_Cls</i>	85.7 ± 5.4	84.6 ± 0.3	77.6 ± 4.8	82.2 ± 0.3
<i>zVtx_Small</i> OR <i>zVtx_Sig1</i>	92.9 ± 4.0	93.7 ± 0.3	89.5 ± 3.5	94.1 ± 0.2
<i>DCRPh-Ta</i>	74.2 ± 1.0	86.1 ± 0.3	76.1 ± 0.7	78.2 ± 0.4
<i>DCRPh-TNeg</i>	76.6 ± 1.5	89.0 ± 0.4	78.7 ± 1.1	80.2 ± 0.5
NOT <i>LAr_IF</i>	90.0 ± 0.8	87.2 ± 0.3	90.5 ± 0.8	82.9 ± 0.7

Table 4.3: Trigger element efficiencies

4.5.2 Identification in the Instrumented Iron

Muons are also identified in the instrumented iron which surrounds the solenoid, and this extends the angular acceptance for the identification of muons compared to electrons. Tracks from the central and forward trackers are extrapolated to the iron, and linked to tracks formed in the iron from hits in the instrumented layers (see section 1.4.4). Cuts are made on the probability of a link between the two tracks.

4.5.3 Efficiency of lepton identification

A sample of events, where there was exactly two reconstructed tracks in the event, was selected to study the efficiency of muon and electron identification. The two tracks were required to pass the selection criteria for tracks described in section 4.6 and were required to be of opposite charge. The sample contained only events where at least one track was identified as a lepton. The invariant mass of the two track system was calculated (see figure 4.9), and only events within the region $2.8 < M(l^+l^-) < 3.4\text{GeV}$ were used in the efficiency study. It was assumed that all the events that lay in this mass region were dilepton events. In reality, this region contains dilepton events from both J/ψ decay and $\gamma\gamma$ events, as well as two track events where one of the tracks has been misidentified as a lepton. The advantage of restricting the sample to a small mass window around the nominal J/ψ mass is that the proportion of these ‘misidentification events’ is kept to a minimum. The lepton identification efficiency could then be found by comparing the number of events with both leptons identified in either the LAr calorimeter or in the iron, to the total number. This gives a ratio, δ , which may be defined as the fraction of events

where both leptons are identified. The ratio, δ , calculated using this method, is a function of the identification efficiency, ϵ .

$$\delta = \frac{\text{Probability of identifying 2 leptons}}{\text{Probability of identifying at least 1 lepton}}. \quad (4.8)$$

The lepton identification efficiency is therefore given by

$$\epsilon = \frac{2\delta}{1 + \delta}, \quad \sigma_\epsilon = \frac{2}{(1 + \delta)^2} \sigma_\delta. \quad (4.9)$$

This study was also carried using DIFFVM MC J/ψ events. The results are shown in figures 4.10 and 4.11, and the values calculated for the efficiencies from data and from MC are shown in table 4.4.

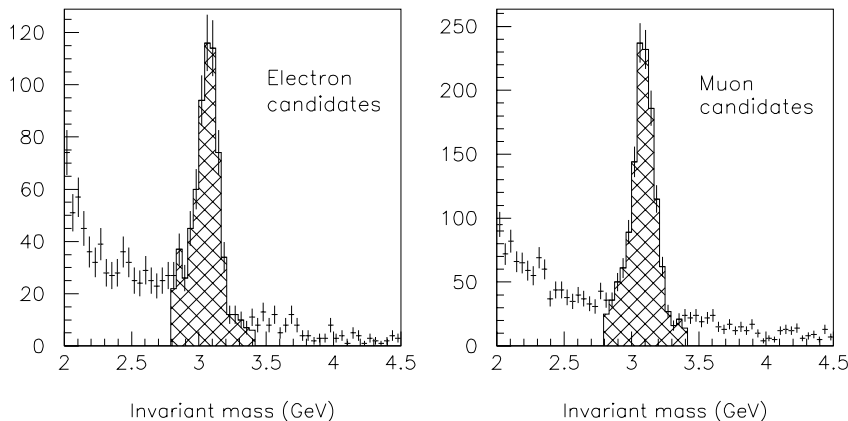


Figure 4.9: *Invariant mass distributions for two track samples where at least one lepton is identified. The hatched histograms show the selection for the lepton identification efficiency studies.*

	Efficiency in 1994 (%)		Efficiency in 1995 (%)	
	Data	MC	Data	MC
Electrons in LAC ($20^\circ < \theta < 140^\circ$)	92.4 ± 0.7	88.3 ± 0.3	87.5 ± 1.6	94.5 ± 0.3
Muons in LAC ($20^\circ < \theta < 60^\circ$)	80.4 ± 2.5	90.8 ± 0.4	82.6 ± 4.3	90.2 ± 1.0
Muons in LAC ($60^\circ < \theta < 140^\circ$)	79.2 ± 1.8	86.4 ± 0.9	93.7 ± 2.6	95.3 ± 0.7
Muons in Iron (all θ)	57.1 ± 1.8	49.4 ± 0.5	55.6 ± 2.7	50.3 ± 0.4

Table 4.4: *Lepton identification efficiencies in the LAr calorimeter and in the instrumented iron in 1994 and 1995 data*

4.6 Track selection

All tracks required to have a reconstructed vertex and a minimum p_T of 120 MeV:

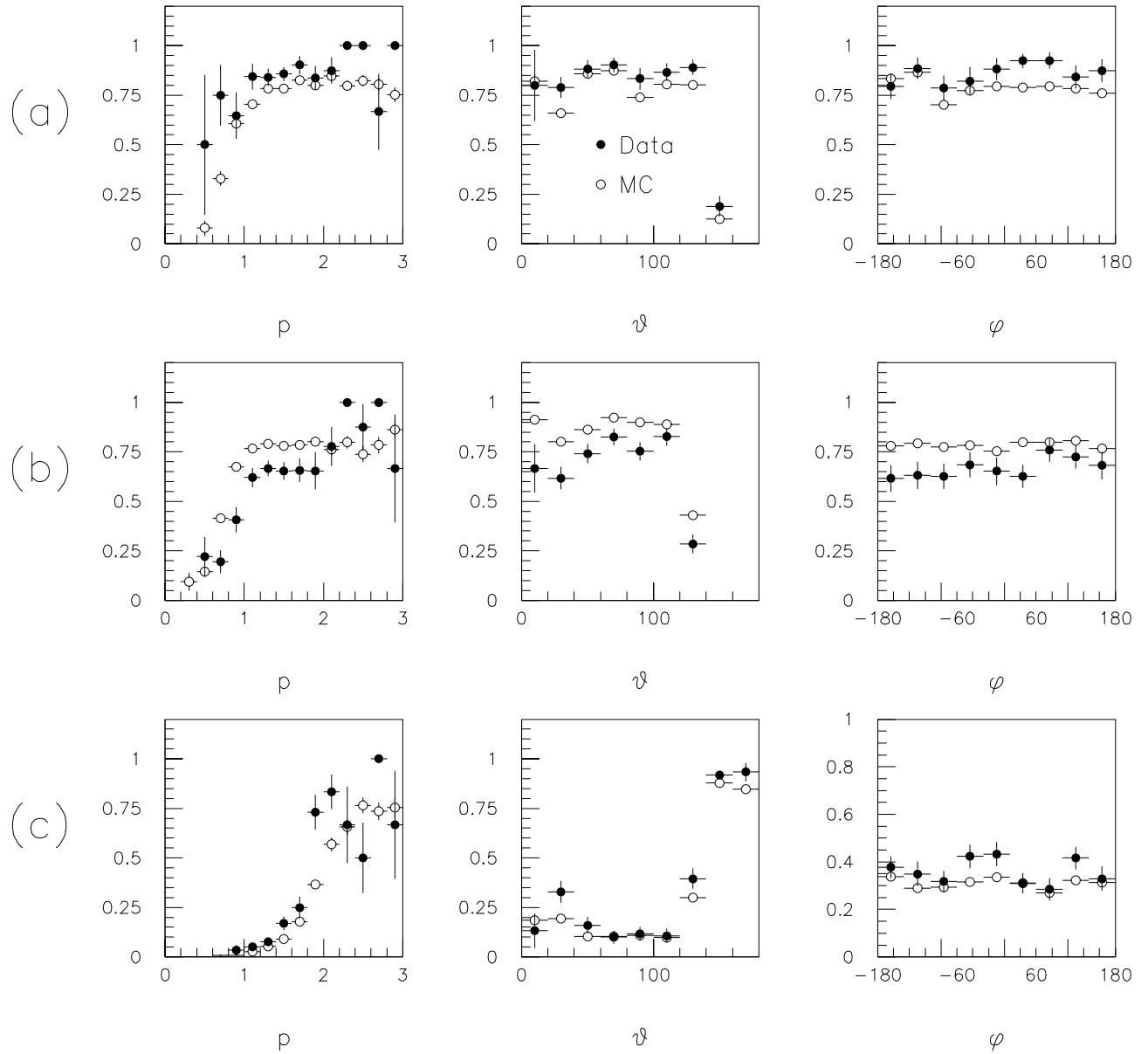


Figure 4.10: (a) The upper three plots show the ratio, δ , for electron identification in the LAr calorimeter as a function of p_T , θ and ϕ . The middle row, (b), shows the equivalent plots for muon identification in the LAr calorimeter, and the lower plots, (c), are of muon identification efficiencies in the Iron. The data are taken from 1994.

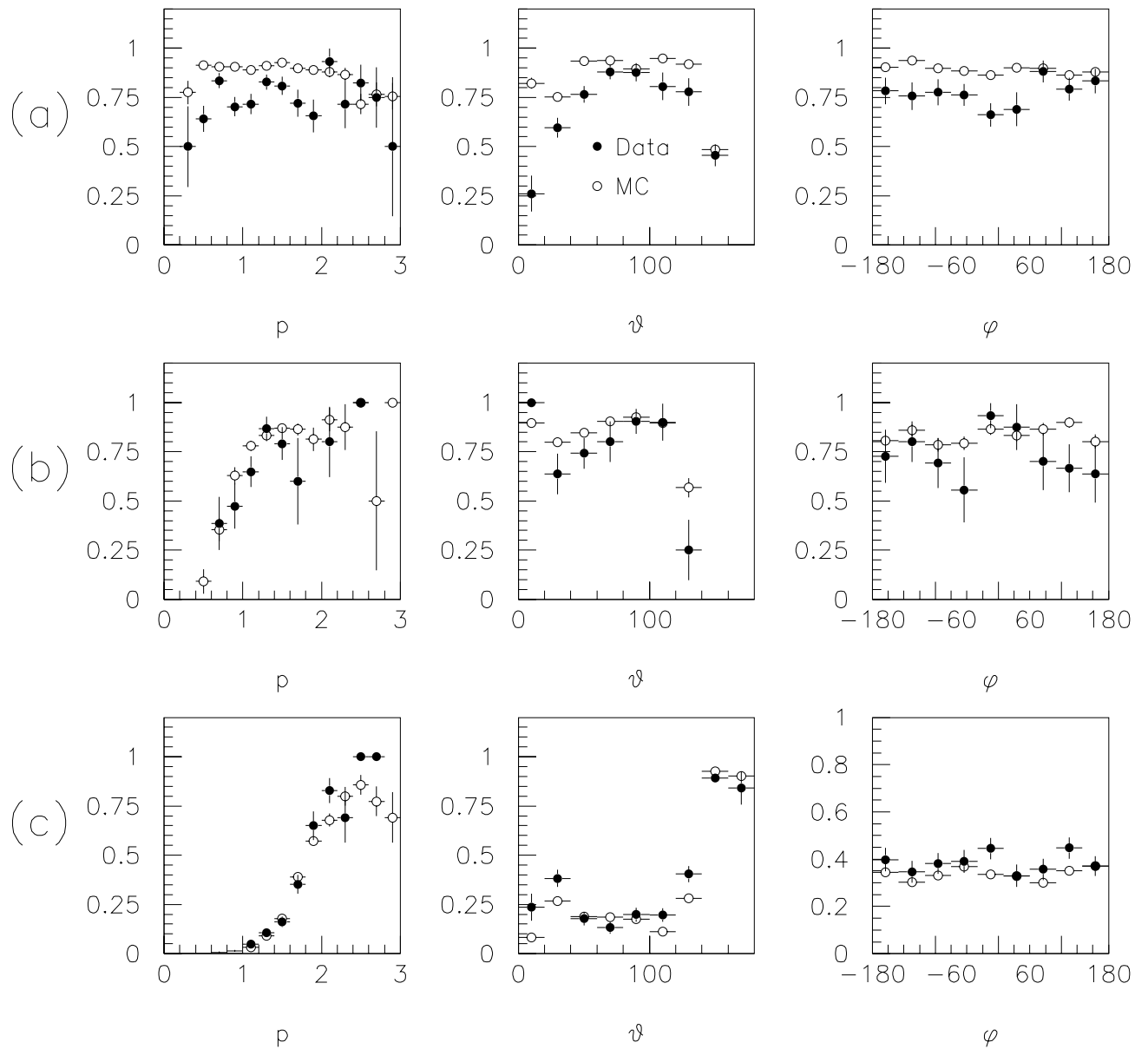


Figure 4.11: *Lepton identification efficiencies in the 1995 data, where plots (a) correspond to electron identification in the LAr, (b) to muon identification in the LAr, and (c) muon identification in the Iron.*

- $p_T > 120 \text{ MeV}$
- $-25 < zvtx < 35 \text{ cm}$

The cuts of forward tracks were:

- $\theta > 8^\circ$
- $R_0 < 10 \text{ cm}$
- At least one primary planar segment

The cuts on central tracks were:

- Number of hits in CJC1 > 0
- $R_{len} > 10 \text{ cm}$
- $DCA' < 2 \text{ cm}$
- $20 < \theta < 165^\circ$

The value R_0 is the radial distance from the z -axis of a forward track extrapolated back to the vertex in the xy plane. This cut is useful in removing secondaries, *ie.* tracks which do not come from the primary vertex. Demanding at least one primary planar segment ensures a forward track of a reasonable quality. The quantity DCA' refers to the distance of closest approach to the actual vertex. R_{len} is the radial track length. The cuts on the radial track length and the number of hits in CJC1 are useful in removing ‘ghost tracks’. These appear when a track in the central trackers is reconstructed as two tracks, one with hits from CJC1, and one with hits from CJC2. The cuts on p_T and θ restrict consideration to a region where the Monte Carlo modelling of the data is well understood, because the acceptance is good and uniform.

The track cuts are kept as loose as possible so that the soft pion tracks from the decay $\psi' \rightarrow J/\psi \pi \pi$ are not rejected, and hence ψ' candidates lost. Also, if the track cuts were too restrictive, events would be selected where there are more than four (or two) tracks in the event, and the event samples will become contaminated with background. The background consists not only of events which are not ψ' candidates, but also of ψ' events which have a value of z which is less than 0.95, *ie.* events which are not quasi-elastic (see section 4.8).

4.7 Selection of ψ' Candidates

4.7.1 Four track sample

Data samples were taken from the 1994 and 1995 positron-proton nominal vertex running. A four track selection was made to identify ψ' candidates from the decay: $\psi' \rightarrow J/\psi (\rightarrow l^+l^-)\pi^+\pi^-$, where all four tracks were required to pass the track cuts defined in section 4.6. From this sample, events were selected with two identified leptons of opposite charge, and where the two remaining tracks were also of opposite charge. Wrong charge combinations were rejected, and the mass of the dilepton system was required to be within 300 MeV of the nominal J/ψ mass. This ‘loose’ selection was used to identify a signal for ψ' events, and further cuts were then applied to obtain a final ‘tight’ selection which was used to calculate the cross section.

The remaining cuts which define the ‘tight’ selection, used for the cross section measurement, are as follows. Where the J/ψ candidate decayed into electrons, only events from subtriggers 52 and 54 were selected, and for decays into muons, events from subtriggers 18, 19 and 22 were selected. Further angular cuts were placed on the tracks, requiring them to be in the central part of the detector, $20 < \theta < 165^\circ$. Finally, in order to select photoproduction events, a cut was made to reject events where a scattered positron was detected in the BEMC (in 1994 data) or in the SPACAL (in 1995 data). This limited the sample to the region where $Q^2 < 4 \text{ GeV}^2$ in the 1994 data, and $Q^2 < 1.2 \text{ GeV}^2$ in the 1995 data (see section 4.8). The events were required to have a centre of mass energy of the photon - proton system of $40 < W_{\gamma p} < 160 \text{ GeV}$ for events with muons in the decay, and $40 < W_{\gamma p} < 120 \text{ GeV}$ for events with electrons as the decay products. This corresponds to the region in W in which the acceptance is good.

The mass difference $\Delta M = M(l^+l^-\pi^+\pi^-) - M(l^+l^-)$ was calculated, and events with ΔM within 60 MeV of the nominal difference in mass between the ψ' and the J/ψ (590 MeV) were defined to be ψ' candidates. The mass difference is a more useful variable to define a ψ' candidate due to the significantly better resolution in the ΔM distribution, than the invariant mass distribution of all four particles. The natural widths of the resonances are of the order of a few keV and are therefore insignificant in comparison to the reconstruction resolution.

An event display picture of a typical event satisfying this selection (in the electron channel) is shown in figure 4.12. The electrons can be clearly seen as tracks linked to clusters in the electromagnetic section of the LAr calorimeter, with no energy in the hadronic section behind. The low momentum pions can be seen as the tracks that bend significantly in the

magnetic field. In addition, the event appears to be elastic because there is no observable activity in the forward parts of the detector.

4.7.2 Two track sample

A two track selection was made to identify ψ' candidates from the direct decay: $\psi' \rightarrow l^+l^-$. Events were selected with exactly two identified leptons, and no other tracks in the detector. In order to obtain as clean a sample as possible, only events where the two tracks were in the central part of the detector were accepted, *ie.* $20 < \theta < 160^\circ$. The same trigger selections were made as in the four track sample, and events where a scattered positron was observed were also rejected.

Background events from cosmic muons were rejected by demanding that the opening angle between the two muon be less than 170° . Two other possible sources of background to the two track sample are events from the high mass tail of the J/ψ mass peak which may fall into the ψ' mass region, and l^+l^- QED pair production. The number of background events in the signal region was estimated by fitting the background around the resonance.

There is significant background to the two track sample, which leads to large uncertainties in the final cross section. The four track sample, however, gives a very clean signal with negligible background. The motivation behind studying the two track sample is that it provides a cross check on the cross section calculated using the four track sample.

4.8 Kinematic Acceptance

The kinematic region in which the measurement is made results from the geometric acceptance of the main detectors and the selection criteria used to define ψ' candidate events. The requirement that precisely four (or two) tracks are observed in the detector ensures that the sample is quasi-elastic, *ie.* $z > 0.95$ (see figures 4.13 and 4.14). The sample is not purely elastic, as it includes some proton dissociative events, which may appear to be elastic when the proton remnant goes down the beam pipe undetected. Some of the forward detectors may be used to tag these type of events by looking at the level of activity from secondary scattering of proton dissociation particles, but no attempts were made in this analysis to separate the purely elastic from proton dissociative events because of the limited statistics.

The range in $W_{\gamma p}$ over which the measurement was made is a result of the geometric

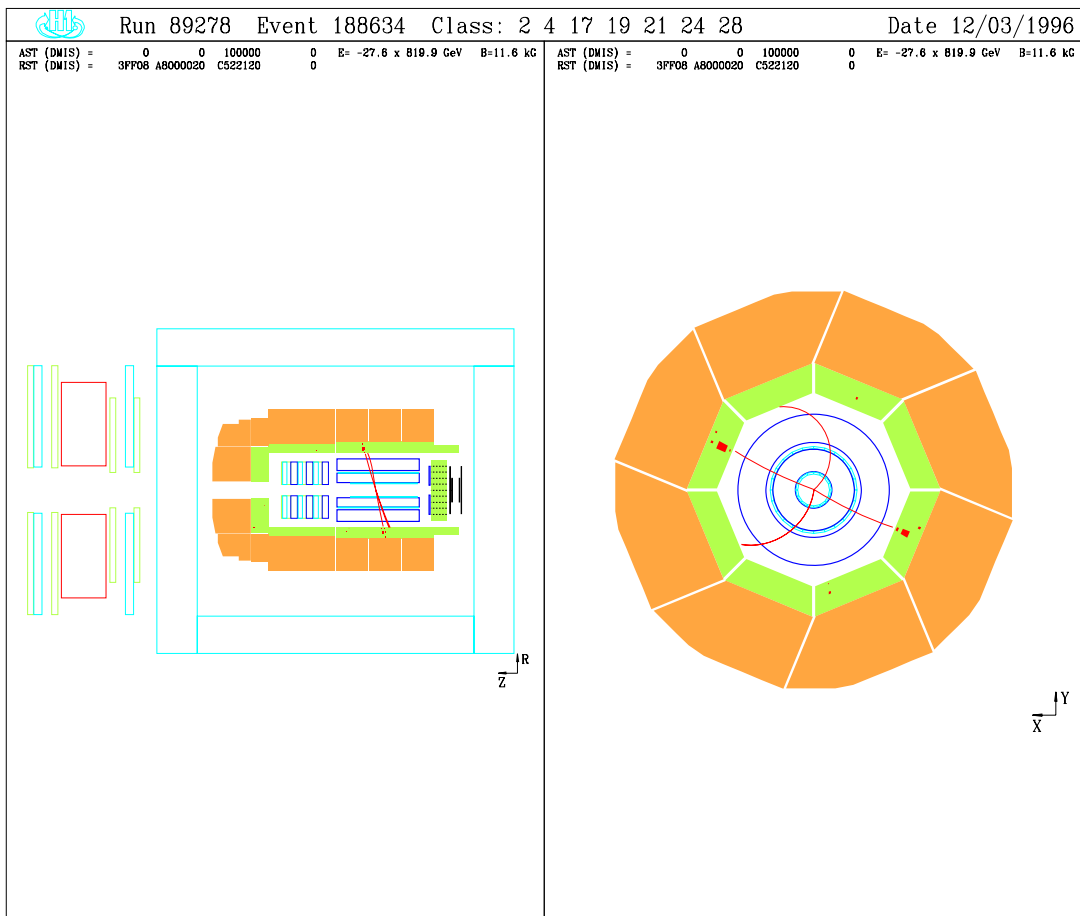


Figure 4.12: Candidate event for an elastic ψ' decaying to two electrons and two pions

acceptance of the detector. Figures 4.13 and 4.14 show the region of acceptance in $W_{\gamma p}$ for the electron and muon channels. The larger range in the muon channel is due to the fact that the muons are detected in both the instrumented iron and in the LAr calorimeter, whereas electrons are identified in the calorimeter only. This means that the angular acceptance for muons is larger in the backward direction, and hence there is a wider accessible region in W in the muon channel. Cuts are made in the analysis around the region in W where the acceptance is approximately flat.

The acceptance in Q^2 is determined by the requirement that no scattered positron should be observed. Due to the different detectors used to detect the positron in 1994 and 1995 (BEMC and SPACAL respectively), this led to different acceptances in Q^2 in the 1994 and 1995 data. Figure 4.15 shows the acceptance in Q^2 in 1995.

To summarise, the kinematic acceptance region is given by:

- $40 < W < 120$ GeV (Electron channel)
- $40 < W < 160$ GeV (Muon channel)
- $z > 0.95$
- $Q^2 < 4.0$ GeV² (1994)
- $Q^2 < 1.2$ GeV² (1995)

The measured cross sections presented in the following chapter are integrated over these regions.

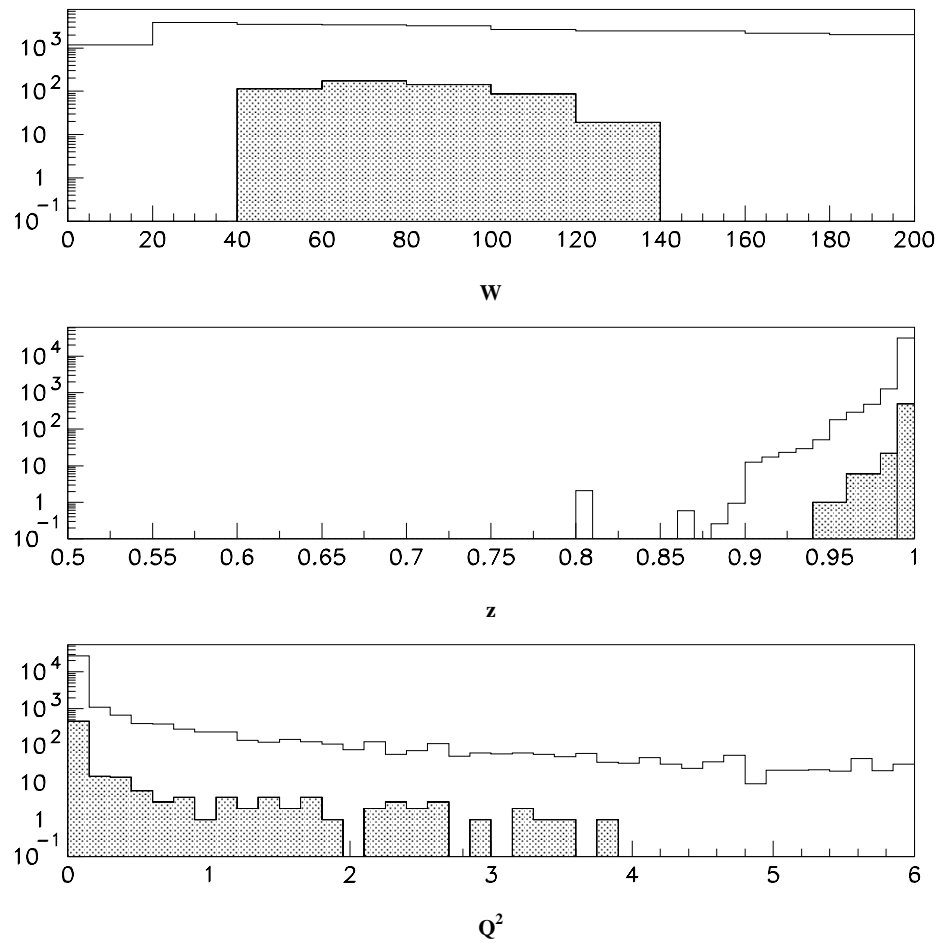


Figure 4.13: Acceptance in W , Q^2 and z (electron channel). The open histogram shows the generated values (from the DIFFVM MC, using a mixture of elastic and proton dissociative events), and the shaded histogram shows those events passing the analysis cuts. (All cuts were applied except for that on the value of W).

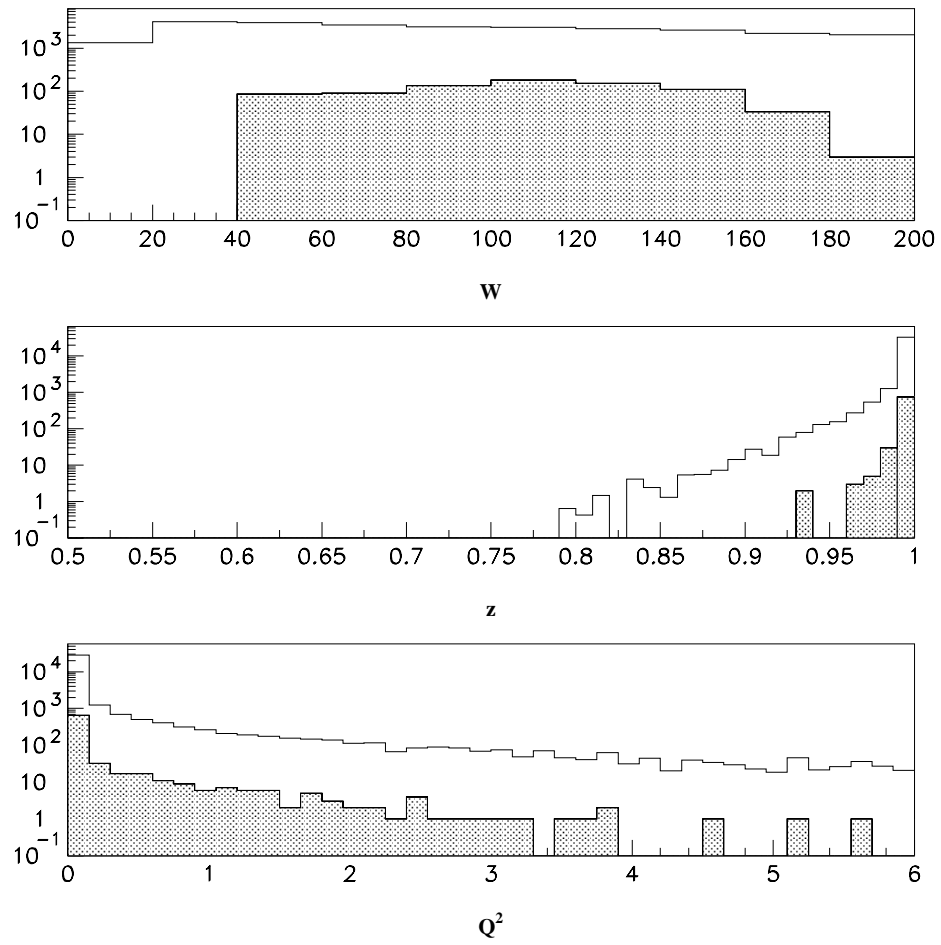


Figure 4.14: Acceptance in W , Q^2 and z (muon channel). The open histogram shows the generated values, and the shaded histogram shows those events passing the analysis cuts. (All cuts were applied except for that on the value of W).

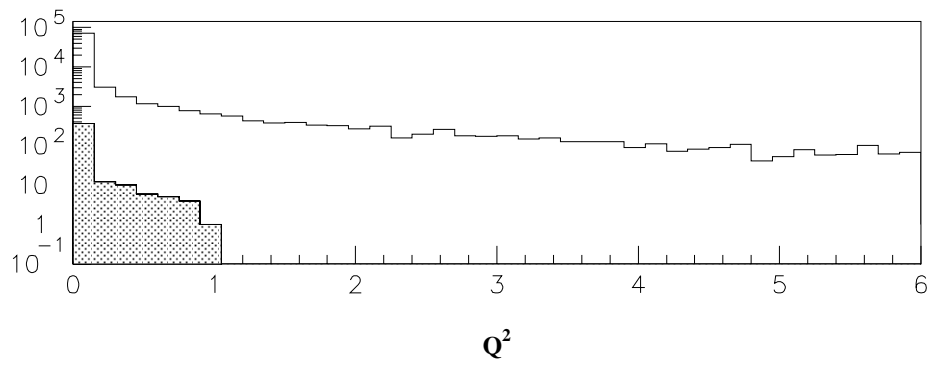


Figure 4.15: Acceptance in Q^2 in the 1995 data. The open histogram shows the generated values, and the shaded histogram shows those events passing the analysis cuts.

Chapter 5

Measurement of Cross-Sections

5.1 Signals

For the four track selection described in section 4.7.1, clear signals with little or no background in the signal region were observed in both the electron and muon channels in 1994 and 1995 data. These are shown in figures 5.1 and 5.3. The peaks in the mass difference distribution lie at approximately 0.6 GeV (the nominal mass difference between the J/ψ and the ψ' is at 0.589 GeV). The ‘tight’ and ‘loose’ selections shown in these figures are described in section 4.7.1. The invariant mass distributions of the two lepton system and of all four tracks are shown in figures 5.2 and 5.4 from the 1994 and 1995 data respectively. For these distributions, both the electron and muon channels are shown together. The number of events in each channel are shown in table 5.1. A signal was also

	$e^+e^-\pi^+\pi^-$	$\mu^+\mu^-\pi^+\pi^-$
1994	5	10
1995	4	8

Table 5.1: Table showing the number of ψ' candidates from the two four track channels in the 1994 and 1995 data. The number of events refers only to events with a value of ΔM that is within 60 MeV of the nominal mass difference.

observed in the channel where the ψ' decays directly to two leptons (see figures 5.5 and 5.6). The fact that the peak at approximately 3.7 GeV is considerably smaller than the J/ψ peak, is not only due to the smaller cross section, but also the fact that branching ratio to leptons is approximately 12 – 15% that of the J/ψ . However, especially when the e^+e^- and $\mu^+\mu^-$ channels are considered together, an enhancement is clearly visible in the region of the ψ' mass.

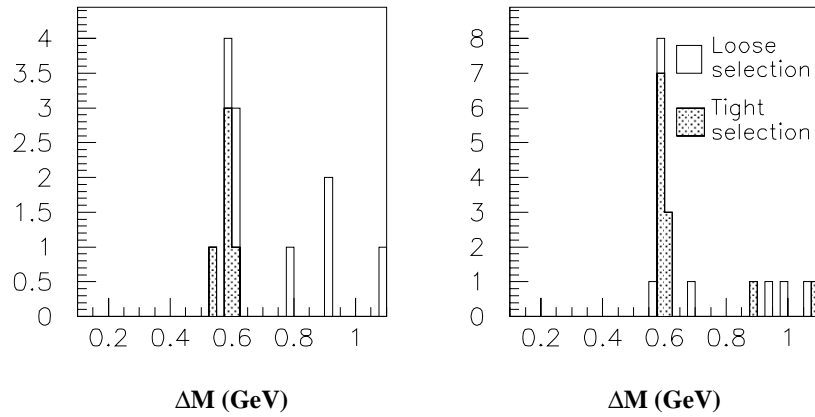


Figure 5.1: ψ' signal from the channel $\psi' \rightarrow J/\psi(\rightarrow l^+l^-)\pi^+\pi^-$ in the 1994 data. The ΔM distribution is shown, where $\Delta M = M(l^+l^-\pi^+\pi^-) - M(l^+l^-)$. The left hand plot shows the channel where the J/ψ decays to electrons, and the right hand plot shows the decay to muons.

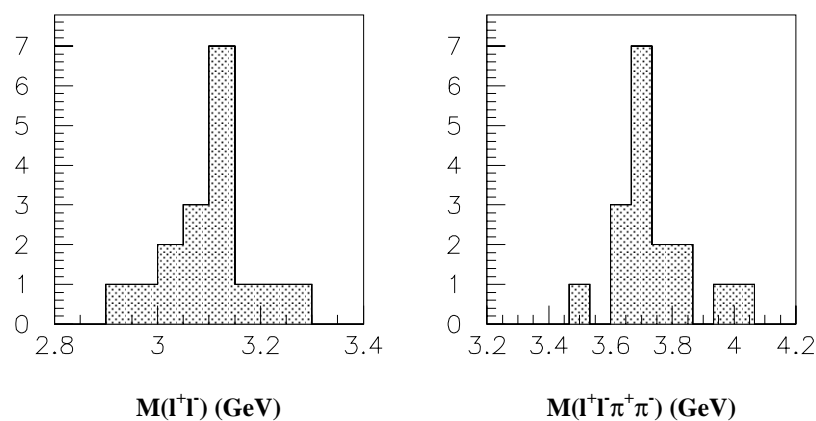


Figure 5.2: Invariant mass distributions for those events passing the tight selection in the 1994 data. The left hand plot shows the invariant mass of the two tracks identified as leptons, and the right hand plot is the mass of the four track system. In these two plots, the electron and muon channels are shown together.

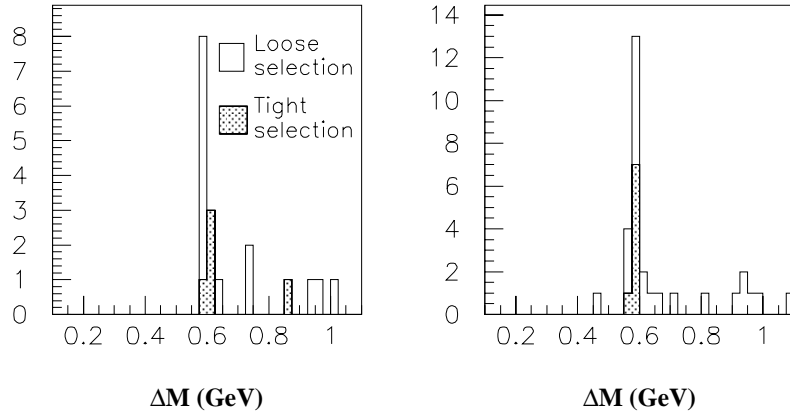


Figure 5.3: ψ' signal from the channel $\psi' \rightarrow J/\psi(\rightarrow l^+l^-)\pi^+\pi^-$ in the 1995 data. The ΔM distribution is shown, where $\Delta M = M(l^+l^-\pi^+\pi^-) - M(l^+l^-)$. The left hand plot shows the channel where the J/ψ decays to electrons, and the right hand plot shows the decay to muons.

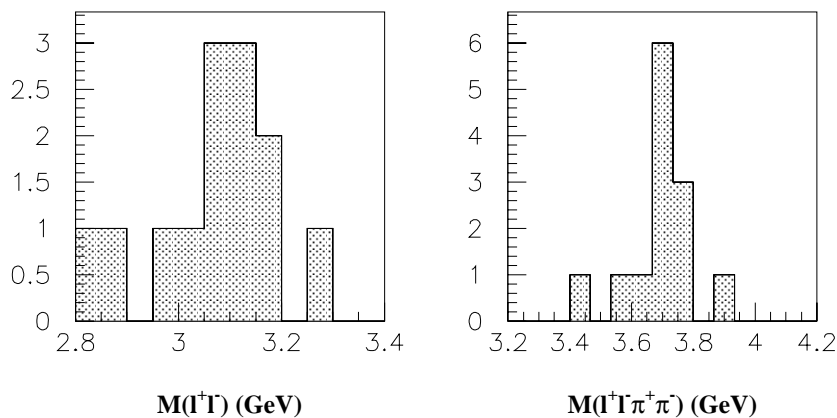


Figure 5.4: Invariant mass distributions for those events passing the tight selection in the 1995 data. The left hand plot shows the invariant mass of the two tracks identified as leptons, and the right hand plot is the mass of the four track system. In these plots, the electron and muon channels are shown together.

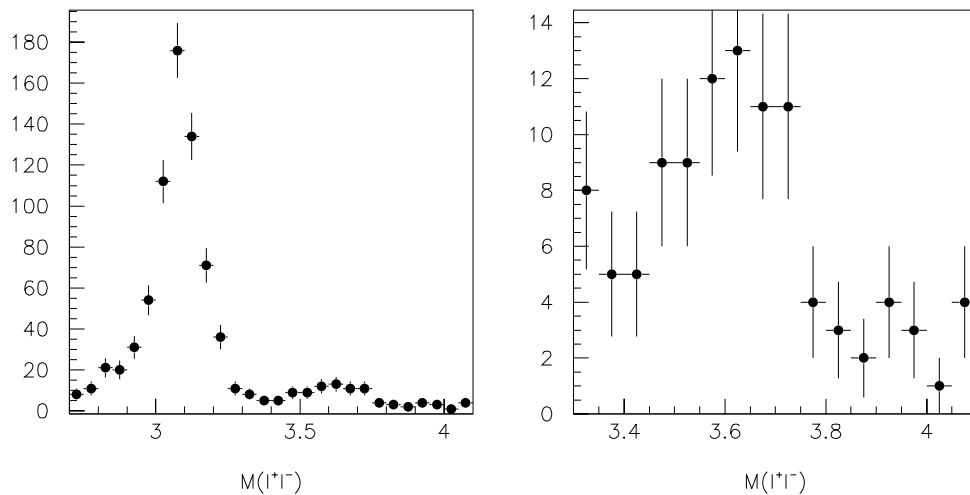


Figure 5.5: ψ' signal from the channel $\psi' \rightarrow l^+l^-$ in the 1994 data. The left hand plot shows the invariant mass distribution from the two track sample, displaying the large J/ψ signal, and the right hand plot is the same distribution, but expanded to show just the region between 3.3 and 4.1 GeV.

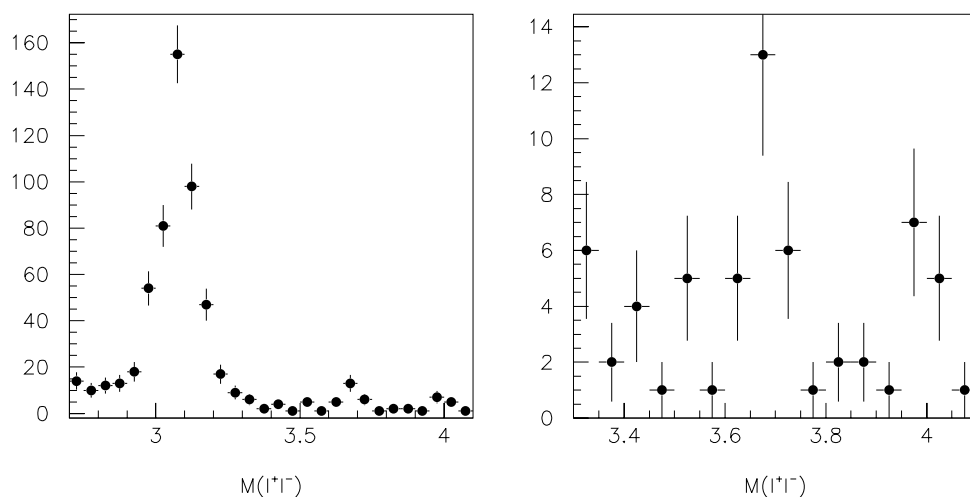


Figure 5.6: ψ' signal from the channel $\psi' \rightarrow l^+l^-$ in the 1995 data. The left hand plot shows the invariant mass distribution from the two track sample, displaying the large J/ψ signal, and the right hand plot is the same distribution, but expanded to show just the region between 3.3 and 4.1 GeV.

5.2 Acceptance determination

The acceptance for ψ' events, decaying through each channel studied in the kinematic region of the measurement was determined using the DIFFVM Monte Carlo (see section 4.3.1). The acceptance is the fraction of generated events which are reconstructed as ψ' events and pass all the selection cuts defined in sections 4.7.1 and 4.7.2. Included in this acceptance is the geometric acceptance of the detector, the triggering and reconstruction efficiencies, and the acceptance of the analysis cuts. To ensure that an accurate determination of the overall efficiency is made, it is important that the Monte Carlo models the data well in every respect. The agreement between the various efficiencies evaluated from data and MC was shown in the previous chapter. Any discrepancies are included in the systematic errors (see section 5.3). Figures 5.7 and 5.8 show comparisons between data and MC for distributions of the ψ' and of the decay products (for the decay: $\psi' \rightarrow J/\psi(\rightarrow l^+l^-)\pi^+\pi^-$) from 1994 and 1995 data respectively.

In DIFFVM the distribution of the three particles (J/ψ and two pions) from the decay of the ψ' is generated simply according to phase space. However, data from previous experiments [69][70] show a quite different mass spectrum for the two pion system, and the MC was accordingly weighted by a factor

$$(M(\pi\pi)^2 - 4m_\pi^2)^2,$$

where $M(\pi\pi)$ is the invariant mass of the dipion system, and m_π is the mass of a pion. Despite the low statistics, the data clearly favour the reweighted mass distribution (see figures 5.7 and 5.8).

The acceptance calculation also took account of the effects of the trigger prescales, which are included as a trigger inefficiency. Also, events which it would not have been possible to trigger on or reconstruct due to the H.V. status of various parts of the detector are accounted for as an inefficiency in the overall acceptance.

In the 1994 data, the overall acceptances for the four track samples were 7.1% and 7.2% for the electron and muon channels respectively. The corresponding acceptances in 1995 were 2.3% and 3.8%. The low values for these acceptances are due in part to the demand that all four tracks must lie in the central region of the detector, and the trigger efficiencies. The main inefficiency of the other analysis cuts is due to the p_T cut on the pions from the ψ' decay, which tend to be very soft. The comparatively lower values for 1995 are a result of the high trigger prescales in place for much of the data taking period. These prescales give a very low trigger efficiency. The different components of the overall acceptance

are shown in table 5.2. The combined acceptance for 1994 and 1995 for the two track sample was measured using the same MC, and found to be 11.6%. The errors on these acceptances are discussed in some detail in the next section.

Data sample	$e^+e^-\pi^+\pi^-$ 1994	$\mu^+\mu^-\pi^+\pi^-$ 1994	$e^+e^-\pi^+\pi^-$ 1995	$\mu^+\mu^-\pi^+\pi^-$ 1995	Combined 94/95
H.V. corrections	.895	.902	.691	.699	.772
Geometric acceptance	.495	.627	.494	.625	.496
Trigger efficiency	.427	.364	.192	.197	.278
Analysis cuts	.375	.351	.358	.441	.383
Total acceptance	.071	.072	.023	.038	.041

Table 5.2: Acceptances for triggering and reconstructing ψ' events in 1994 and 1995 data

5.3 Systematic Errors

The systematic uncertainty on each measurement has contributions from various sources. Firstly, there is an error on the acceptance due to uncertainties in efficiencies, MC model dependence, and MC statistics.

The systematic uncertainties on the acceptance are as follows.

- In the central tracker the efficiency for track reconstruction rises very sharply from $\sim 0\%$ at $p_T = 80$ MeV to $\sim 97\%$ at $p_T = 120$ MeV, and is then flat for higher p_T tracks [71]. The lepton tracks, which have momenta of typically 1.5 GeV, lie in the region of the maximum efficiency of the central tracker. The pion tracks, however, are very soft, and therefore have larger errors associated with their reconstruction. It was assumed that tracks with $p_T < 0.15$ GeV had an error of $\pm 5\%$ associated with their efficiency, and tracks with $p_T > 0.15$ GeV, an error of $\pm 3\%$. These errors result in an overall systematic uncertainty on the acceptance of 12%.
- A study of the efficiencies of the various subtriggers used in the analysis is presented in section 4.4.1. The resulting uncertainties in the acceptance are shown in table 5.3. The large discrepancy between data and MC for the efficiencies of the track trigger elements *DCRPh-Ta* and *DCRPh-TNeg* in 1994 was accounted for by correcting the efficiency of the MC to the level obtained from the data. The error on the measured efficiency in the data sample was then used to estimate the systematic error. Any further discrepancies between data and MC efficiencies are covered by the systematic errors shown in table 5.3. These systematic errors represent the uncertainty on the overall acceptance as a result of the uncertainty on the trigger

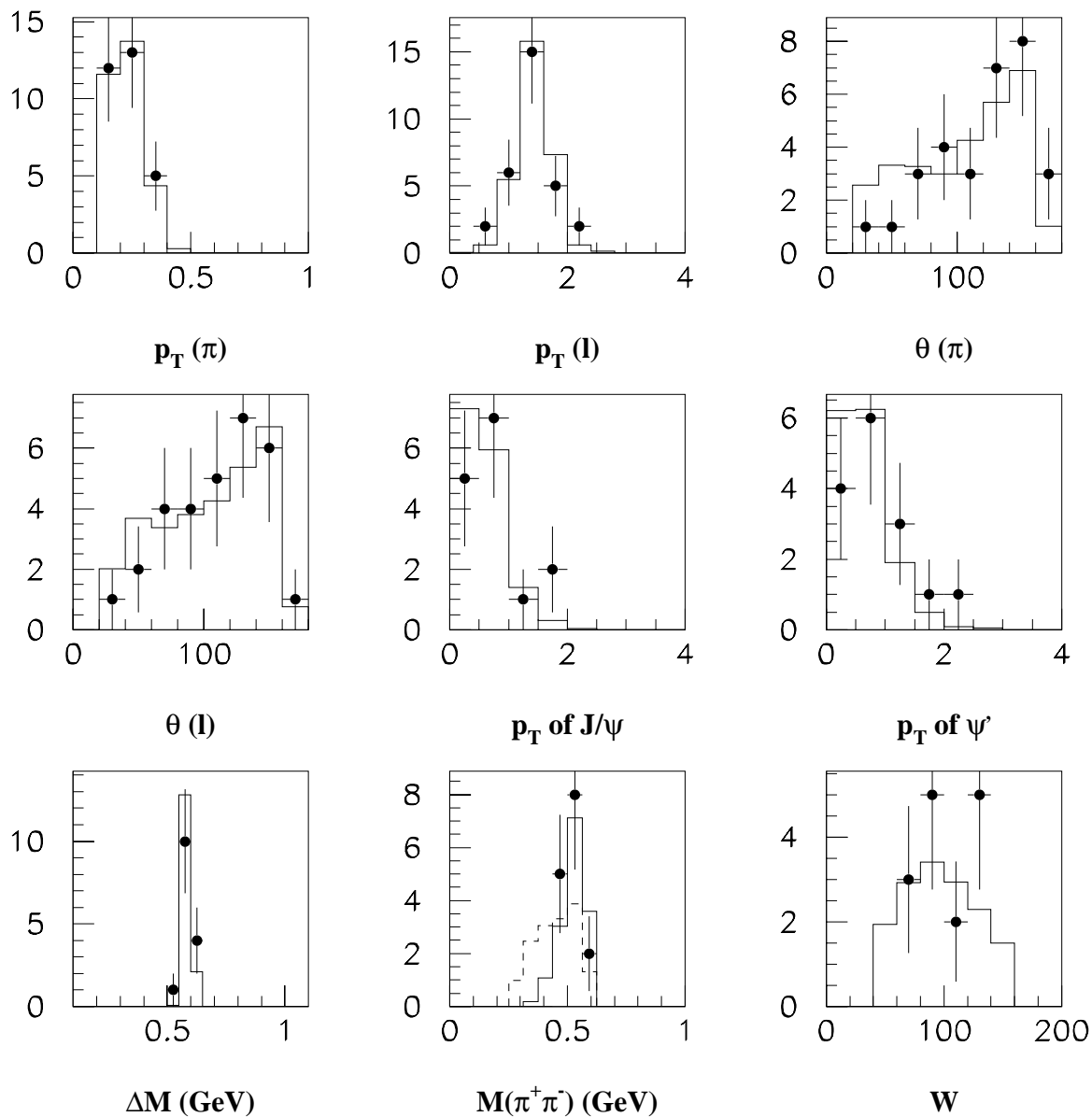


Figure 5.7: The upper six plots show a comparison between data and MC for p_T and θ distributions for the ψ' and for the decay particles in the event. Data is from 1994 and is shown as points and the solid histogram is MC. The Lower three plots show the mass difference, the dipion mass distributions, and the W distribution. For the invariant mass distribution of the dipion system, the dashed line is the MC before reweighting and the line is the weighted MC (see text).

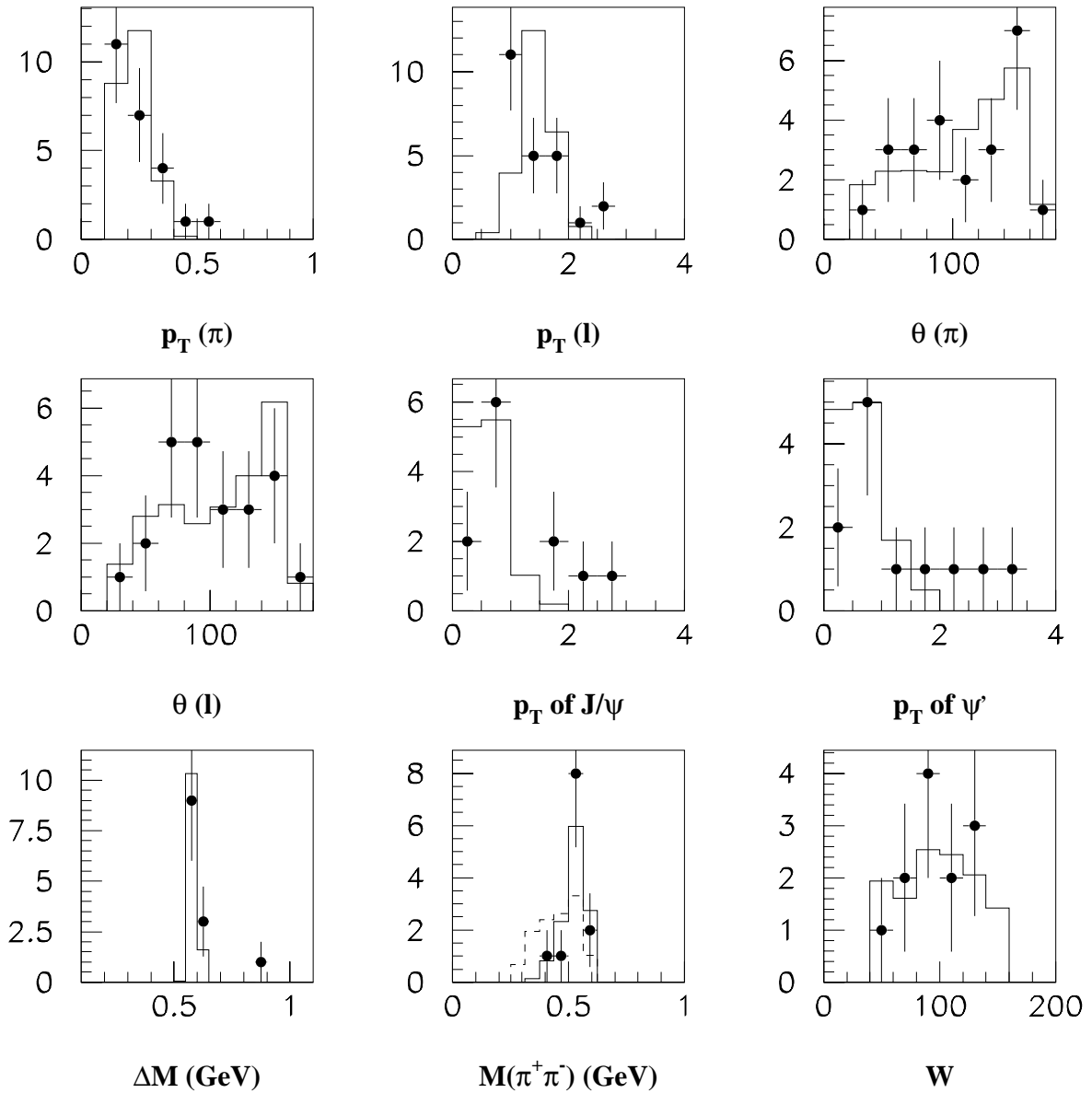


Figure 5.8: Comparison between data and MC of various distributions of the ψ' and the decay particles in the event, where the data is taken from 1995. Data is shown as points and the solid histogram is MC. The invariant mass distribution of the dipion system shows the MC before reweighting as the dashed histogram, and the solid histogram is the weighted MC.

element efficiency. The systematic errors may therefore be smaller than the error on the efficiency, if, for example, the trigger element is not responsible for triggering a large fraction of the final event sample.

Trigger element	Systematic error on acceptance (%)				Combined (94/95)
	$e^+e^-\pi^+\pi^-$ (1994)	$\mu^+\mu^-\pi^+\pi^-$ (1994)	$e^+e^-\pi^+\pi^-$ (1995)	$\mu^+\mu^-\pi^+\pi^-$ (1995)	
<i>Mu_BEC</i>	—	1	—	1	1
<i>Mu_FOEC</i>	—	1	—	$\ll 1$	1
<i>Mu_Bar</i>	—	2	—	1	1
<i>LAr_BR</i>	4	—	2	—	2
<i>Topo_BR</i>	1	—	3	—	1
<i>zVtx_Cls</i>	5	—	5	—	2
<i>zVtx_Small</i>	—	3	—	4	2
<i>DCRPh-Ta</i>	1	1	2	4	2
<i>DCRPh-TNeg</i>	1	—	1	—	1
<i>LAr_IF</i>	2	—	3	—	1
Veto Elements	4	4	4	4	4
Total	8	6	8	7	6

Table 5.3: Contributions to systematic error from individual trigger elements

- A study of the lepton identification efficiencies was presented in section 4.5.3. Due to inherent uncertainties in the method used to find the identification efficiency directly from data, *eg.* background events in the sample chosen from the J/ψ peak, it was not clear that the data gave the best estimate of the efficiency. The agreement between data and MC was reasonably good in most cases, and any discrepancies were accounted for in the measurement by taking the difference between the efficiencies as estimated from data and MC as the error on the efficiency measured from MC. The resulting systematic errors in the 1994(1995) data due to uncertainties in the lepton identification efficiency were 4%(7%) and 9%(7%) for the electron and muon channels respectively, and 6% for the error on the acceptance for the combined measurement.
- The variable parameters in the DIFFVM MC are described in section 4.3.1. The MC model dependent errors were evaluated by varying these parameters and calculating the effect this had on the acceptance. The parameter ϵ which describes the W dependence of the cross section was varied between 2.0 and 2.5 and the b -slope parameter was varied by ± 1.0 . The cross section dependence on M_X was described by $\frac{1}{M_X^k}$, and k was varied between 0.20 and 0.25 ($k = 2.2 \pm 0.2$ was measured in [72]). Finally, the ratio of purely elastic events to proton dissociative events was varied by $\pm 20\%$. These errors were added in quadrature and gave the model dependent errors of 5%(4%) in the electron channel and 6%(7%) in the muon channel in the 1994(1995) data. The error on the acceptance for the combined measurement was found to be 5%.

The background for the four-prong sample is estimated from wrong charge combinations of pions and found to be consistent with zero in the signal region. The remaining uncertainty in the number of events in the signal region comes only from migration of events from outside the kinematic region in which the measurement is made. No specific cuts are made in the data sample on Q^2 or z , as the cuts on the scattered electron and on the number of tracks are assumed to restrict these kinematic variables, and the cross section is expected to peak sharply as $Q^2 \rightarrow 0$ and $z \rightarrow 1$. The number of events which may still pass all the analysis cuts and have $Q^2 > 4 \text{ GeV}^2$ ($Q^2 > 1.2 \text{ GeV}^2$ in 1995) or $z < 0.95$ is estimated from MC, and is very small. The background in the two track sample is estimated by fitting the dilepton invariant mass distribution to a Gaussian with a linear background. The number of events is then taken as the area under the Gaussian, with a systematic error associated with the uncertainty in the background of $\pm 20\%$. This error is estimated by changing the parameterisation of the background from a linear fit to a second degree polynomial, by varying the mass range over which the background is fitted and by varying the binning. The number of background events in the two track sample due to migration of events from outside the kinematic region is assumed to be negligible compared to the uncertainty in the total background.

Other systematic errors arise from uncertainty in the total integrated luminosity and in the different branching ratios. The systematic errors for the four track sample are summarised in table 5.4, and those for the two track sample in table 5.5. The total systematic error given at the bottom of each column is obtained by summing the contributing errors in quadrature.

The combined measurement of the four track sample is evaluated by calculating the overall acceptance for both channels over the two years data, weighting the Monte Carlos for each year proportionally to the integrated luminosity for that year. The systematic errors are then calculated by the method used for each channel individually, *ie.* by finding the effect on the overall acceptance of the individual uncertainties in efficiencies *etc.*

5.4 Cross section measurements

The measured cross section is determined from the number of reconstructed events (N_{event}), the overall acceptance for detecting and reconstructing such events (ϵ), the total integrated luminosity (\mathcal{L}) and the branching ratio ($B.R.$) of the decay channel used to identify the process.

$$\sigma = \frac{N_{event}}{\mathcal{L} \times \epsilon \times B.R.} \quad (5.1)$$

Systematic uncertainty (%) in:	Data Sample				
	$e^+e^-\pi^+\pi^-$ (1994)	$\mu^+\mu^-\pi^+\pi^-$ (1994)	$e^+e^-\pi^+\pi^-$ (1995)	$\mu^+\mu^-\pi^+\pi^-$ (1995)	Combined (94/95)
Track reconstruction efficiency	12	12	12	12	12
Lepton identification efficiency	4	9	7	7	6
Trigger efficiency	8	6	8	7	6
Model dependence	5	6	4	7	5
MC Statistics	5	5	12	8	4
Migration of events from outside kinematic region	< 1	1	3	2	1
Luminosity	1.5	1.5	1.2	1.2	2
$B.R.(\psi' \rightarrow J/\psi\pi^+\pi^-)$	8	8	8	8	8
$B.R.(J/\psi \rightarrow l^+l^-)$	3	4	3	4	2.5
Total Systematic Error	19	19	22	21	18

Table 5.4: *Systematic errors for the four data samples of four track events from the 1994 and 1995 data, together with the errors for the combined result.*

The number of events in the signal from the four track sample is simply given by the number of candidate events which had a reconstructed mass difference (ΔM) within 60 MeV of the nominal mass difference between the J/ψ and the ψ' . The reconstruction of four track events gives a very clean sample, and the background was estimated to be zero in the signal region.

The branching ratios used to calculate the cross section for each channel were shown in table 4.1, and the overall acceptances used in the measurement are shown in table 5.2.

5.4.1 Results from the four track sample

The cross sections for the process $ep \rightarrow \psi'X$ were measured in each decay channel from the four track sample, for the region $z > 0.95$, and $Q^2 < 4 \text{ GeV}^2$, ($Q^2 < 1.2 \text{ GeV}^2$ in 1995). The measurement was made from a total integrated luminosity of 3.02 pb^{-1} from 1994, and 5.19 pb^{-1} from 1995.

Firstly, the channel where the J/ψ decays to electrons gave for the region $40 < W_{\gamma p} < 120 \text{ GeV}$,

$$\sigma(ep \rightarrow \psi'X) = 1.2 \pm 0.5(\text{stat}) \pm 0.2(\text{syst}) \text{ nb}, \quad (5.2)$$

from the 1994 data, and

$$\sigma(ep \rightarrow \psi'X) = 1.7 \pm 0.9(\text{stat}) \pm 0.4(\text{syst}) \text{ nb}, \quad (5.3)$$

Systematic uncertainty in (%)	$\psi' \rightarrow l^+l^-$ 94/95
Track reconstruction efficiency	10
Lepton identification efficiency	6
Trigger efficiency	6
Model dependence	3
MC Statistics	2
Background	20
Luminosity	2
$B.R.(\psi' \rightarrow l^+l^-)$	12
Total systematic error	27

Table 5.5: Systematic errors for the two track data sample. Both years are combined.

from the 1995 data.

The channel where the J/ψ decays to muons gave for the region $40 < W_{\gamma p} < 160$ GeV,

$$\sigma(ep \rightarrow \psi'X) = 2.4 \pm 0.7(stat) \pm 0.4(syst) \text{ nb}, \quad (5.4)$$

from the 1994 data, and

$$\sigma(ep \rightarrow \psi'X) = 2.1 \pm 0.7(stat) \pm 0.4(syst) \text{ nb}, \quad (5.5)$$

from the 1995 data.

5.4.2 Photon Flux

The ep cross sections (σ_{ep}) shown above are related to the photoproduction cross sections ($\sigma_{\gamma p}$), at $Q^2 = 0$, by

$$\sigma_{ep} = \int \int dy dQ^2 \mathcal{F}_{\gamma/e}^T(y, Q^2) \sigma_{\gamma^*p}(y, Q^2), \quad (5.6)$$

where the photon flux, $\mathcal{F}_{\gamma/e}^T(y, Q^2)$, is given by the Weizsäcker-Williams approximation [73]

$$\mathcal{F}^T(y, Q^2) = \frac{\alpha}{2\pi} \frac{1}{yQ^2} \left\{ 1 + (1-y)^2 - 2(1-y) \frac{Q_{min}^2}{Q^2} \right\}, \quad (5.7)$$

where Q_{min}^2 is related to y and the electron mass, m_e , by

$$Q_{min}^2 = \frac{m_e^2 y}{1-y}. \quad (5.8)$$

The dependence on Q^2 and y of the cross section can be parameterised in the following way

$$\sigma_{\gamma^*p}(y, Q^2) = \sigma(W_0, Q^2 = 0) \left(\frac{W}{W_0} \right)^{4\epsilon} \frac{1}{(1 + Q^2/M_V^2)^2}. \quad (5.9)$$

The cross sections σ_{ep} and $\sigma_{\gamma p}$ are then related by the simple equation

$$\sigma_{ep} = \sigma_{\gamma p}(W_0)\Phi_{\gamma/e}, \quad (5.10)$$

where the ‘flux factor’, $\Phi_{\gamma/e}$ is given by the integration over y and Q^2

$$\Phi_{\gamma/e} = \int \int dy dQ^2 \mathcal{F}^T(y, Q^2) \left(\frac{W}{W_0} \right)^{4\epsilon} \frac{1}{(1 + Q^2/M_V^2)^2}, \quad (5.11)$$

where M_V is the mass of the vector meson. The integration in Q^2 is done between Q_{min}^2 (equation 5.8) and the upper limit on Q^2 , namely 4 GeV^2 in 1994 and 1.2 GeV^2 in 1995. The limits on the y integral come from the region in W over which the measurement was made since W and y are simply related by the centre of mass energy, \sqrt{s} , at $Q^2 = 0$ according to

$$W^2 \simeq ys. \quad (5.12)$$

The flux factors were calculated over the different ranges in W and Q^2 for the two different channels in the 1994 and 1995 data, to give the photoproduction cross sections at $Q^2 = 0$ and $W_{\gamma p} = 80 \text{ GeV}$. The ep cross sections, flux factors and photoproduction cross sections are summarised in table 5.4.2. An additional systematic error due to uncertainties in the photon flux calculation is included in the errors on the photoproduction cross sections. This error was estimated by varying the value of ϵ , the W dependence of the cross section, from 0.15 to 0.225, and was found to be 2% in the muon channel, and 3% in the electron channel.

Data sample	$e^+e^-\pi^+\pi^-$ (1994)	$\mu^+\mu^-\pi^+\pi^-$ (1994)	$e^+e^-\pi^+\pi^-$ (1995)	$\mu^+\mu^-\pi^+\pi^-$ (1995)
$W_{\gamma p}$ (GeV)	$40 < W < 120$	$40 < W < 160$	$40 < W < 120$	$40 < W < 160$
Q^2 (GeV^2)	$Q^2 < 4.0$	$Q^2 < 4.0$	$Q^2 < 1.2$	$Q^2 < 1.2$
$\sigma(ep \rightarrow \psi' X)$	$1.2 \pm 0.5 \pm 0.2$	$2.4 \pm 0.7 \pm 0.4$	$1.7 \pm 0.9 \pm 0.4$	$2.1 \pm 0.7 \pm 0.4$
$\Phi_{\gamma/e}$	0.0918	0.1187	0.0879	0.1135
$\sigma(\gamma p \rightarrow \psi' X)$	$13 \pm 6 \pm 2$	$20 \pm 6 \pm 4$	$20 \pm 10 \pm 4$	$19 \pm 7 \pm 4$

Table 5.6: Summary of ep and photoproduction cross sections for the four data samples, where the first error shown is statistical and the second systematic. The ranges of W and Q^2 over which the ep cross section measurement is made are shown. $\Phi_{\gamma/e}$ is the photon flux integrated over Q^2 and $W_{\gamma p}$. The photoproduction cross sections are at a fixed $W_{\gamma p}$ of 80 GeV .

5.4.3 Combined Cross section Result

The combined ep cross section for both four track channels from both years was measured to be

$$\sigma(ep \rightarrow \psi'X) = 2.1 \pm 0.4(stat) \pm 0.4(syst) \text{ nb}, \quad (5.13)$$

for the region $40 < W < 160 \text{ GeV}$, $z > 0.95$ and $Q^2 < 4 \text{ GeV}^2$. This was converted to a γp cross section at $W = 80 \text{ GeV}$ and $Q^2 = 0$, giving

$$\sigma(\gamma p \rightarrow \psi'X) = 18 \pm 3(stat) \pm 3(syst) \text{ nb}. \quad (5.14)$$

This can be compared with the equivalent cross section for J/ψ production of $119.5 \pm 11.2 \pm 12.0 \text{ nb}$ [52] to give a ratio

$$\frac{\sigma_{\gamma p}(\psi')}{\sigma_{\gamma p}(J/\psi)} = 0.15 \pm 0.03(stat) \pm 0.02(syst). \quad (5.15)$$

The systematic error in the above ratio is estimated from the systematic error on the cross section for ψ' production, but neglecting factors which are correlated in the ψ' and J/ψ cross section calculations. Correlated systematic errors include uncertainties in trigger efficiencies (the same triggers were used in both cases) and uncertainties in lepton identification efficiency. The total error on the ratio is dominated by the statistical error.

5.4.4 Results from the two track sample

The cross section for the photoproduction of ψ' mesons was also measured from a two track sample of data, selected from data taken over both 1994 and 1995 with a total integrated luminosity of 8.22 nb^{-1} . The number of events was estimated by fitting the signal to a Gaussian with a linear background (see figure 5.9), and was found to be 41 ± 8 . The mass of the ψ' was left free in the fit; the mean of the Gaussian fitted to the data was $3.66 \pm 0.02 \text{ GeV}$ (cf. the nominal mass of the ψ' of 3.686 GeV [64]). The cross section was measured over the kinematic region $40 < W < 160 \text{ GeV}$, $Q^2 < 4 \text{ GeV}^2$ and $z > 0.95$.

$$\sigma(ep \rightarrow \psi'X) = 2.6 \pm 0.4(stat) \pm 0.7(syst) \text{ nb}. \quad (5.16)$$

This was converted to a photoproduction cross section at a centre of mass energy of $W_{\gamma p} = 80 \text{ GeV}$, giving

$$\sigma(\gamma p \rightarrow \psi'X) = 23 \pm 4(stat) \pm 6(syst) \text{ nb}. \quad (5.17)$$

The systematic error on this result is large compared to that for the result from the four track sample, and is dominated by the uncertainties on the branching ratio for $\psi' \rightarrow \mu^+ \mu^-$, and on the background. This cross section result is viewed as a cross check on that calculated from the four track sample, and the two results are not combined.

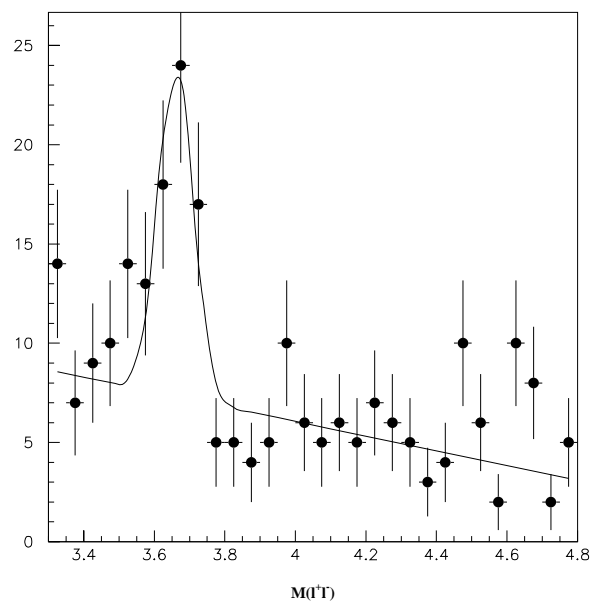


Figure 5.9: *Fit to the two track data sample around the ψ' mass. Both electron and muon channels are included, from data taken in 1994 and 1995. The fit is a Gaussian with a linear background.*

5.5 Comparison with other experiments

The result found for the ratio of the cross sections for the photoproduction of ψ' compared to that for J/ψ is in very good agreement with that measured at previous fixed target experiments. The strong rise of the elastic J/ψ cross section with centre of mass energy is also present for the elastic production of ψ' mesons, if the result from this analysis is compared to the lower energy fixed target experiments. The ratio of the cross sections, however, is totally consistent with a constant value over the energy range covered by the different experiments ($6 < W < 80$ GeV). This is demonstrated in figure 5.10, where the ratio is shown as a function of the centre of mass energy, W .

The different experiments shown in figure 5.10 all measure slightly different cross sections. The earliest measurement of the cross section ratio from SLAC in 1975 [74] used real photons incident on a deuterium target at a centre of mass energy of 6 GeV. The cross sections measured were defined as ‘elastic’, essentially meaning there was no other activity detected apart from the decay products of the J/ψ or ψ' . The ψ' was identified from its decay to a J/ψ and two pions. The ratio of the differential cross sections, $d\sigma/dt$, is given, but this should be the same as the ratio of the t integrated cross sections, provided the

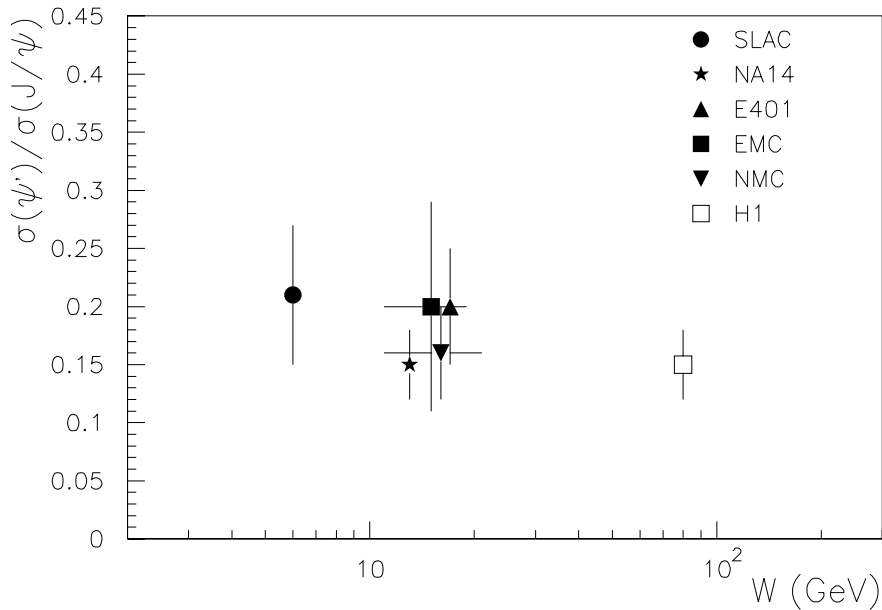


Figure 5.10: Ratio of the cross sections for the photoproduction of J/ψ and ψ' meson as a function of the centre of mass energy, W . The result from this analysis is shown together with those from previous fixed target experiments [74][75][76][77][78]. The ratios from the fixed target experiments have been corrected to account for different values used for the various branching ratios. The error bars shown are statistical only.

b slope (the parameter describing the exponential t distribution) is the same for both ψ' and J/ψ production. The experiment NA14 [75] measured the photoproduction of J/ψ and ψ' from real photons incident on a lithium target at a mean centre of mass energy of 13 GeV. The ratio in this case includes contributions from inelastic ψ production, and was measured using the decay to two muons. The ratio measured at E401 [76], where real photons were incident on a deuterium target at $W = 17$ GeV, has a similar definition of ‘elastic’ to that used at SLAC, *ie.*, no other tracks in the events aside from those due to the decay products of the ψ , which is equivalent to measuring the cross section at high z . The cross section for the photoproduction of ψ' mesons was measured using both the two track and four track decay channels, and a good agreement was obtained between both measurements. The EMC [77] measurement comes from collisions of 250 GeV muons on an iron target. The ratio from this experiment is from cross sections which include not only an inelastic contribution, but also a contribution from DIS events at higher Q^2 . The NMC experiment, an upgraded version of EMC, also reported a result on this ratio [78], for a similar sample of data, in this case from collisions of 280 GeV muons on targets of both tin and carbon. All the ratios from the different experiments were corrected for the

different branching ratios used in the cross section measurements. The errors displayed on figure 5.10 are statistical only.

In order to compare results from different experiments (and consequently from different production mechanisms) for the ratio of ψ' to J/ψ , it is important to separate direct production from other sources of these particles, *ie.* ‘feed down’ from higher mass charmonium states or from b decays. In many experiments, the latter contribution may be ignored due to the small cross section for $b\bar{b}$ production, and the contributions from higher mass charmonium states differs greatly depending on the production mechanism. In the case of diffractive photoproduction, the only two states under consideration are the $J^{PC} = 1^{--}$ J/ψ and ψ' . Charmonium states with these quantum numbers which lie above the mass threshold for $D\bar{D}$ production will obviously not contribute to J/ψ or ψ' production, because of the available strong decay channels. Similarly, J/ψ and ψ' are the only states produced via photon gluon fusion, the dominant mechanism in the case of inelastic photoproduction. The states χ_{c1} and χ_{c2} have sizable branching ratios for their radiative decays to J/ψ , 27.3% and 13.5% respectively, but do not decay to the ψ' , as they are lower in mass, see figure 3.8. At high energies, these states are produced predominantly by gluon gluon fusion, and therefore present a significant background to direct J/ψ hadroproduction.

Many results for the ratio of the cross sections for the production of ψ' compared to J/ψ mesons are available from various fixed target hadroproduction experiments, *eg.* proton or pion beams on nuclear targets. Whilst the mechanisms via which these particles are produced in such collisions may differ radically from those at the photoproduction experiments, the ratios of the resulting cross sections are remarkably consistent, once the feed down from χ states to J/ψ has been taken into account. The ratio of the cross sections appears to have very little dependence on either the nature of the beam or the target [79].

5.6 Summary

Clear signals have been observed for ψ' mesons in H1 in the decay channel $\psi' \rightarrow J/\psi \pi^+ \pi^-$, where the J/ψ decays to both electrons and muons. The γp cross sections for the quasi-elastic photoproduction of ψ' mesons have been measured in both of these channels, at a centre-of-mass energy of 80 GeV, for both 1994 and 1995 data. The four measurements agree well within errors. A clear peak was also observed in the dilepton invariant mass spectrum around the nominal mass of the ψ' , a signal for the decay $\psi' \rightarrow l^+ l^-$. The cross section measurement from this dilepton sample (from 1994 and 1995 data) is in good

agreement with that obtained from the combined four-track sample.

The cross section from the four track sample was measured at a centre-of-mass energy, $W = 80 \text{ GeV}$ to be $\sigma(\gamma p \rightarrow \psi' X) = 18 \pm 3(stat) \pm 3(syst) \text{ nb}$, for the region $z > 0.95$. The equivalent cross section measured from the two track sample was $\sigma(\gamma p \rightarrow \psi' X) = 23 \pm 4(stat) \pm 6(syst) \text{ nb}$. The ratio of the cross sections for production of ψ' to J/ψ was measured to be $0.15 \pm 0.03(stat)$, which is in agreement within errors with values measured for this ratio by lower energy, fixed target experiments. The results are therefore consistent with a fixed value for the ratio, with no dependence on the centre-of-mass energy. This would indicate that the quasi-elastic ψ' photoproduction cross section shows a similar rise with $W_{\gamma p}$ as the J/ψ cross section.

The measured value of the ratio is somewhat below that predicted using a naive vector meson dominance model, but it is in good agreement with the colour dipole prediction of Kopeliovich and Zarkharov. With greater luminosity it may be possible to measure the ratio at higher Q^2 , and test the prediction that it should rise. More accurate photoproduction measurements at a range W values should also be possible, which will extend the study presented here.

References

- [1] M.Breidenbach et al., Phys. Rev. Lett. **23** (1969) 935.
- [2] H1 Collaboration, I.Abt et al., N.I.M. **A386** (1997) 310.
- [3] H1 Collaboration, I.Abt et al., N.I.M. **A386** (1997) 348.
- [4] H1 Collaboration, 'Technical Proposal to Upgrade the Backward Scattering Region of the H1 Detector', (1993)
- [5] B.Andrieu et al., H1 Calorimeter Group, N.I.M. **A336** (1993) 460.
- [6] J.Ban et al., DESY-95-177 (1995) to be published in N.I.M.
- [7] R.D.Appuhn et al., DESY-96-171 to be published in N.I.M.
- [8] T.Nicholls et al., N.I.M. **A374** (1996) 149.
- [9] R.D.Appuhn et al., DESY-95-250 (1995) to be submitted to N.I.M.
- [10] H1 Collaboration, 'Luminosity Measurement in the H1 Experiment at HERA', submitted to XXVIII ICHEP, Warsaw, 1996.
- [11] H.I.Cronstrom et al., H1 Forward Muon Group, N.I.M. **A340** (1994) 304.
- [12] C.Hilton, 'Forward Muon Detection in H1 and Hadronic Energy Flow in Deep Inelastic Scattering' (Doctoral Thesis, Manchester University, 1993)
- [13] L.West. 'How to use the reconstruction code MTREC', internal note (1994).
- [14] J.P.Sutton, 'The H1 Forward Muon Spectrometer at the HERA Collider', (Doctoral Thesis, Manchester University, 1993)
- [15] R.K.Griffiths, 'Drift Chamber Calibration using Laser ionization', (MSc. Thesis, Manchester University, 1994)
- [16] Forward Muon Alignment Measurement Notes 1-5

- [17] A.Mehta, 'Calibration of the Forward Muon Detetector and Determination of the Diffractive Proton Structure Function at H1', (Doctoral Thesis, Manchester University,1994)
- [18] J.P.Sutton, private communication
- [19] R.Feynman, Phys. Rev. Lett **23** (1969) 1415.
- [20] J.Bjorken and E.Paschos, Phys. Rev. **185** (1969) 1975.
- [21] C.Callan, D.Gross, Phys. Lett. **21** (1968) 311.
- [22] V.Gribov et al., Sov. J. Nucl. Phys. **15** (1972) 438;
G.Alterelli, G.Parisi, Nucl. Phys. **B126** (1977) 298.
- [23] H1 Collaboration, S.Aid et al., Nucl. Phys. **B449** (1995) 3.
- [24] H1 Collaboration, 'A Measurement and QCD Analysis of the Proton Structure Function $F_2(x,Q^2)$ at HERA', Nucl.Phys. **B470** (1996) 3.
- [25] BDCMS Collaboration, A.C.Benvenuti et al., Phys.Lett.B223 (1989) 485; CERN preprint CERN-EP/89-06
- [26] NMC Collaboration, M.Arneodo et al., Phys Lett. **B364** (1995) 107.
- [27] T.Regge, Nuovo Cim. **14** (1959) 951;
T.Regge, Nuovo Cim. **18** (1960) 947.
- [28] A.Donnachie and P.V.Landshoff, Nucl. Phys. **B244** (1984) 322.
- [29] H1 Collaboration, S.Aid et al., Z.Phys. **C69** (1995) 27
- [30] CDF Collaboration, F.Abe et al., Phys. Rev. **D50** (1994) 5550.
- [31] H.Abramovich et al., Phys. Lett. **B269** (1991) 465.
- [32] T.Bauer et al., Rev. Mod. Phys. **50** (1978) 261.
- [33] J.J.Sakurai, Ann. Phys. **11** (1960) 1.
- [34] J.J.Sakurai, D.Schildknecht, Phys. Lett. **B40** (1972) 121.
- [35] M.Greco, Nucl. Phys. **63B** (1973) 398.
- [36] H1 Collaboration, T.Ahmed et al., Nucl. Phys. **B445** (1995) 195.
- [37] S.Frixione et al., Phys. Lett. **B348** (1995) 633.

- [38] H1 Collaboration, C. Adloff et al., *Z.Phys.* **C72** (1996) 593.
- [39] EMC Collaboration, J.J.Aubert et al., *Nucl. Phys.* **B213** (1983) 31.
- [40] OPAL Collaboration, CERN-PPE-94/217 (1994);
LEP Collaboration, CERN-PPE-96/017 (1996).
- [41] H1 Collaboration, S.Aid et al., *Nucl. Phys.* **B472** (1996) 32
- [42] Zeus Collaboration, M.Derrick et al., *Phys. Lett.* **B349** 1995 225.
- [43] CIF Collaboration, M.S Atiya et al., *Phys. Rev. Lett.* **43** (1979) 414;
BFP Collaboration, A.R. Clark et al., *Phys. Rev. Lett.* **45** (1980) 682;
SLAC HFP Collaboration, K.Abe et al., *Phys. Rev.* **D30** (1984) 1;
EMC Collaboration, M.Arneodo et al., *Z. Phys.* **C35** (1987) 1;
PEC Collaboration, M.Adamovich et al., *Phys. Lett.* **B187** (1987) 437;
E691 Collaboration, J.C.Anjos et al., *Phys. Rev. Lett.* **65** (1990) 2503;
WA4 Collaboration, D.Aston et al., *Phys. Lett.* **B94** (1980) 113.
- [44] J.J Aubert et al., *Phys. Rev. Lett.* **33** (1974) 1404.
- [45] J.E.Augustin et al., *Phys. Rev. Lett.* **33** (1974) 1406.
- [46] J.E.Augustin et al., *Phys. Rev. Lett.* **33** (1974) 1453.
- [47] S.Glashow, J.Iliopoulos, L.Maiani, *Phys. Rev.* **D2** (1970) 1285.
- [48] E.Eichten et al., *Phys. Rev. Lett.* **34** (1975) 369.
- [49] E760 Collaboration, T.A.Armstrong et al., *Phys. Rev. Lett.* **69** (1992) 2337
- [50] E.L.Berger and D.Jones, *Phys. Rev.* **D23** (1981) 1521.
- [51] M.Cacciari and M.Krämer, DESY-96-005 (1996).
- [52] H1 Collaboration, S.Aid et al., *Nucl. Phys.* **B472** (1996) 3.
- [53] L.D.Landau, *Dokl. Akad. Nauk. USSR* **60** (1948) 207;
L.N.Yang, *Phys. Rev.* **77** (1950) 242.
- [54] G.Schuler, J.Terron, CERN-TH-6403-92, submitted to *Phys. Lett. B*.
- [55] M.G.Ryskin, *Z. Phys.* **C37** 89.
- [56] M.G.Ryskin et al., hep-ph/9511228.
- [57] Zeus Collaboration, M.Derrick et al., *Phys. Lett.* **B350** (1995) 120.

- [58] E687 Collaboration, P.L.Frabetti et al., Phys. Lett. **B316** (1993) 197.
- [59] E401 Collaboration, M.Binkley et al., Phys. Rev. Lett. **48** (1982) 73.
- [60] FTPS Collaboration, B.H.Denby et al., Phys. Rev. Lett. **52** (1984) 795.
- [61] J.Nemchik et al., Phys. Lett. **B374** (1996) 199.
- [62] J.Nemchik et al., Talk given at International Conference on Hadron Structure: High-energy Interactions: Theory and Experiment, Stara Lesna, Slovakia, 12-17 Feb 1996.
- [63] B.Kopeliovich, B.Zakharov, Phys. Rev. **D44** (1991) 3466.
- [64] 'Particles and Fields', Phys.Rev. **D54** (1996) 1-720
- [65] B.List, 'Diffraktive J/ψ -Produktion in Elektron-Proton-Stoessen am Speicherring HERA' (Diploma Thesis, Tech. Univ. Berlin, 1993).
- [66] H1 Note, H1-03-11/89
- [67] T.Carli et al, 'Performance of the H1 LAr Trigger in 1994' (H1-07/95-445)
- [68] T.Jansen, 'Untersuchung diffraktiver J/ψ -Erzeugung bei HERA' (Doctoral Thesis, Hamburg University, 1995)
- [69] T.N.Pham et al., Phys. Lett. **B61** (1976) 183.
- [70] Mark III Collaboration, D.Coffman et al., Phys. Rev. Lett. **68** (1992) 282.
- [71] W.Erdmann, 'Untersuchung der Photoproduktion von D^* Mesonen am ep-Speicherring HERA' (Doctoral Thesis, Institut f. Teilchenphysik, ETH Zürich, 1996).
- [72] CDF Collaboration, F.Abe et al., Phys.Rev. **D50** (1994) 5535.
- [73] C.Weizsäcker, Zeit. Phys. **88** (1934) 612;
E.Williams, Phys. Rev. **45** (1934) 729.
- [74] U.Camerini et al., Phys. Rev. Lett. **38** (1975) 483.
- [75] NA14 Collaboration, R.Barate et al., Z. Phys. **C33** (1987) 505
- [76] M.Binkley et al., Phys. Rev. Lett. **50** (1983) 302.
- [77] European Muon Collaboration, J.J.Aubert et al., Nucl. Phys. **B213** (1983) 1.
- [78] New Muon Collaboration, P.Amaudruz et al., Nucl. Phys. **B371** (1992) 553.
- [79] G.Schuler, CERN-TH-7170/94 (1994), submitted to Phys. Rep.

Acknowledgements

I would like to claim that I did all this on my own with no help from anyone, but unfortunately that would be a dastardly lie. I would therefore like to acknowledge the help and advice of the following people.

Firstly, I would like to thank all the staff at Birmingham, particularly those involved with H1: John Dowell, John Garvey and Ian Kenyon, my supervisor. I would also like to mention the fellow students who started out with me all those years ago: Tim Nicholls, Dave Rigby and Keith Norman, who all managed the double achievement of completing their PhD's before me, and getting married in the process (not to each other I hasten to add). What does this say of me I wonder? Not only on the shelf, but past my sell by date?

Working at DESY has given me the opportunity to get to know many people whose friendship I value, and whose help and support has been indispensable. I would like to thank Lee West and Paul Sutton for helping me to get to grips with the Forward Muon System. Chris Hilton deserves a special thank you for all the help with the ψ' analysis. The fact that I have a thesis at all owes a great deal to Chris's ability to explain things clearly, patience whilst answering lots of silly questions, and above all, the immense amount of practical advice given. Tim Nicholls, Eram Rizvi and Paul Newman have also been very helpful and generous with their knowledge of computers and physics. For proof reading all or part of my thesis, I would like to thank Lee West, Chris Hilton, Paul Newman and Ian Kenyon.

This section would not be complete without a big thank you to the women at DESY, without whom, I would have doubtless gone insane. So, thank you Molly, Chandy, Jane, Kirstee and Rachel. Thanks must go to Eram and Andrew for being jolly decent flatmates, and letting me live with them after I got kicked out of my lovely little house. Indeed, thanks to everyone who made the time I spent in Hamburg so enjoyable. Writing up this thesis has not been the easiest task I have faced, but I'm grateful to the people around me in Birmingham who have helped to make that task easier. I would particularly like to thank Paul for his patience and support.

Last, but most certainly not least, I would like to thank my Mum and Dad, who have supported me tirelessly over the years. They have given guidance when I'm confused, comfort when I'm down, and the odd pound or two when I'm broke, but most of all, they've had faith in me. Thank you.